EFFECT OF ATMOSPHERIC ICE ACCRETION ON THE DYNAMIC PERFORMANCE OF WIND TURBINE BLADES

Abdel Salam Alsabagh

A Thesis Submitted in Partial Fulfilment

of the Requirements of the University of Hertfordshire

for the Degree of Doctor of Philosophy

The programme of research was carried out in the School of Engineering & Technology, University of Hertfordshire, Hatfield, UK

May 2016

Abstract

Atmospheric icing presents serious challenges to the development of wind power of the wind energy industry in cold regions. The potential detrimental impact on the safe operation of wind turbines and the energy harvest hasn't been fully understood and requires further investigation. This thesis presents the research on icing profiles under different weather conditions and their impact on natural frequency, fatigue life, and lift and drag of the wind turbine blade. The research aims to develop a further understanding of the effect of atmospheric ice accretion on the structural integrity and aerodynamic performance of wind turbine blades through numerical and aerodynamic investigations to address the challenges facing the industry.

A 5-MW NREL (National Renewable Energy Laboratory) wind turbine blade was selected for this study, due to availability of required geometric design parameters and experimental data for verification. The turbine rotor and its three blades were modelled and numerically simulated with commercial finite element software ANSYS. Three icing scenarios were chosen according to the ISO Standard and the corresponding icing profiles were developed to investigate their influence on vibrational behaviours of the wind turbine blade and rotor under different weather conditions. Icing loads were applied on the leading edge of the blade and natural frequency results were compared between clean and iced blades. It was found that harsh icing weather drove the natural frequency down to the near resonance limit, which could lead to significant issue on structural integrity of the wind turbine.

The effect of atmospheric ice accretion with additional load due to varying wind speeds on the fatigue life of the wind turbine blade has been investigated. Significant reduction of fatigue life was found due to the increase of the von Mises stresses.

Finally, computational fluid dynamics (CFD) analysis was carried out to investigate the effect of atmospheric ice accretion on the aerodynamic performance of typical 1-MW and 5-MW wind turbine blades. Results of the drag and lift coefficients and power production under different icing scenarios were obtained for five angles of attack. Compared with the results of the clean aerofoil profile, remarkable reduction in the power generation was observed due to the accreted ice at various aerofoil sections in the spanwise direction of the blade, demonstrating the detrimental impact of atmospheric icing on energy harvest for the wind energy industry.

Dedication

Say: "Truly, my prayer and my service of sacrifice, my life and my death, are (all) for Allah, the Cherisher of the Worlds.

No partner hath He: this am I commanded, and I am the first of those who bow to His will.

The Holy Quran

Chapter 6: Al-An`am (162-163)

Acknowledgement

My first and most earnest acknowledgment must go to my principal supervisor at the University of Herefordshire Dr Yigeng Xu for his devotion to this research. He has been the most instrumental person for my academic and research achievements, and to my principal supervisor at Narvik University College, Prof. Muhammad Shakeel Virk, who provided the motivation, encouragement, guidance and advice which have prepared me for the challenges of future life.

I also would like to express my sincere gratitude to my previous supervisor Dr William Tiu who taught me how to dig in ANSYS, and to Dr Ying Pei to his support on my CFD work. My deepest thanks to Narvik University College for sponsoring my study at the University of Herefordshire and allowing me to access all the research facilities they have. Many thanks also to Al-Balqa` Applied University for their financial support and to my external supervisor Prof. Omar Badran for his continuous helping and guidance.

I also convicted cordial appreciation and gratitude to my family in Jordan for their patience and endurance troubles during the period of my study.

Table of Contents

List of Figures

List of Tables

Nomenclature

Symbols

A	Cross Sectional area
a	The axial induction factor
a'	The tangential induction factor
â , Ъ	Constants
c	Chord length
C_L	Lift coefficient
D	The total rime accreted diameter
C_D	Drag coefficient
D_f	The drag force
d̲	The dimension perpendicular to the aerofoil chord
ΔE_{mech}	The change in mechanical energy
ΔV	The change in potential energy
F_i	The i^{th} conservative force
F_D	Drag force component
F_L	Lift force component
I	The ice accretion intensity
k-ϵ	Reynolds-Averaged Turbulence
[k]	Generalized stiffness matrix
Ł	Thickness of accreted ice
L	Length of blade

L_f	Lift force
L_{fa}	Lift force for certain area
L_w	The turbulence intensity
[m]	Generalized mass matrix
$\hat{\mathrm{m}}$	Preliminary value for accreted ice mass
m	The mass
N	Number of cycles to failure
n	Number of degrees of freedom and spanwise stations
P	Airflow pressure
$\mathbb{P}$	Output power of an aerofoil
R_e	Reynolds number
$\bar{r}$	Blade local radius
$\mathfrak{r}$	The ratio of the excitation frequency to the natural frequency
S-N	Stress-Number of cycles to failure
s_p	The span for each segment of the blade
T	The kinetic energy
ΔT	The averaged kinetic energy
$\underline{\mathrm{T}}$	Thrust of incoming airflow
t	The thickness of ice
u	Local wind velocity
$\hat{\mathrm{U}}_o$	Incoming wind velocity
x	Displacement in lateral direction
V	The potential energy

ΔV	The change of potential energy
$\tilde{\mathrm{V}}$	The volume
$[W]$	Matrix of weighting
$\dot{\mathrm{W}}$	Relative wind velocity
$\bar{\mathrm{W}}$	Watt
$\hat{\mathrm{W}}$	Width of blade Section
₩	Work done of incoming air
x_i	The ith generalized coordinate
$\dot{x}_i$	The generalized velocity
$\vec{x}$	The column vector of the generalized coordinates
X/X_{st}	Dynamic magnification factor

Abbreviations

DOF	Degrees Of Freedom
AOA	Angle of Attack
APDL	ANSYS Parametric Design Language
NREL	National Renewable Energy Laboratory
CAD	Computer Aided Design
CCD	Charge-Coupled Device
CFD	Computational Fluid Dynamics
CFMBD	Computational Flexible Multi-Body Dynamics
CMS	Condition Monitoring System
CSV	Comma Separated Values
FVM	Free-Vortex Method

FRP	Fibre-Reinforced Plastics
GL	Germanischer-Lloyd
GUI	Graphical User Interface
IGES	Initial Graphics Exchange Specification
FDS	Fault Detection System
WTG's	Wind Turbine Generators
ISO	International Organization for Standardization
TMD	Tuned Mass Damper
LWC	Liquid Water Content
MVD	Median Volume Diameter
OWEP	Offshore Wind Energy Plants
IEA	International Energy Agency
MST	Modified Strip Theory
STMDs	Semi-Active Tuned Mass Dampers
UREX	Universal Resonant Excitation

Greek

$\propto$	Angle of attack
$\bar{\alpha}$	Ice accretion correction factor
γ	Damping factor
φ	Flow angle
θ	The pitch angle
δ_u	The standard mean deviation of velocity
λ_r	local speed ratio
Ω	Angular speed

ϖ	Mass concentration of ice particles
σ_{vm}	Von Mises stress
Ĉ	Water liquid content
μ	The dynamic viscosity
þ	Ice precipitation rate
λ	Smallest exact eigenvalues
ρ	Density
ν	The kinematic viscosity
μ	The dynamic viscosity of air
ω	Natural frequency
Φ	Mode shape

CHAPTER ONE

INTRODUCTION

1.1 Background

Wind turbines for the production of energy from the wind are being used more extensively nowadays in cold regions due to the abundance of wind resources and the ever-increasing demand of renewable energy of the world. Nevertheless, cold climate poses some unique challenges to the wind power industry as atmospheric icing on wind turbine blades may induce excessive structural dynamic vibration and energy loss in production. According to (Dalili et al., 2009), a 7-weeks of wind turbines stoppage was reported in the winter of 2002-2003 in Sweden. An investigation on the impact of climate change on the wind energy generation potential within the Northwest USA was carried out in 2008 showing that the energy reduction may reach as high as 40%. (Sailor et al., 2008). It has been shown that ice accretion on the blades can lead to up to 30% decrease in the lift and 50% increase of the drag. During the winter of 2009/2010, in Sweden, five 1.2-MW wind turbines have experienced losses in the power ranged from 20%-56% with total stoppage from 59 to 90 days (Carlsson, 2011).

While some efforts have been made to address above challenges to the wind energy industry, the likely harmful impact of atmospheric ice accretion on the safe operation of wind turbines and the energy harvest hasn’t been fully understood and requires further investigation. It is therefore clear that a detailed research on the effect of atmospheric ice accretion on the dynamic performance of wind turbine blade is vital to the wind energy industry to ensure the optimum operation without compromising the safety of the wind turbine.

1.2 Aim and Objectives

To address the challenges facing the wind energy industry operating in cold regions, this project carries out an in-depth research on icing profiles under different weather conditions and their impact on natural frequency, fatigue life, and lift and drag of the wind turbine blade. The research aims to develop a further understanding of the effect of atmospheric ice accretion on the structural integrity and aerodynamic performance of wind turbine blades through numerical investigation.

Three atmospheric icing scenarios based on the International Standard ISO (12494) are chosen to represent most of the icing events happening in the cold regions which vary from moderate to heavy icing including severe cases. The cases are based on longer events of icing which usually took place in cold countries.

The objectives of this project are as follows:

- Develop an approach on the basis of ISO (12494) Standard to estimate the on-blade accreted ice mass and thickness and apply the technique to estimate the accreted ice mass on a 5-MW wind turbine blade under three icing scenarios.
- Construct models of typical wind turbine blades and an assembled NREL 5-MW wind turbine rotor and carry out detailed numerical investigation of the effect of atmospheric icing on the vibrational behaviour of the wind turbine blade and the turbine rotor.

- Study the effect of heavy icing scenario along with aerodynamic pressure on the fatigue life of a 5-MW wind turbine blade.
- Investigate the loss of wind energy generation of a typical 5-MW and 1-MW aerofoils due to icing through CFD simulation.

To achieve above project aim and objectives, a comprehensive literature review will be carried out to understand theories and techniques associated with the dynamic effects of atmospheric icing on wind turbine blades. A Computer Aided Design (CAD) model of a typical 5-MW wind turbine blade based off-shore will be constructed using coordinates from the manufacturer. The NERL 5-MW rotor will be constructed by assembling three blades with the hub. Accreted ice will be modelled as an additional mass on top of the blade using the technique developed on the basis of ISO Standard 12494. Finite element software ANSYS will be used to determine the effect of atmospheric icing on the natural frequency of the turbine blade and its assembly. The impact of lowered natural frequencies due to icing on structural integrity will be investigated for two different wind speeds. CFD software STAR-CCM+ will be used to investigate the effect of atmospheric icing on the lift and drag and the subsequent power loss of the turbine blade.

1.3 Outline of the Thesis

This thesis presents the research work carried out between May 2011 and December 2014 for the PhD project titled “Effect of atmospheric ice accretion on the dynamic performance of wind turbine blades”. It consists of eight Chapters. Chapter 1 gives a brief introduction of the background associated with the project and defines the project aim and objectives. Chapter 2 is a comprehensive review

of the concept, theories, techniques, and key findings in the field related to the project. Chapter 3 explains the research methodology employed in the project. Chapter 4 presents the numerical set up of the FE model of the wind turbine blade and its assembly, and a method to estimate icing mass and profile under different weather conditions. Icing mass and profiles for the 5-MW wind turbine blade and its rotor are determined in Chapter 5. The effects of atmospheric icing on the vibrational behaviour of the turbine blade and the rotor are investigated with the finite element approach. The impact of the atmospheric icing along with aerodynamic pressure on the structural integrity of the wind turbine is investigated in Chapter 6. Detailed study of the effect of atmospheric icing on the aerodynamic performance including the lift/drag and power generation of the wind turbine blade is presented in Chapter 7, and finally Chapter 8 summarises the key results achieved in the project and the areas where further work is required.

CHAPTER TWO

LITERATURE REVIEW

2.1 Wind Turbines and Wind Energy

A wind turbine is a device that converts kinetic energy from the wind into electrical power. Wind energy has been used for thousands of years. One of the earliest application was using sails to drive boats by old Egyptians in the Nile River about 5000 B.C. (Ahlström, 2005). Windmills have been used for at least 3000 years, mainly for grinding grain or pumping water (Burton et al., 2011). But wind turbines are relatively modern invention. The 1250 kW Smith–Putnam wind turbine constructed in the USA in 1941, as shown in Figure 2.1, was a remarkable leap in the wind power industry and had kept its leading position for 40 years (Turkia et al., 2010).

Development in nuclear power and availability of oil in cheap price led to a decline of development in large wind turbines. But with the huge increase in oil price since 1973, the interest in wind energy increased again. Recently, wind energy industry has played a key role in the supply of renewable energy with an increase in installed wind turbine capacity to over 40 GW in the year 2010 (Burton et al., 2011). With the increasing demand of energy and awareness of environmental issues, people all over the world are looking for clean and renewable source of energy. Wind energy could be the key word for the future generations.

Figure 2.1: The 1250 kW Smith–Putnam wind turbine (Turkia et al., 2010)

2.2 Structures of Wind Turbine Blades

Wind turbine design is the process of defining the form and specifications of a wind turbine to extract energy from the wind. The understanding of the structure of the blade is important because the blade is the key component of the wind turbine which converts the wind energy into rotary mechanical movement. A preliminary study to optimize the use of material in a 2.5 m long fiberglass composite wind turbine blade was presented in (Bechly and Clausen, 1997).

From structural point of view, the rotor of a wind turbine consists of a number of subsystems corresponding to all the rotating parts of the wind turbine outside the nacelle. These subsystems include the rotor blades, the hub, and the blade pitch and yaw mechanisms.

The rotor blade technology is associated more with light weight aeronautical engineering than with conventional mechanical engineering. Wind turbines are subjected to continuous loading and unloading. The rotation of the rotor, shafts and gears, the gusting and lulls of the wind, and the subsequent vibrations induced by all these factors, lead to load cycles varying in size, frequency, and sequence. The bending moment due to the gravity load already results in up to 10^7 - 10^8 load cycles alternation within the lifetime of a wind turbine (Hau, 2010a). This represents about 20 working years depending, of course, on the overall operating conditions, namely the weather conditions.

Computer aided engineering methods were developed to aid in the preliminary design of composite wind turbine blades. These methods allow for the realization of any required design specifications of the chord, twist, and aerofoil geometry along the blade and any number of shear webs (Bir and Migliore, 2004). The main structural features of a typical wind turbine blade are illustrated in Figure 2.2.

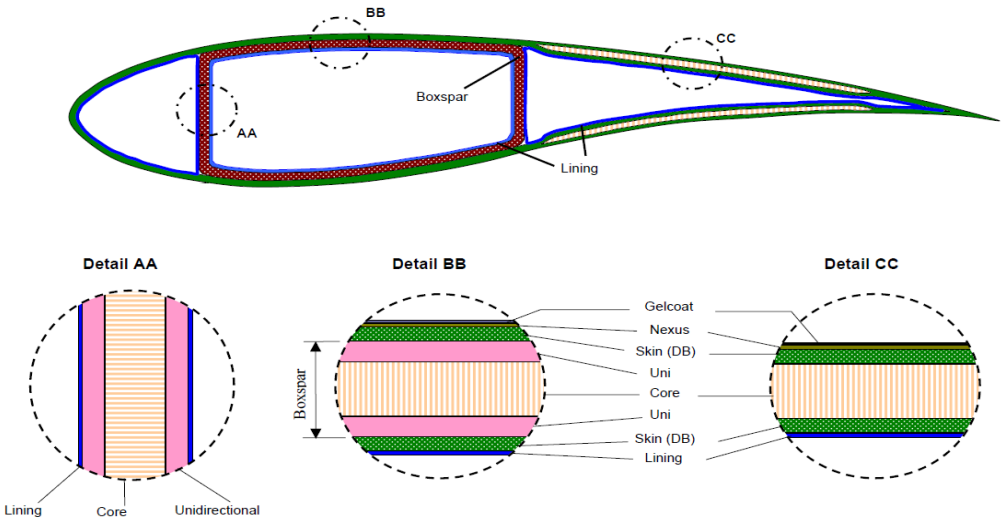

Figure 2.2: Structural layup at a typical blade section (Bir and Migliore, 2004)

A wind turbine blade normally consists of two shells, bonded together with structural adhesive as shown in Figure 2.3-a. There are two main designs of wind turbine blade: blade of one-piece construction cross-section, and blade of two-piece construction cross-section where the adhesive is applied. Figure 2.3-b shows the one-piece blade construction in which a spar is fixed to the first shell, and the second shell is then lifted over onto the installed spar, and so making the (shell - spar - shell) construction. Adhesive systems such as Polyurethane (PU) are usually sufficient to support the applied stresses. In a typical type of blade shown in Figure 2.3(c), two shear webs (stiffeners) are bonded to the shells (Albisser, 2009).

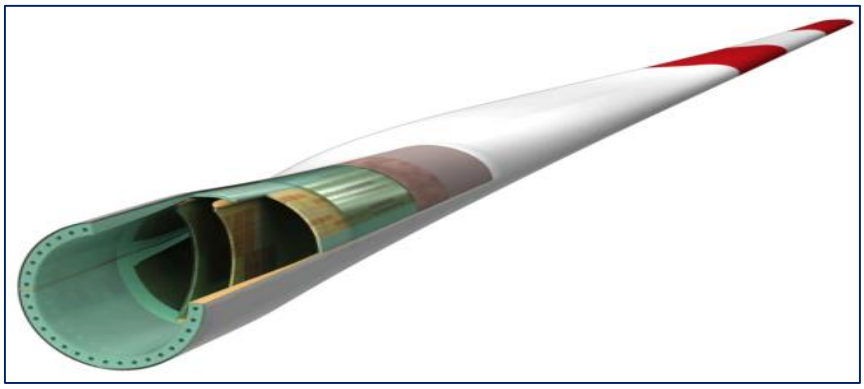

(a)

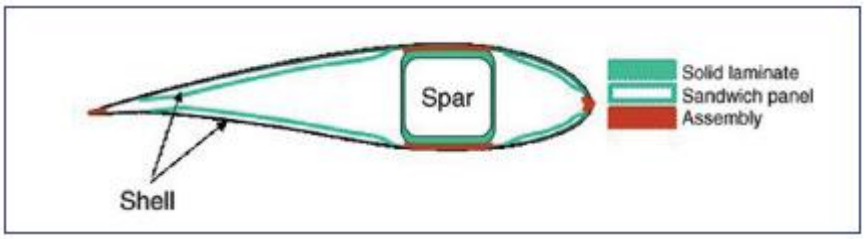

(b)

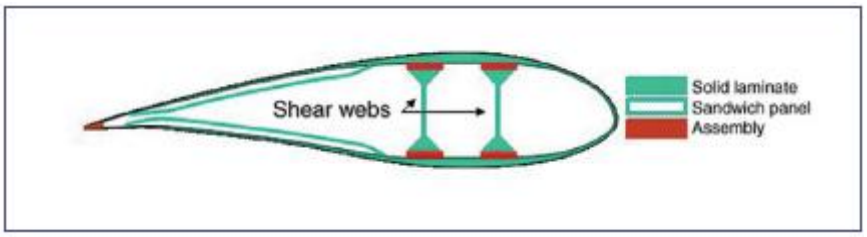

(c)

Figure 2.3: Wind turbine blade sections, (a) simplified diagram, (b) Blade of one-piece construction: cross-section, and (c) Blade of two-piece construction (Albisser, 2009)

Two different geometries are included in the blade internal structure which basically require two dissimilar adhesive chemistries. It is essential to use two resin and hardener, which from thixotropic materials, is essential in the process of bonding the blade components (Albisser, 2009).

The use of thixotropic agent is important to achieve a non-slump texture, otherwise, high shear conditions will be dominant for both resin and the hardener

during the process of mixing and application steps in which stress can lower the viscosity. (Albisser, 2009).

As for composite technologies for large wind turbine blades, which basically comprise of skins and spar cap made of laminated glass-epoxy type E which is designated as CDB340 based on tri-axial material has a composition of 25% of both distribution of +45° and -45° and 50% for 0° fibers. During the stacking sequence, the spar cap is laminated with 70% uniaxial and 30% off-axis fibers on weight basis (Griffin, 2004).

Two years later, Griffin (Griffin, 2004) published his second report about composite technologies for large wind turbine blades. The report provided a discussion of materials and various manufacturing concerns for large wind turbine blades for 3-MW and 5-MW classes. Detailed specifications were given for a 3-MW turbine blades including parametric analysis and the benefits of using hybrid carbon-glass materials. Figure 2.4 shows the relation between the blade mass and rotor radius of various commercial blade manufacturers

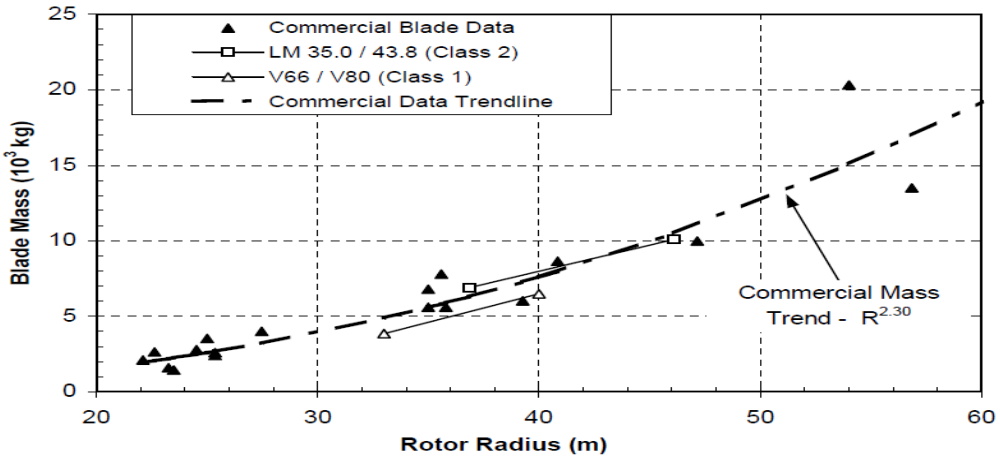

Figure 2.4: Mass growth for the commercial MW-scale blade designs - primarily fiberglass - (Griffin, 2004)

Finite element modelling was extensively used to study both static and dynamic limitations of wind turbine blades (Bonnet, 2007). In all cases, wind turbine blades have their own strength requirements including fatigue strength for 20-25 years lifetime with number of cycles in the order of 10^7, enough clearance between the wind turbine blade tip and the turbine tower, the blade root and hub should also endure the static load due to the blade weight also the nacelle structure, tower and foundation need to sustain the whole machine dynamics (Bonnet, 2007).

The stiffness and strength of the blade under each loading mode for any given materials is determined by the exact shape of the internal structure. For a wind turbine blade reliable design, the material of the blade should be as light as possible for a given stiffness so as to meet the blade design criteria, this is can be maintained by having constant blade-tip speed ratio for maximum power coefficient for all wind speed and also to minimise the blade weight induced fatigue loads.

2.3 Wind Energy Resources in Cold Climate

As the energy concerns recently become more crucial and the world is struggling to find cleaner sources of energy, the industry of wind energy is more likely to expand significantly every year. Most of such investment happens to be in cold climate regions like northern Europe and the arctic areas as shown in Figure 2.5. The cold climate affects the dynamical behaviour of wind turbines in various ways and poses serious challenges to the wind energy industry.

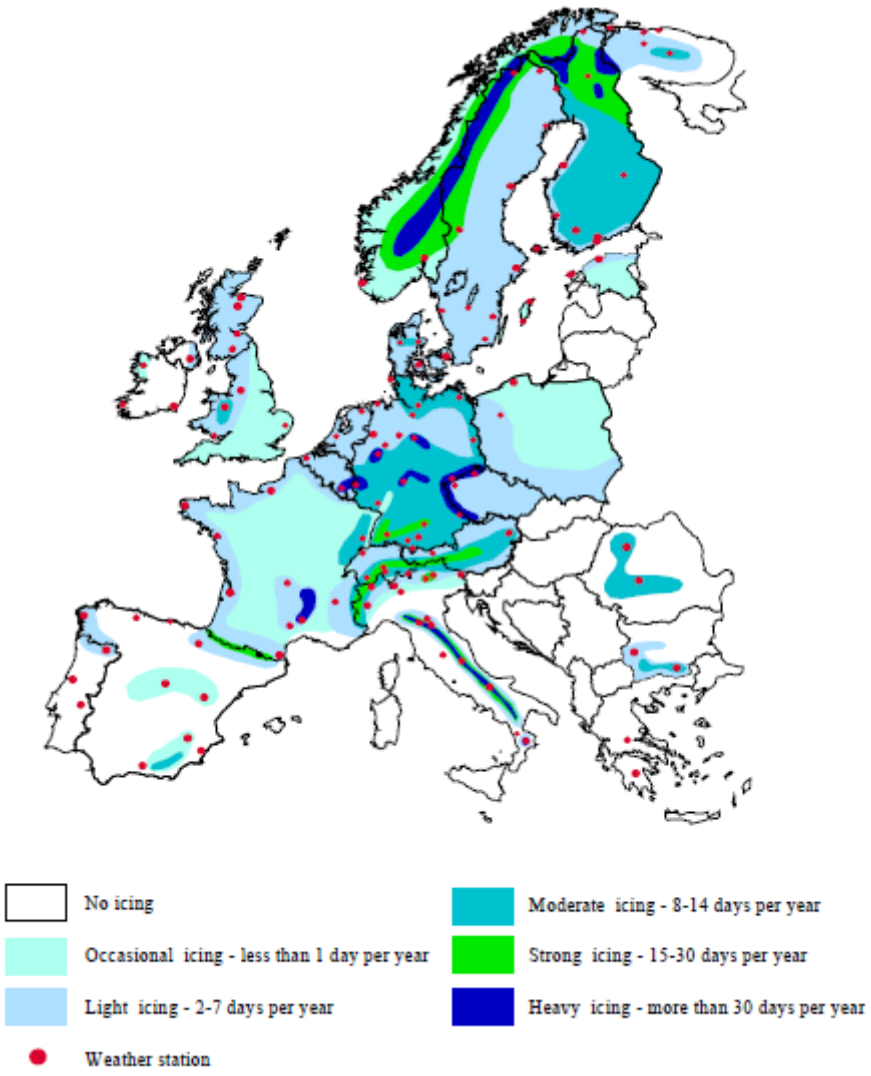

Figure 2.5: Icing map of Europe (Tammelin et al., 2000)

Ice accretion is not uniformly exist along the blade length. Ice thickness increases rapidly at the tip while less ice thickness can be observed near the root section of the wind turbine blade. The wind turbine blades angular movement and tapered shape of blades structure are the main two factors identified behind this observation, namely (Fu and Farzaneh, 2010). Furthermore, the leading edges of the blades collect more ice around the stagnation points where the local velocity of the incoming air is zero (Bose, 1992), (Tammelin et al., 1998),

and (Seifert and Tammelin, 1996) . An estimated possible ice load on a 38m radius blade of 2 MW wind turbine may reach 25-30 kg/m (Frohboese and Anders, 2007b). The weight of accreted ice under some severe weather conditions can be as high as 50% of the blade structural weight ((ISO, 2001a), (Walsh, 2010), which demonstrates the seriousness of a potential risk on the structural integrity of the wind turbine.

2.3.1 Energy Losses Due To Atmospheric Icing

The structural behaviour of the wind turbines considerably affected by harsh weather especially in cold regions, other potential problems like load imbalance, changing of natural frequencies, turbine vibrations and increasing of fatigue loads are often happened due to excessive ice accretion and irregular shedding, moreover, ice accretion on the blades is usually associated with increasing of drag and decreasing of lift (Wang et al., 2007). Due to severe weather conditions, the annual power loss may be ranges from 20% to 50 % (Seifert and Tammelin, 1996). A performance losses of about 20 % was reported for a 450-kW wind turbine due to the effects of rime ice accretion (Parent and Ilinca, 2011).

(Seifert and Richert, 1997a) led a study of measurements estimation of unsteady behaviour and dynamic stall effects for iced and clean 300-kW wind turbine rotors by using a wind tunnel. The study also included a calculation of the power loss and power curves for the rotor of a stall and pitch controlled. The load due to ice accretion increases with the time of icing event. It also increases with the increase of ice density which could reach 900 kg/m^3 (Frohboese and Anders, 2007a). (Haaland, 2011) conducted a study for Aapua wind park, Sweden, and showed

that the total production during the winter 2009-2010 gives a loss of 16000 MW, or 25%, for the wind farm as a whole due to icing. The highest loss is found in January, which alone stands for a loss of 7000 MW, or 52% of the expected production during this month. (Lacroix and Manwell, 2000) pointed out another important loss which is the power wasted for heating the blades to overcome the icing problem. According to early study in Europe, (Jasinski et al., 1997) stated that thermal anti-icing system requires an amount of heater power equal to at least 25% of the wind turbine maximum rated power. (HoloOptics, 2012) had investigated in a study for a 2.5-MW wind turbine located in Skellefteå, Sweden, and for a period of 1500 hours during which severe icing was present in 246 hours, the production loss has a value of more than €22000 / year.

2.3.2 Hazardous Issues of Ice Shedding

Safety issues for both working and stand still wind turbines aroused as crucial question in the industry of wind power generation, this resulted in the development of risk assessment methodologies. It has confirmed that a distance of 250 m from the turbine is necessary to minimise the risk of being struck by ice thrown in a moderate icing scenario climate (Morgan et al., 1998), while ice will fall within 50 meters of the wind turbine when the blades are stationary(Gadawski and Lynch, 2011, Walsh, 2010) . The ice shedding may causes potential injuries (Colby, 2008). (Antikainen P. et al., 2003) reported that the accumulated ice may be a real danger for the corresponding rotation inertia, which may increase because of additional weight of ice.

The accreted ice also possesses a possible danger of being thrown away while melting and/or due to centrifugal forces as blades are rotating. Safety measures include spacing turbines apart, placing them in uninhabited locations, and avoiding too close to roads or agricultural infrastructure (Perovic et al., 2010), (Seifert et al., 2003). Ice shedding form wind turbine blades is illustrated in Figure 2.6. Wind turbines are normally built far away from housing complexes, industrial plants, etc., as the wind conditions are not encouraging in the neighbourhood of large obstacles. Furthermore, certain distances are required by national regulations must be considered regarding the acoustic noise emission and shadow flicker this is when wind farms are planned in the regions of housing areas, 700 meters is an accepted distance for separation (Barclay, 2012).

Figure 2.6: Accumulated ice shedding from black blades (Maissan, 2001)

2.3.3 Ice Distribution over Wind Turbine Blades

Even though icing of both static and moving structures is a common phenomenon in the high Alps and Polar Regions, predicting accurately the intensity, thickness and mass of icing events is difficult (Makkonen, 1988). Standardized methods to calculate and predict the local icing time based on typical meteorological measurements data are still lacking (Laakso, 2010).

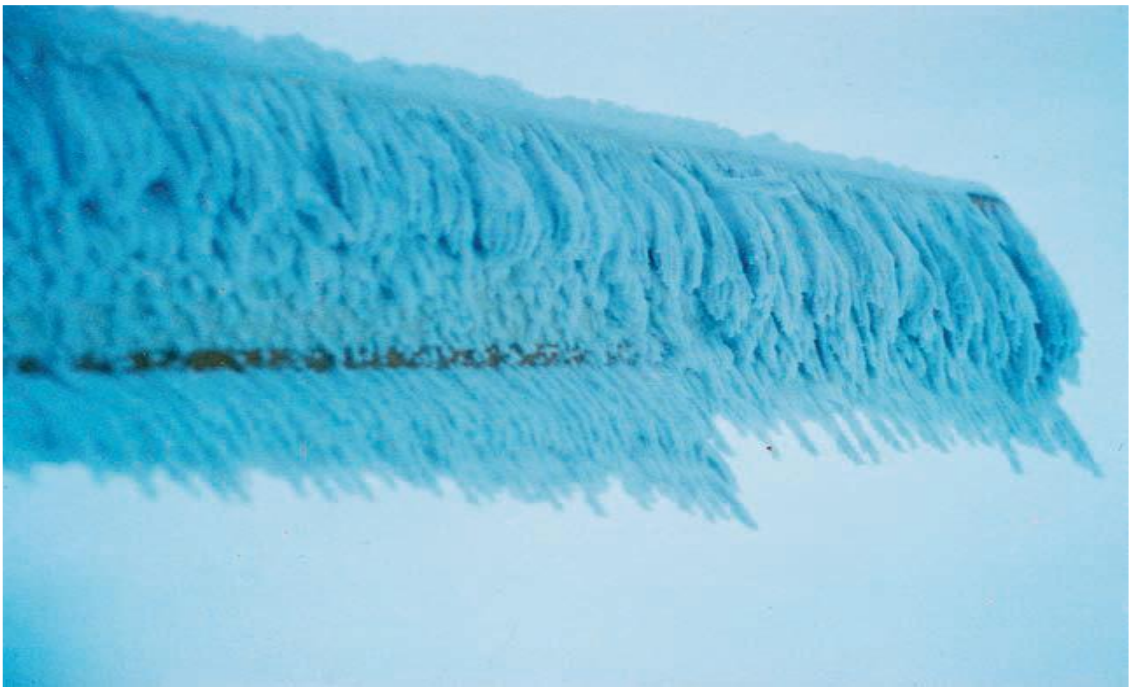

Figure 2.7: Blade after four days of moderate to heavy icing (Walsh, 2010).

It is noticed from Figure 2.7 that large amount of ice exists on the tip and leading edge of wind turbine blade under heavy icing event. A numerical analysis of atmospheric ice accretion on 5-MW wind turbine blade at five different sections for the rime and the glaze icing conditions had been carried out based on a computational fluid dynamics technique (Virk et al., 2012).

Figure 2.8 shows the effects of atmospheric temperatures variation on the maximum accreted ice thickness and mass along a 5-MW wind turbine blade for about an hour.

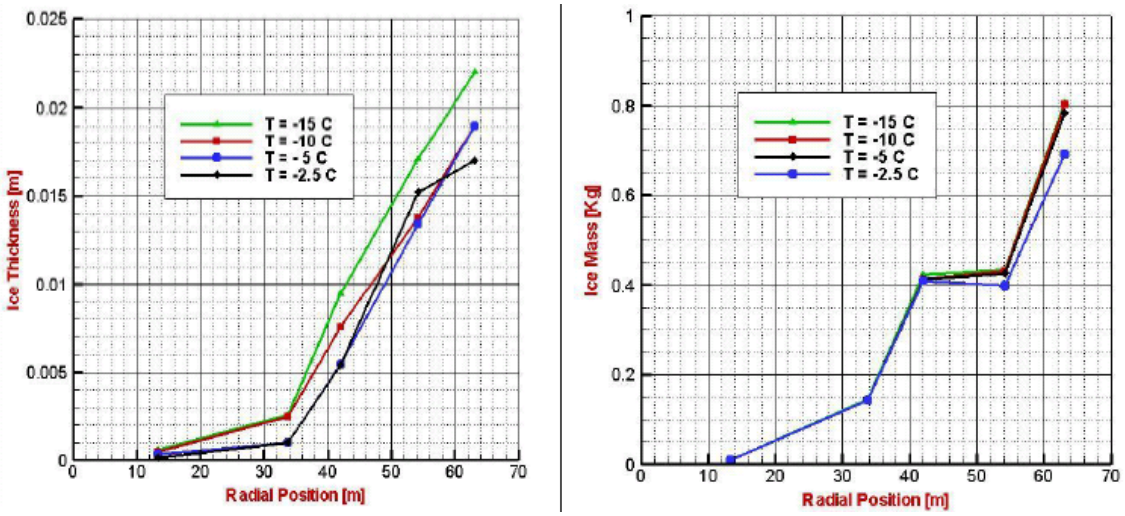

Figure 2.8: Effect of atmospheric temperature variation on accreted ice mass to the right and on thickness along blade to the left (Virk et al., 2012)

Commonly ice is either soft or hard rime, soft rime is gradually turned into hard rime during continued icing. Ice accretion depends on the temperature, wind speed, the density of the deposition, the liquid water content of the air, the surface of the accreting ice structure, and dimensions of the object (Dobesch, 2005). Ice density at approximately 350 kg/m^3 is considered as soft rime, and is fairly easy to brush off. Though, underneath the soft rime layer at the blade-ice interface there is a harder layer difficult to even scratch off, this harder rime layer is of a density reaches 550 kg/m^3 (Walsh, 2010).

In severe winters, ice loads can be as high as 400 kg/m on some latticed tower structures on the Finnish high fells such as Ylläs (Sundina and Makkonen, 1998). While accreted ice on wind turbine blades and nacelle are relatively less.

The weight of accreted ice in some severe weather situations can be as high as 50% of blade weight (ISO, 2001a), which indicates the seriousness of a possible failure risk of the wind turbine structure due to the accreted ice. When the wind carries super-cooled water droplets towards the wind turbine tower, they will be expected to hit and then freeze on the tower, if the tower is thick; usually a higher percentage of the water droplets will follow the wind flow around it and won't stick. In some heavy icing conditions, a tower with a mass of around 1000 kg may collect ice five times of its own mass (Laakso et al., 2010).

(Kollár and Farzaneh, 2010) experimentally studied the importance of varying the axis of a cylindrical icing object and the angle of the incoming wind. By using a horizontal icing wind tunnel, the shape, mass, and profile of ice accretion obtained. (Fu et al., 2006) studied the size effect of the exposed objects on ice accretion, the study showed that a larger object is less likely to be subjected to higher intensity icing, the author also concluded that the icing rate of can increase remarkably with the increase of air speeds.

2.3.4 Ice Shape and Mass Estimation

Atmospheric icing is the physical process where drifting or falling water droplets, rain or wet snow freezes upon a surface exposed to the open atmosphere, as was defined by 'The International Organization for Standardization' (ISO, 2001b). It should be noted that the process of atmospheric icing is quite complicated and depends on many variables including wind speed, air temperature, median volume diameter (MVD), and liquid water content (LWC) of the water droplets. Meteorological parameters are not the only functions for ice accretion, the

properties of the actual object exposed to icing are also of great importance, and these properties include shape, size, orientation relative to the mean wind relative velocity direction and flexibility. Icing most often occurs on objects exposed to the prevailing wind at times with freezing temperatures and significant LWC. However, low temperatures alone do not automatically imply ice accretion. Water vapour or some form of condensation has to be present in the atmosphere to trig the icing (Laakso et al., 2010).

Ice accretion can also be defined as the process of ice building up on the surface of an exposed structure. According to (Vargas, 2010), different types of icing on structures can occur, main types of icing are:

- In-cloud icing which are super-cooled water droplets hitting surfaces exposed to incoming cold air.
- Glaze ice, rime (soft and hard) ice and mixed ice. The formation of glaze is happened when the thermal energy released by the formation of ice from the droplets impacting the surface is slowly removed; as a result, some portion of the incoming droplets remains as liquid water. Consequently, some liquid water is always present, and therefore the surface temperature will be 0°C (Homola, 2005). The quick removal of the thermal energy by wind and radiation droplets that are impacting the surface is the key of the process of rime formation so there is no liquid water presents on the exposed surface. Rime ice appears in white and usually breaks much easier than glaze.

  Process of precipitation icing occurs when precipitation, either snow or rain, freezes just after striking the surface.

The rate of accretion of ice and snow on a cylindrical object is given by the formula (Makkonen, 1994)

$$\frac{dM}{dt} = \bar{\alpha}_1 \times \bar{\alpha}_2 \times \bar{\alpha}_3 \times \varpi \times \tilde{v} \times A \quad (2.1)$$

where M is the ice mass per unit length at time t . The terms $\bar{\alpha}$ are correction factors that vary from 0 to 1, the ratio of the particles striking surface to the maximum possible particles striking the surface is the collision efficiency $\bar{\alpha}_1$. This factor is mostly less than 1 since small particles will try to follow the incoming air stream and so failed from striking the surface. $\bar{\alpha}_2$ is known as the sticking efficiency which represents the ratio of the flux density of particles sticking to the surface to the flux density of the maximum possible particles striking the surface. $\bar{\alpha}_3$ stands for the accretion efficiency, which represents the ratio of the rate of ice building up on the exposed surface to the flux density of maximum possible particles sticking to the surface. Usually this factor is less than 1, which means that some portion of the particles are melting and running off after sticking to the exposed surface. ϖ is the mass concentration of ice particles. $\tilde{v}$ is the relative velocity of particles and A is the cross sectional area of the object exposed to icing with respect to the direction of particle velocity.

The maximum growth rate of ice will occur when the three correction factors equal unity. However, due to certain atmospheric processes, these correction factors often attain values less than unity, therefore reducing the growth rate from its maximum value (ISO, 2001a, Rindeskär, 2010). Due to the importance of these

factors in the process of ice accumulation, more details are given in following sub-sections.

2.3.4.1 Collision Efficiency

The inertia and the aerodynamic drag of the water droplet will determine the trajectory path in order to determine the collision efficiency. If the inertia of the water droplet is greater than the aerodynamic drag then the droplet will impact on the object's surface, and if the aerodynamic drag is greater the droplet will tend to follow the airstream around the object. The bigger the droplet is the greater chance for if to collide on the exposed object due to higher inertia force for it while smaller droplets have greater chance for it to follow the airstream away from the object due to higher aerodynamic drag as shown in Figure 2.9.

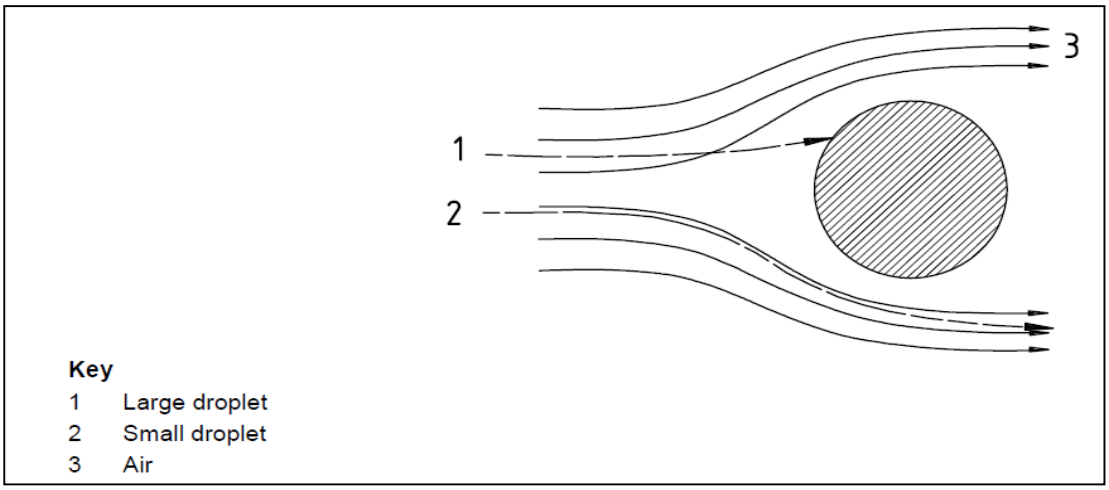

Figure 2.9: Air streamlines droplet trajectories around a cylindrical object (Makkonen, 2000)

The collision efficiency $\bar{\alpha}_1$ can be determined if the above variables (droplet size, air stream velocity and object dimensions) are known.

2.3.4.2 Sticking Efficiency

The sticking efficiency is the ratio of the numbers of droplets that stick to the surface of an object to the total number of droplets that strike the surface without bouncing off it. This efficiency is dependent upon temperature, impact velocity of droplets and liquid water content LWC (Dobesch, 2005). An impinging super-cooled water droplet freezes without bouncing off the surface. This is true both for dry and wet growth. Figure 2.10 shows water droplet hitting an iced surface while wet growth droplet hitting an iced surface with a liquid layer is illustrated in Figure 2.11.

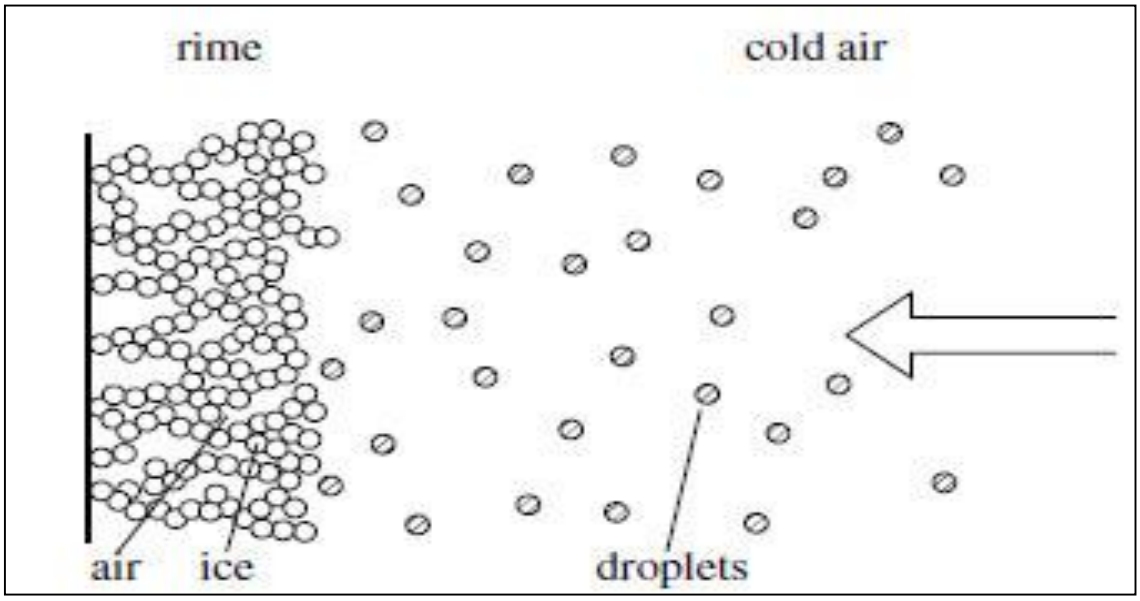

Figure 2.10: Growth of rime ice (dry growth)

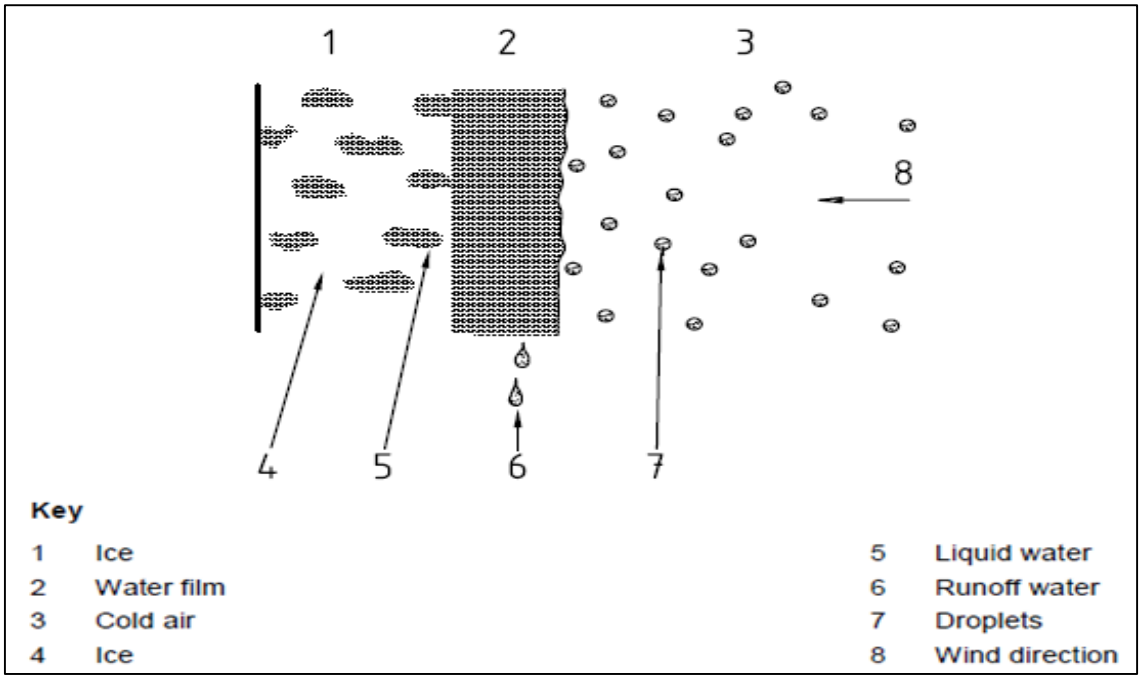

Figure 2.11: Growth of glaze ice (wet growth), (ISO, 2001a)

As mentioned in Section 2.3.4, for maximum ice growth, the sticking efficiency for water droplets is therefore considered to equal unity. On the contrary, snow particles bounces very efficiently. However, the rate of bouncing depends on the fraction of liquid water within the snowflake. If there is a liquid layer on the surface of the wind turbine blade, the sticking efficiency is close to 1, while in contrast, for a completely solid snowflake $\bar{\alpha}_2 \approx 0$.

2.3.4.3 Accretion Efficiency

If the ice accretion is dry, as in Figure 2.10, all the imposing water droplets freeze upon impact and so the accretion efficiency $\bar{\alpha}_3 = 1$. And if the accretion is wet, as in Figure 2.11, the accretion efficiency depends on the rate at which latent heat is moved away from the surface of the object through the liquid water in the air.

The water droplets do not freeze when colliding with the surface drop off the object as a result of gravity or wind drag.

Empirical models for precipitation icing are studied in details (Makkonen, 1994). Equation (2.2) may be also used (Goodwin et al., 1983) with another modification considered by (Dobesch and Nikolov, 2005) in equation (2.3)

$$\frac{dM}{dt} = 2 \times \mathrm{r} \times \hat{\mathrm{C}} \times u \quad (2.2)$$

$$I = 0.26 \times \mathrm{þ}^{0.88} \times u \quad (2.3)$$

where $\mathrm{þ}$ is the precipitation rate and r is the radius of the cylinder at which icing takes place. I is the ice accretion intensity in g.cm^{-2} h^{-1} and u is the wind speed m.s^{-1}. In equation (2.2), $\hat{\mathrm{C}}$ is the LWC of the air. The effects of temperature and wind of speed are clear in Figure 2.12 (ISO, 2001b), where the curves are shifted to the left with the increasing of liquid water content and with the decreasing of object size.

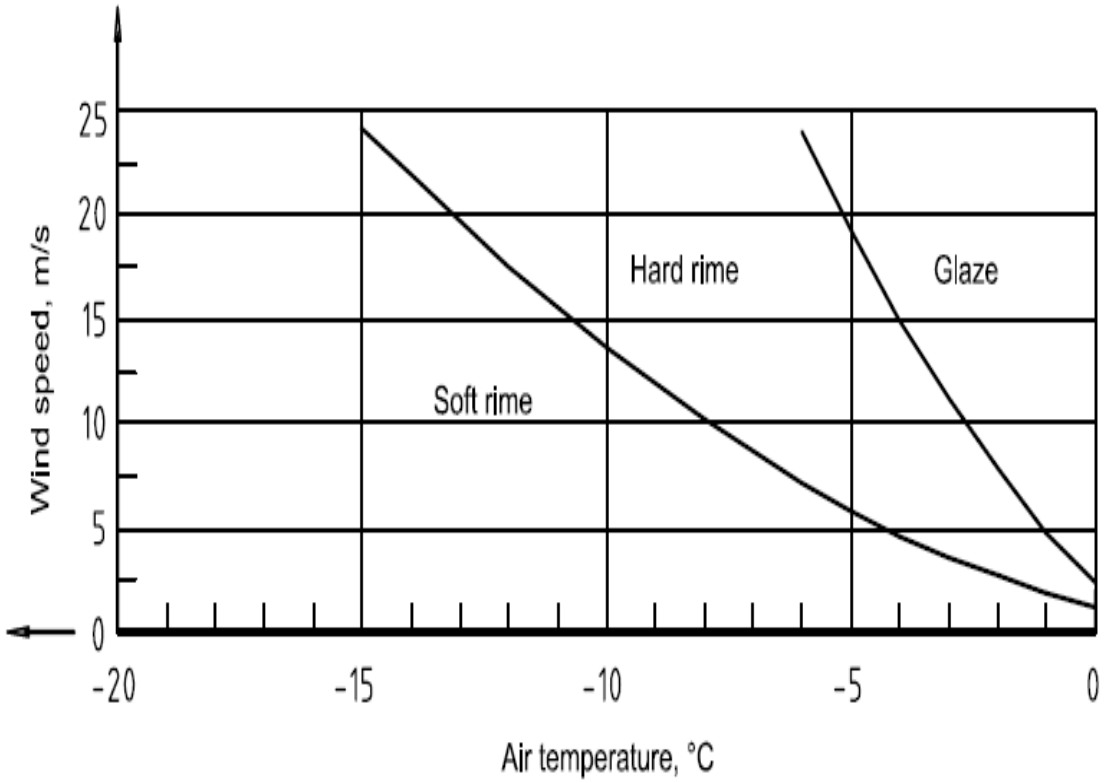

Figure 2.12: Types of accreted ice as a function of wind speed and air temperature (ISO, 2001b)

An empirical model for in-cloud icing depending only on the wind speed (Ahti and Makkonen, 1982) is given by:

$$I = 11 \times 10^{-3} \times u \tag{2.4}$$

It has been showed that linear relationship between wind speed and the constant given in equation (2.4) (Baranowski and Liebersbach, 1978). Out of standard measurement data, (Frohboese and Anders, 2007a) addressed a procedure to calculate the expected ice accumulation on wind turbines. It is clear from Figure 2.13 that mass of ice can be as heavy as the mass of the blade near the tip and it reduces to the third of mass of the blade near the root based on the ice accretion

load for a typical 2-MW wind turbine. This gives an idea on how big weight of ice that can be accumulated on wind turbine blades during icing events.

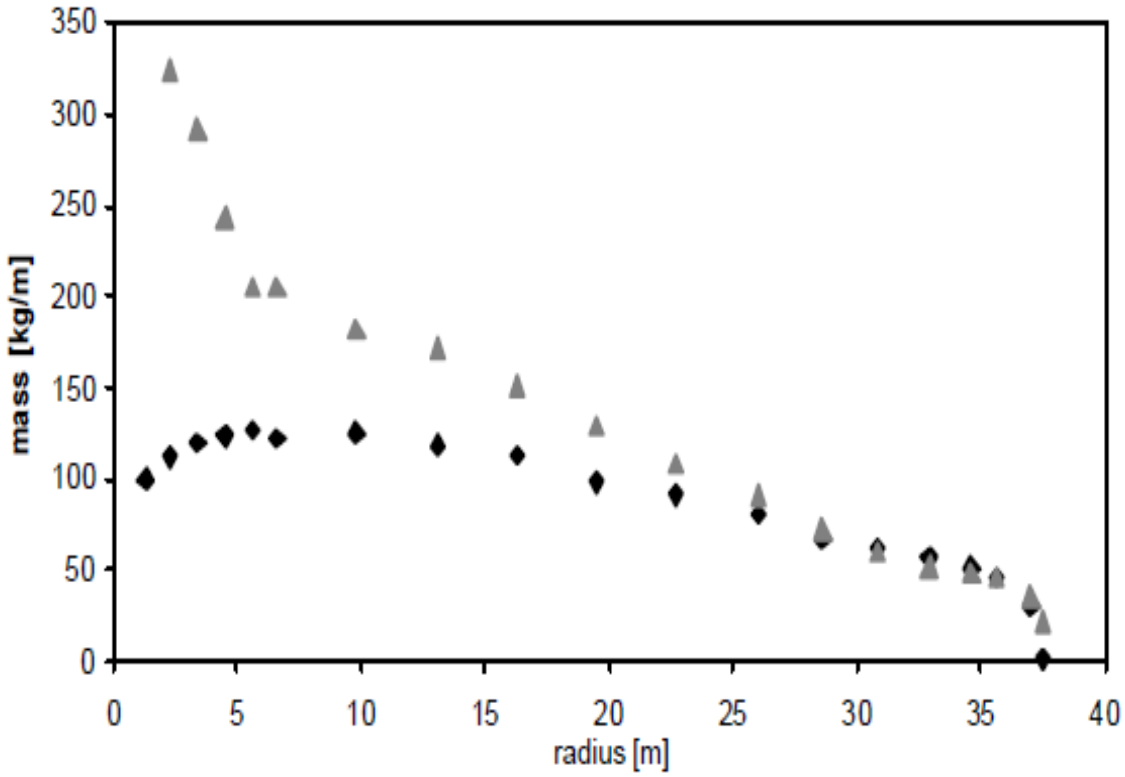

Figure 2.13: Blade mass (grey triangles) and the predicted maximum ice mass (black diamonds) over the blade length (Frohboese and Anders, 2007a)

The maximum thickness of ice built up at the leading edge can reach as high as 20 % of the chord length at that section (Seifert and Richert, 1997b). Typical leading edge ice accretion is shown in Figure 2.14. A tapered shape of accreted ice is noticed, where the maximum ice thickness is located near the tip. The mass of accreted ice is however less at the tip and more towards the root as the area of the leading edge is bigger away from the tip. Ice mass distribution at about 70% of the blade length starting from the tip and a tapered ice shape profile were recommended by (Antikainen P. et al., 2003) and (Lloyd, 2004).

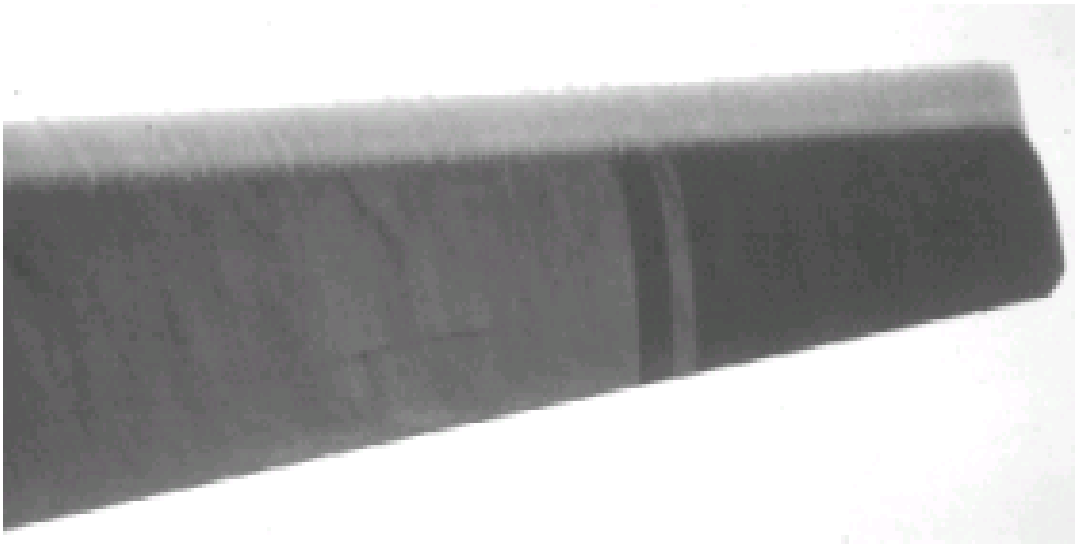

Figure 2.14: Typical leading edge ice accretion (Seifert and Richert, 1997b)

Glaze is relatively transparent, hard and sticks well to the exposed surfaces. This type of icing is usually encountered during severe ice storms (Makkonen, 2000). The accretion rate varies with wind speed, air temperature and rate of precipitation and is most often formed at temperatures between 0°C and –10°C (ISO, 2001a).

Rime ice is a common type of ‘in-cloud icing’. The stability and intensity of this type of ice accretion is dependent on several local variations in cloudiness, wind speed, air temperature, size and rate of the super cooled water droplets, height of the cloud base. Geographical location and its elevation are crucial for the probability and frequency of rime ice accretion on a given site, while observation of air speed and temperature can be used to estimate the number of days on which rime accretion takes place. Rime ice may be soft or hard. It is more difficult to remove hard rime from wind turbines especially the blades (Andersen et al.,

2011). 'rime' characteristics begin to approach those of glaze 'hard rime' when ambient temperatures approach zero, (Walsh, 2010).

2.3.5 Heavy Icing on Wind Turbine Blades

The heavy snowfall is a feature of many Polar Regions and repeated especially in the winter time. Large amount of ice is accreted on the exposed objects of the wind turbines. (Haaland, 2011) investigated the power loss due to heavy icing in the winter season 2009-2010 at Aapua, Sweden. He presented the ice load and the power loss of 1.4-MW wind turbines in a selected wind farm in Table 2.1.

Table 2.1: Ice accretion load and power losses on 1.4 MW wind turbine (Haaland, 2011)

Month	Loss of Energy [%]	Ice load/Turbine [kg/m]
October	9.9%	245.7
November	37.8%	424
December	12.3%	216
January	52.5%	686.7
February	18.5%	174

During NREL 5-MW wind turbine simulation research in a Scandinavian region, (Lehtomäki et al., 2012) found that ice mass on the wind turbine blade would be 40 kg/m. It is however worth noting that the simulation for the wind turbine was only for three and half hours for the assumed icing event. One can imagine the tremendous amount of ice that could accumulate by exposing wind turbine blade to severe icing condition when blizzard stays for days. According to an annual

report of International Energy Agency (IEA) (Ronsten et al., 2012) which stated that on the highest Norwegian coastal mountains the icing load on wind turbine blade can reach up to 50 kg/m. It is known that some other Scandinavian regions experience more severe weather conditions. (Walsh, 2010) investigated the results of modelling the load severe icing case of 200 kg/m on the blades of a stationary 100-kW wind turbine. In their empirical model (Frohboese and Anders, 2007b), the ice load reached 135 kg/m (about 7 m away from the root of blade) based on assumed icing event lasted for one week. The maximum assumed mass of ice in the simulation is about 68% of the mass of the blade itself.

2.4 Rotating Machinery

Wind energy is one of the fastest developing renewable and clean energy sources (Mathew and Philip, 2011). In the near future renewable energy generators such as wind turbines will play a significantly increasing role in the generation of electrical power. Many encouraging sites for wind farms in terms of higher wind speeds are mostly located in cold, wet regions such as the Alps, Canada, and the northern Scandinavian coastline. Installation and operation of wind turbines in such cold regions is facing the problems of ice accumulation on its components, especially the blades. Ice accretion on wind turbine blades increases the overall load causing serious structural problems. The continuous process of ice accretion is generally affected the wind turbine lifespan and structural integrity, in particular the blades and the tower.

Rotation can be defined as a progressive radial orientation to a common point which lies within the axis of motion. That axis is 90º perpendicular to the plane of

the motion. Rotating machinery is the general grouping of mechanical machine that is used for adding kinetic energy to a process. The additional kinetic energy is needed to move machine connecting parts continuously from one point to the next. For wind turbines, it means maintaining rotation of blades as smooth as possible. Preventing vibration is however an impossible task because rotating machinery inherently creates vibration.

When dealing with rotating blades of wind turbine, it is important to give specific definition for a turbine. A turbine may be defined as a rotary engine that extracts energy from an incoming fluid flow. A simple turbine has one moving part and rotor blade assembly. The moving fluid acts on the blades to rotate them and convey energy to the rotor. Next sections will deal with rotating criteria especially for wind turbines.

2.4.1 Dynamic Effects on Rotating Blades

The analysis and design of structures that support or resist loads behaviour refers to what known as the structural approach, this is mainly to examine the structures response to certain excitation forces. The dynamic behaviour of these structures can be determined by their individual components and the interactions between them. Both of rotating and non-rotating structures can be studied by the virtue of modal analysis which is basically a study the dynamic properties of structures under vibrational excitation (Gutierrez, 2003, Ewins, 2003).

Natural frequency of any system is the frequency with which the system oscillates freely once set into motion in the absence of any external force. These

frequencies are usually dependent on the basic characteristics of the structure such as stiffness, density, and geometry (Tartibu et al., 2012). (Maalawi and Badr, 2010) studied the problem of possible resonance because of the blade pitching motion, the authors considered an optimized model for the wind turbine blade based on the reduction of the vibration by maximizing or separating the natural frequencies from the pitching mechanism at the wind turbine rotor hub.

The effect of tapering on the natural frequencies of the beam is examined by (Bazoune, 2007). This investigation takes into account the effect of tapering in two planes and shows that the first natural frequency increases as taper ratios increase. Also reported in the research is that the increase of the hub radius leads to an increase in the first three natural frequencies. The rotation will induce a stiffening effect leading to an increase of the natural frequencies.

(Das et al., 2007) concluded in their study that dynamics of rotating beam under a relatively high rotational velocity differs from that of non-rotating one because of the centrifugal stiffness addition during rotation. Flexible beams usually become stiffer when they are subjected to high speed rotation, this is due to the axial- bending coupling related to large displacements of the beam cross-section (Piovan and Sampaio, 2009). The thick beam theory was investigated by (Chen and L-W., 2001). They emphasized that for thick blades, the rotary inertia and transverse shear deformation need to be included in the vibration analysis as illustrated in the Timoshenko beam theory.

Finite Element Method (FEM) is widely used as a powerful numerical tool to analyse various engineering aspects including dynamics of rotating blades. A

hierarchical finite element model ,which uses fewer elements to obtain a better accuracy, was presented by (Ghayoura et al., 2010) for the flapwise bending vibration analysis of a tapered multi-layered composite rotating beam.

(Chen and Peng, 1995) used the (FEM) to investigate the effect of rotation speeds and geometric non-linear reference amplitudes on the dynamic stability of a rotating blade. Reference amplitude is the ratio of maximum amplitude to the length the blade. In their study, the Lagrangian's approach was used to derive the equations of motion. The same approach and a Galerkin finite element method are implemented to study the dynamic stability of a rotating blade subjected to axial periodic forces.

The wind turbine blades may be treated as flexible bodies (components) attached to moving base, which is the rotor. The next section will focus on the dynamic effects on wind turbines.

2.4.2 Dynamic Effects on Wind Turbines

Recently, the multi-MW wind turbines are getting more dominant; the dynamic behaviour of such huge machines is becoming more important. Understanding their dynamic analysis gives enough knowledge to improve efficiency for the thriving wind turbines industry. In accordance to structural design process, a wind turbine should be analysed under various loads may experience during its life. The first intention is to make sure that the wind turbine is capable to support the loads with adequate safety margin. In this section, detailed survey will be given to have better understanding of the methods used in analysing the dynamic effects on wind turbines.

In the two-parts paper, (Bazilevs et al., 2010) numerically presented a successful application to model and simulate a wind turbine rotor . In Part 1 of the paper, the authors focused on the basics of geometry modelling and construction analysis for wind turbine rotors. Figure 2.15 shows a CFD representation of the 5-MW wind turbine rotor. In Part 2 of the paper, the focus was on the blades of for wind turbine and the authors gave computational procedures details of the fluid–structure interaction.

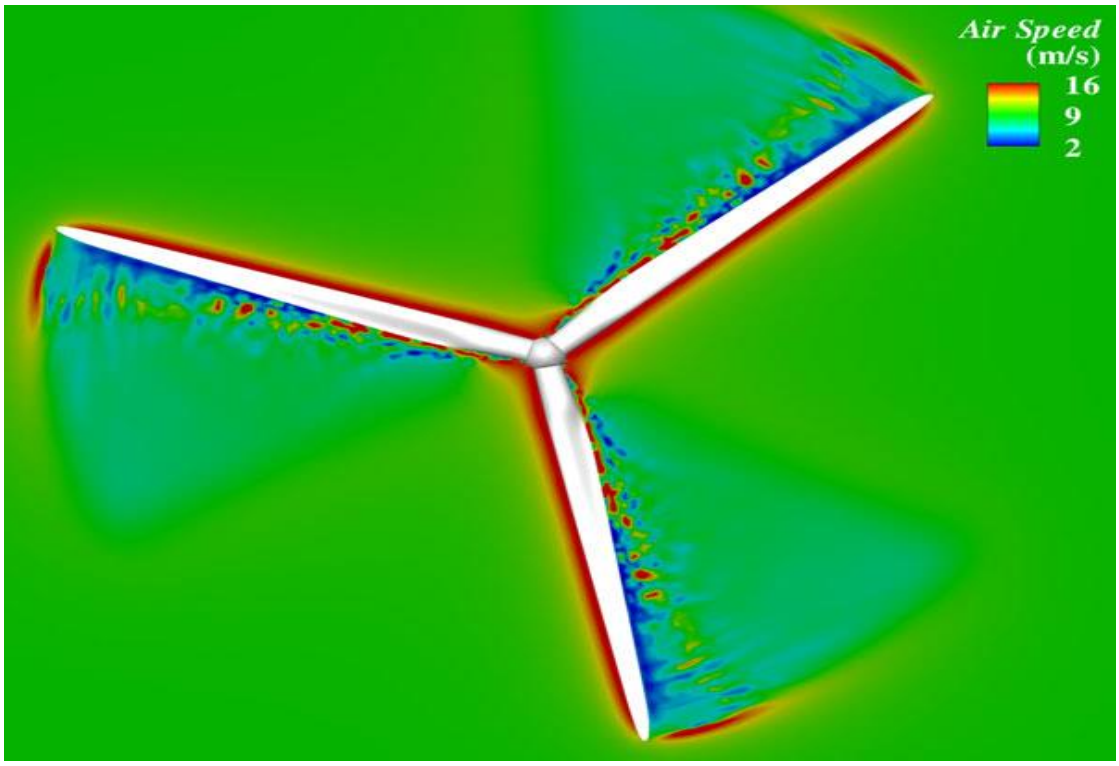

Figure 2.15: CFD representation of the 5-MW wind turbine rotor (Bazilevs et al., 2010)

(EswaraRao, 2012) has presented 3D CFD rotor computations of a 20 kW stall-regulated wind turbine with tip plate. The paper described a full three dimensional CFD modeling for the whole rotor assembly of the wind turbine by using Reynolds Averaged Navier-Stokes (CFD-RANS).

Analytical methods are widely used in studying various dynamic effects on wind turbine. (Choudhry et al., 2012) investigated analytically the effect of spacing of the wind turbines for both upstream and downstream wind turbine on the areas of a tandem wind turbine blade, as a result, no dynamic stall event was came across due to very small turbulence intensity.

Numerical results showed that the increase of the rotational speed of the wind turbine rotor lead to an increase in the first frequency of a wind turbine blade. (Wang et al., 2010) implemented mathematical model based on mixed flexible rigid multi-body to estimate the dynamic performance of a wind turbine. Figure 2.16 illustrates rotor's first two flap and edge bending mode shapes.

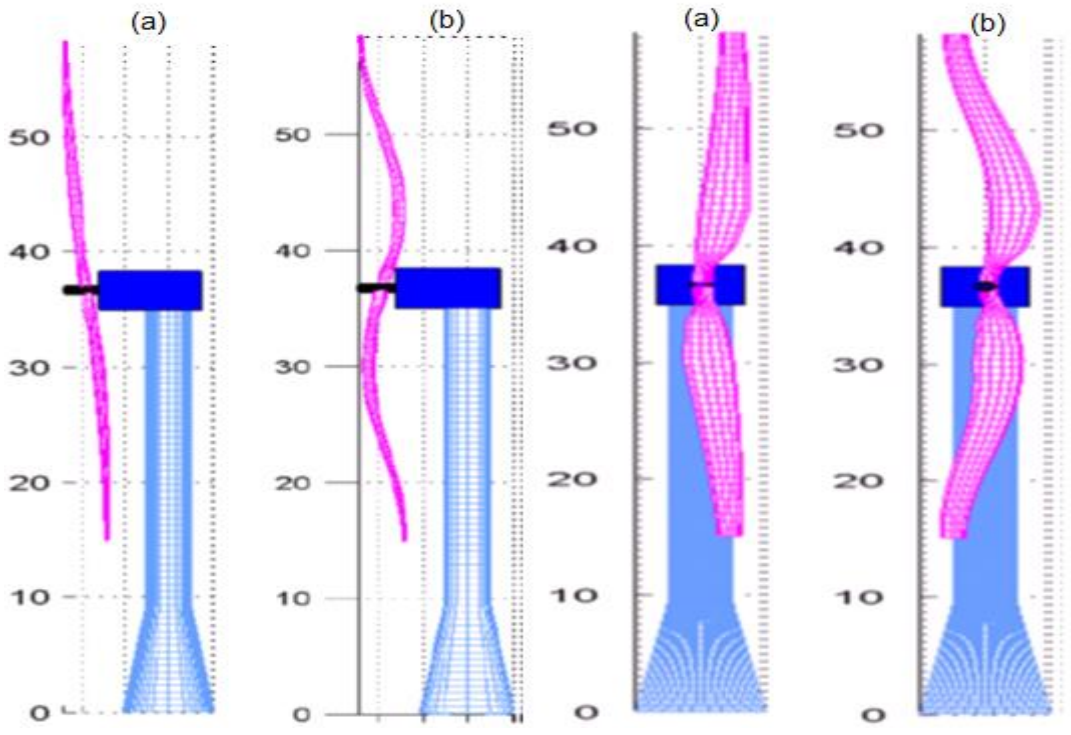

Figure 2.16: Rotor's first two symmetrical edge bending mode shapes(Right) and, Rotor's first two anti-symmetrical flap bending mode shapes (Left) (Wang et al., 2010).

(Larsen et al., 2002, Kim and Kim, 2011) investigated the vibrational behaviour of wind turbine blades by modal analysis, the authors extracted natural frequencies, mode shapes for the blades. Based on Glauert's blade element momentum propeller theory, (Lanzafam and Messina, 2007) implemented a mathematical model for a wind turbine optimization .

Turbulence effects and rotational on a wind turbine blade had been studied by (Sicot et al., 2008). The authors intended to experimentally evaluate the turbulence and rotation effects on the aerodynamics of a wind turbine blade, focusing particularly on stall mechanisms. A 1/16-scale model of high performance 1500 kW wind turbine blade was tested in a suitable wind tunnel and the computational results experimentally validated. Moreover, the aerodynamic performance of the scaled blade was calculated by using both free-vortex method (FVM) and (CFD) method. Wake geometry is shown in Figure 2.17. The smooth shape of the wake can be disturbed by changes occurred to the blade profile like ice accretion on the leading edge.

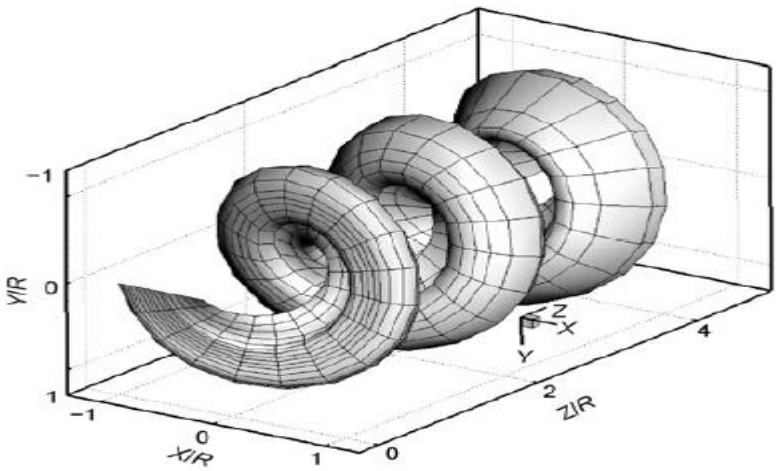

Figure 2.17: Wake geometry by Free Vortex Method FVM (TongGuang et al., 2012)

It is clear from above discussion that different techniques have been used to study and analyse dynamic effects on wind turbine. It is worth mentioning that some software such as ADAMS and FAST are specifically developed for wind turbines both for structural and aerodynamic analysis.

2.4.3 Dynamic Effects on Iced Wind Turbines

The effects of accreted ice on mechanical behaviour of wind turbines have received wide attention, especially in recent years. The Alpine terrain is suitable for the construction wind turbines due to the gainful wind resource and less heavily populated areas (Rindeskär, 2010). At the same time, the severe weather conditions possess a real challenge to the wind power industry since icing of the wind turbine blades and sensors may induce losses in production, increasing in the wear and tear of the different components, leading to serious structural integrity problems and hence reducing the expected economical outcome.

(Fu and Farzaneh, 2010) introduced a CFD procedure to simulate the ice accretion process on a rotating wind turbine blade. The authors found that the rotational speed of the turbine has a major impact on the amount of accreted ice on the blade. Increasing in the rotational speed leads to an increase ice thickness.

2.4.4 Stress Amplification in Wind Turbine Due to Icing

Low temperatures usually have harmful effects on the materials of the wind turbines. Structural elements including composite material and steel change their mechanical properties when working at low temperatures. Steel tend to be more brittle with reduction in its capacity of deformation and energy absorption,

composite materials fiber will subjected to more residual stress due to unequal shrinkage. With sufficiently high residual stress, micro-cracking will probably initiate in the material. These initiated micro-cracks decrease both the impermeability and the stiffness of the material leading to accelerate the undesirable deterioration process as explained by (Dutta and Hui, 1997) and (Lacroix and Manwell, 2000).

Other effects of low temperatures on wind turbines are the changes in the dimensions and oil viscosity of different components resulting in possible overheating and considerable reduction in lifetime ((Botta et al., 1998), (Laakso and Peltola, 2005), (Seifert, 2003), and (Tammelin, 2005)).

Icing of the rotor blades or other components of wind turbines as shown in Figure 2.19 will lead to an increase in the edgewise vibrations and resonance may occur due to changed natural frequencies (Tammelin et al., 1998).

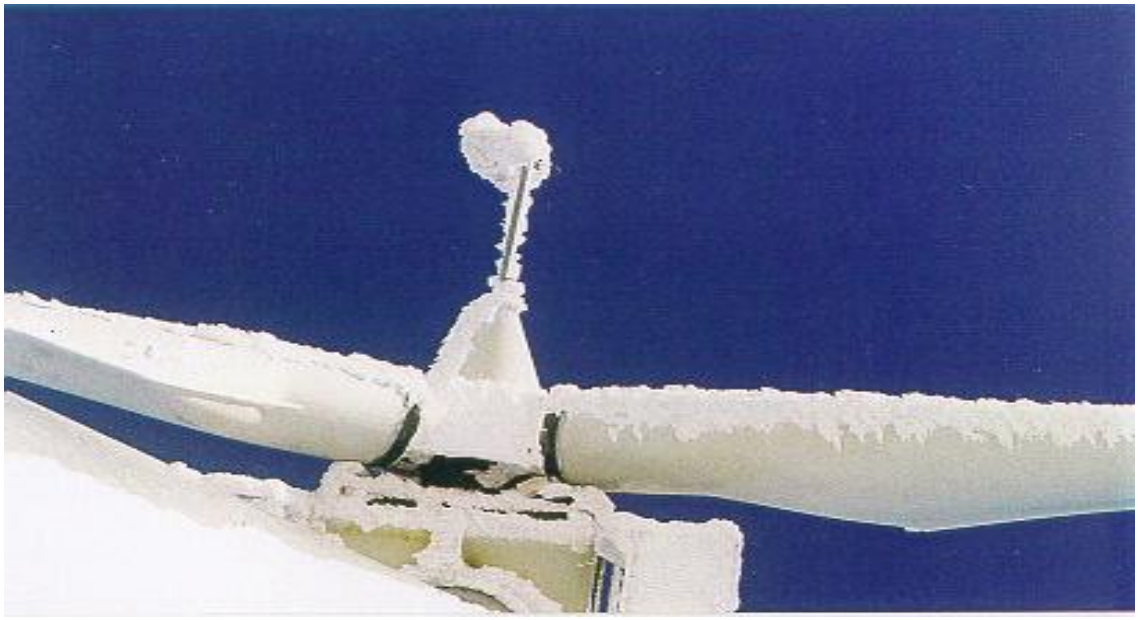

Figure 2.18: Accumulating of ice on the leading edges of a 150-kW wind turbine in Switzerland (Tammelin et al., 1998)

Accreted ice significantly increases the bending moments of the wind turbine blade, (Gallardo, 2011) found that the maximum stresses occurred in the root area of the blade. On the other hand, ice accretion affects the fatigue performance of the wind turbine blade and creates complex load cycles. In their book, (Burton et al., 2011) investigated several aspects of wind turbine including structural effects on wind turbine blade. Figure 2.20 illustrates the “close to failure blade” near the root due to excessive stress accumulation.

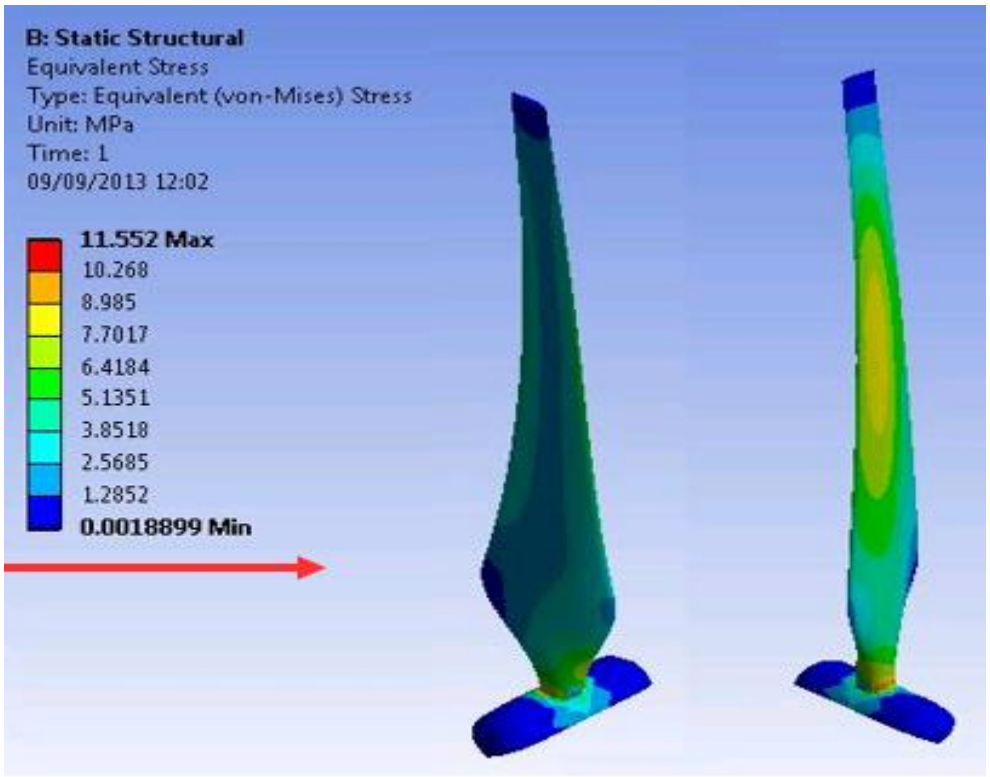

Figure 2.19: Finite element analysis showing areas near the root closest to failure (Sweeney, 2015)

The natures of wind turbine fluctuating loads cause variable amplitude fatigue loading on wind turbine (Pollino and Huckelbridge, 2007). As ice loading becomes one of the important overall general loadings on wind turbines, it should

be considered, in certain cold regions, as a major threat to be taken care of not only for the fatigue and internal stresses issue, but also as fundamental structural load.

2.5 Vibration of Wind Turbine Blade

2.5.1 Overview of Applied Methodologies for Wind Turbine Vibration Analysis

As the wind turbine blades start to rotate from rest, their rotational speed increases accompanied with an increase in the vibration frequency. For a robust design, maximum rotational speed which is very close to the natural frequency of the system must be avoided because this will result in a high like hood of resonant amplification leading to structural instability. Furthermore, rotational speed shouldn't be very close higher natural frequencies of the system under consideration. Both of previous cases will end up with an uncontrollable violent near resonance vibrations by speeding up-to-down from maximum speed. This may lead to catastrophic damages to the whole structure due to very high dynamic forces. It is a good practice to maintain the operational frequency away from the vicinity of the natural frequency with a safety margin of 15% of the natural frequency as recommended by (Satari and Hussain, 2008) for wind turbines of moderate power output (100-225 kW)**.**

2.5.2 Numerical and Analytical Based Vibration Methods

Recently, the ready and available high speed computers and various efficient software packages have a great influence on the numerical solutions for various

engineering fields. Analytical skills were commonly used in the past to solve most of the important engineering problems, such as vibration analysis. Nowadays, by the virtue of modern computers, access to huge amount of computation power is just under the researcher's fingertips, but they need to fully grasp the physical nature of the engineering problem and be able to interpret the computations outcome. In this section, a review of the most useful numerical methods related to the research in this project will be carried out.

Several analytical based vibration methods have been used to analyse the dynamic behaviour of wind turbine blades. These include a solution based on the properties of a Hermitian operator which has always real Eigen values, and its orthogonal basis vectors (Cobble and Fang, 1976). The Extended Galerkin Method has been used for converting continuous operator to a discrete problem (Liu and Ren, 2011). By the implementation of finite element method, the dynamic stability of an axially loaded rotating shaft was studied, Timoshenko's beam theory was used by (Chen and Ku, 1990) to investigated the transverse shear effect.

(Bazoune and Khulief, 1992) conducted a vibrational analysis of a rotating tapered beam, the authors included rotary inertia and shear deformations in their analysis. (Attarnejad et al., 2006) derived an exact solution for the free vibration of a tapered Euler–Bernoulli beam by the well-known Bessel functions using FORTRAN90.

Numerically, the method of harmonic superposition was used by (Arrigan et al., 2011a) to simulate the fluctuations of the wind velocity time histories. The

aeroelastic response and performance of a 5-MW Class rotating composite blade model was examined by numerically advanced coupled method based on (CFD) and the computational flexible multi-body dynamics (CFMBD) (Kim and Kim, 2011). Results showed that for rotation speed of 13 rpm the values of natural frequencies of the first four fundamental modes of vibration were 0.74 Hz, 1.14 Hz, 2.22 Hz and 3.85 Hz respectively as illustrated in Figure 2.21. All values seemed to be slightly higher than those given in the NREL technical specification report in (Jonkman et al., 2009) due to rotational effect.

Figure 2.20: Four vibration bending modes for a typical wind turbine blade: (a) 1st Flapwise bending, (b) 1st Edgewise bending, (c) 2nd Flapwise bending, (d) 2nd Edgewise bending. (Kim and Kim, 2011)

2.5.3 Experimental Based Vibration Methods

Experimental methods are widely used to analyse vibration problem of wind turbines blades ((Hansen et al., 2006), (Arrigan et al., 2011b)). The modal damping of a wind turbine was estimated by ((De-jin et al., 2007), (Hansen, 2003)). (Hansen et al., 2006) experimentally investigated two different methods for approximating the modal damping of a working wind turbine. Dynamic signal analysis was experimentally implemented by (Zhiquan et al., 2001) to extract modal parameters, this is done by measuring the vibrations at different positions along the wind turbine blade surface. A study of numerical and experimental vibration on the reinforced glass fiber polyester composite wind turbine blade had been carried out to optimize its dynamic properties (Attaf, 2010).

2.5.4 Monitoring and Mitigation of Wind Turbine Vibration

Lots of efforts have been made to monitor and mitigate wind turbine vibrations. These include using a tuned mass damper (TMD) which is passive control device mainly used to mitigate wind turbine wind forced vibrations (Murtagh et al., 2007). (Arrigan et al., 2011b) conducted an research about the use of semi-active tuned mass dampers (STMDs) to reduce the vibrations of the wind turbine blade in the flapwise direction, the research also investigated the effect of centrifugal stiffening on the deviation of the natural frequencies of wind turbine blades.

In order to mitigate icing effects on wind turbine blade de-iced and anti-icing methods are used. De-icing means that the ice is allowed to build up before it is being removed. The wind turbine need to be stopped to remove the accreted ice,

which usually not an easy task specially in harsh weather conditions. The use of de-icing method is usually consumes about 5% of the rated power of the wind turbine, while by adopting the anti-icing method requires much higher power reaches up to 25% of the turbine rated power, this method basically prevents ice from building up during the normal working of the wind turbine (Ronsten, 2008).

(Kraj and Bibeau, 2010) proposed a possible solution for wind turbine blade the glaze ice accretion by the use of hydrophobic coatings, and the use icephobic coating with the case of rime ice accretion.

A new approach for stability investigations of wind turbines was presented in (Rosenow and Andersen, 2010)**.** To observe the vibration behaviour of the wind turbine a structural vibration monitoring system was used (Zhang, 2009). The system analysed wind turbine vibrations and developed nonlinear and nonparametric models to optimize wind turbine performance and to reduce vibrations of the tower and the turbine's drive train. Fault detection system (FDS) and condition monitoring system (CMS) were also implemented in order to keep the wind turbine in safe operation. Recently, after the introduction of the multi-MW wind turbines, photogrammetry was used in monitoring the dynamics of large wind turbines (Ozbek et al., 2010), this was mainly done by charge-coupled device (CCD) cameras to capture the response of various components of the wind turbine.

2.5.5 Vibration of Wind Turbine Due To Icing

Modern wind turbines are constructed of slender and elastic parts such as the rotor blades and the tower. Such structures are extremely exposed to vibration.

In addition, due to cyclically alternating rotor forces, rotor-blades system is prone to certain excitations causing dangerous vibrations. The problem becomes seriously important when combined with the accumulation of ice on different components of the wind turbines, especially on the blades. For this, it's important to conduct a vibrational analysis including extracting of natural frequencies and mode shapes for clean and iced wind turbine blades and to study the possible associated resonance problems.

The complex terrain locations have some problems on the wind power harvest process,(Manuel et al., 2001) statically investigated this effect by the use of flap and edge bending of a commercial wind turbine blade. Different algorithms, methodologies and techniques reviewed by (Hameeda et al., 2009) to monitor the performance of various operations of wind turbine to avoid disastrous conditions such as unexpected breakdowns.

Potentially large structural displacements can result from a resonance condition. Therefore, operating at a critical rotor speed could be particularly damaging to the wind turbine system (Osgood, 1998). By the use of Universal Resonant Excitation (UREX), an experiment was conducted by (Farinholt et al., 2012) to examine the structural health of an NREL wind turbine blade by steadily increasing the excited design load until reaching failure.

Higher altitudes represent excellent sites for wind farm installation to capture wind power due to the increase in air density at lower temperatures and wind speed slightly increases by 0.1m/s per 100m for the first 1km of altitude (Fortin et al., 2005). (Staino et al., 2012) discussed actuator control of edgewise vibrations.

(Lin et al., 2008) modelled bending vibration of the blade and the influences of the pre-cone angle and the angular speed on the natural frequencies. Structural vibration of large-scale wind turbines considering periodically time-varying parameters was addressed by (Kim and Lee, 2011).

(Tartibu et al., 2012) conducted a vibrational analytical study using MATLAB of a variable length wind turbine blade. (Gürsel et al., 2012) also analytically investigated the characteristics of wind turbine blades by implementing the Rayleigh's method. The authors tracked the resonance zone and the working frequencies of the system. (Park et al., 2010) proposed a method based on a derivation of the equation of motion of a rotating wind turbine blades to predict the vibratory behaviour of the rotating blade.

It should however be noticed that none of which has dealt with the problem of vibration due to ice accretion. Hence the research in this project will fill the void in the world of knowledge in this field.

2.6 Summary

It is clear from the above literature review that atmospheric icing has a major impact on the performance of the wind turbine. The previous studies generally focused on the following aspects:

1- Energy loss due to atmospheric icing.

2- Hazard of ice shedding and ecological issues.

3- Economic losses due to shutdowns during icing events.

4- Aerodynamic behaviour of an iced wind turbine blades

5- Stress amplification due to atmospheric icing on wind turbines

However, no attention was found, so far, to the problem of vibrations of wind turbine blade due to atmospheric icing. It was interesting to notice from the survey of literature that in spite of the importance issue of the vibration due to atmospheric icing, which can directly influence the structural integrity of wind turbines, this hasn't been fully investigated. It has also been noticed that, while significant power loss has been reported for the wind turbine due to atmospheric icing, no systematic research has been carried out on its impact on aerodynamic performance of wind turbine blade under different weather conditions.

The current research was undertaken with the purpose of investigating the dynamic performance of the blade under three different icing scenarios and to fill the gap concerning those important issues mentioned above for the ongoing industry of wind energy.

CHAPTER THREE

RESEARCH METHODOLOGY

Atmospheric icing is considered as a major problem in many cold region for the wind energy industry and results in considerable loss in wind turbine performance. The aim of this research is to develop a further understanding of the effect of atmospheric ice accretion on the structural integrity and aerodynamic performance of wind turbine blades through numerical investigation to address the challenges facing the industry. Figure 3.1 illustrates the flow of the research methodology.

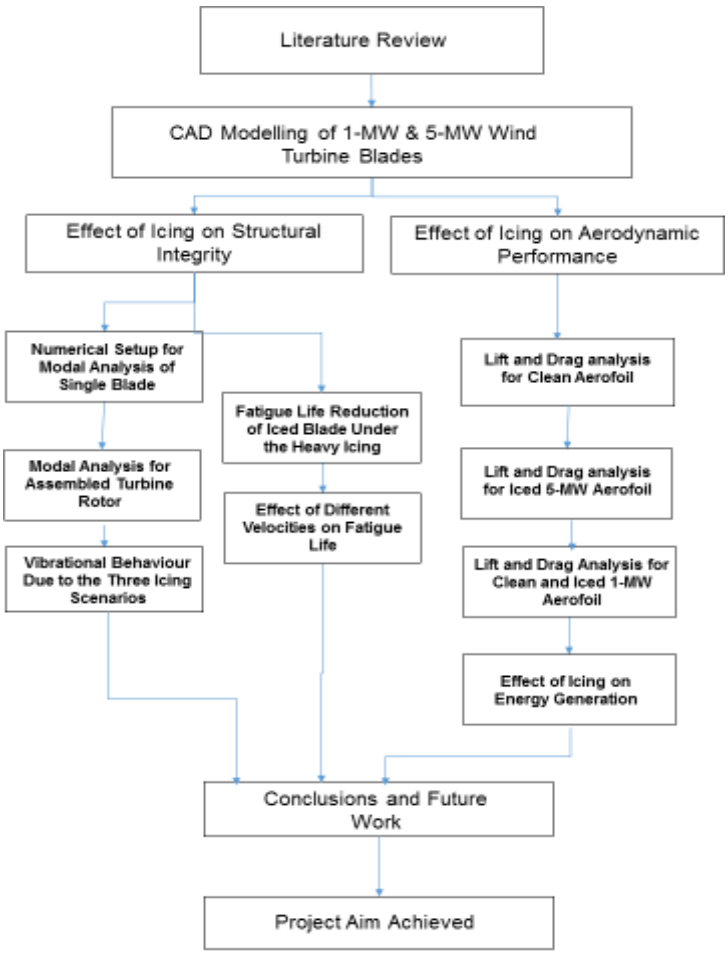

Figure 3.1: Flowchart of the research methodology for the project.

A 5-MW wind turbine is chosen for this study due to availability of geometric design and performance parameters. The geometric parameters are the dimensions ‘coordinates and angle of twist’ and they are used to build the CAD model of the blade in Chapter four. The mass of the blade was compared to the mass of the modelled blade, also natural frequencies for the first three modes have been used to compare numerical results in chapters four through six. After getting the, geometric design parameters of the blade, a computer aided model is established. This is achieved using a commercial CAD solver ,’Rhinoceros 5’, which is a popular software for 3D design recommended by many designers for the design of wind turbine blades (Hartwanger and Horvat, 2008, Monteiro et al., 2009).

Building the CAD model of the wind turbine blade is a first step for modal analysis and CFD simulation for its dynamic performance under various icing conditions. A method will be developed to estimate the on-blade accreted ice mass and thickness on the basis of ISO Standard 12494. The method will be applied to estimate the accreted ice mass on a 5-MW wind turbine blade under three icing scenarios. For the problem of modal and stress analysis, ANSYS is chosen in this research due to the recognition of many researchers in this field (Rathore and Ahmed, 2011, Murtagh et al., 2004). The finite element analysis tools from ANSYS provide the ability to simulate most of the structural aspects including modal analysis for vibrational characteristics. The CAD file is exported to the APDL environment of ANSYS14.5 and modal analysis will be performed to determine natural frequencies for both the clean and iced turbine blade. The modal analysis will also be conducted for the assembly of three modelled blades with a proper hub in ANSYS14.5 WORKBENCH environment. The effect of ice

accretion on the vibrational behaviour of the blade and the rotor under three icing scenarios will be examined by comparing the results of clean and iced conditions.

To investigate the effect of atmospheric icing on the structural integrity of the wind turbine blade and its rotor, stress analysis will be performed in the ANSYS APDL environment. Von Mises stress will be obtained for clean and iced blade and reductions of fatigue life of the blade will be estimated for heavy icing conditions, this will be done for two different wind velocities regimes. The effect of atmospheric icing on the structural integrity of the wind turbine will also be assessed with the concept of dynamic magnification factor.

Finally, CFD analysis will be carried out to investigate the effect of atmospheric ice accretion on the aerodynamic performance of typical 1-MW and 5-MW wind turbine blade aerofoils. CFD software STAR-CCM+ is chosen due to its wide industrial acceptance (Pervez and Mokhtar, 2012). Results of the drag and lift coefficients and power production under different icing scenarios will be determined under different angles of attack. These results will be compared with those of the clean aerofoil profile to demonstrate the detrimental impact of atmospheric icing on energy harvest for the wind energy industry.

CHAPTER FOUR

NUMERICAL SETUP FOR STRUCTURAL ANALYSIS

4.1 Mathematical Description of Models Used

The equation of motion for a multidegree of freedom system can be derived from Lagrange's equation (Rao, 2004)

$$\frac{d}{dt}\left(\frac{\partial T}{\partial \dot{x}_i}\right) - \frac{\partial T}{\partial x_i} + \frac{\partial V}{\partial x_i} = F_i \qquad i = 1,2,\dots n \tag{4.1}$$

where F_i is the non-conservative generalized force corresponding to the ith generalized coordinate x_i and the generalized velocity $\dot{x}_i$ is the time derivative of x_i , T is the kinetic energy and V is the potential energy for a multidegree of freedom may be given in matrix form as

$$T = \frac{1}{2}\dot{\vec{x}}^T[m]\dot{\vec{x}} \tag{4.2}$$

$$V = \frac{1}{2}\vec{x}^T[k]\vec{x} \tag{4.3}$$

where $[m]$ and $[k]$ are the mass and stiffness matrices respectively and $\vec{x}$ is the column vector of the generalized coordinates

$$\vec{x} = \begin{Bmatrix} x_1 \\ x_2 \\ . \\ . \\ . \\ x_n \end{Bmatrix} \tag{4.4}$$

But by noticing the symmetry of the mass matrix $[m]$, we can get

$$\frac{\partial T}{\partial \dot{x}_i} = \frac{1}{2}\vec{\delta}^T[m]\dot{\vec{x}} + \frac{1}{2}\dot{\vec{x}}^T[m]\vec{\delta} = \vec{\delta}^T[m]\dot{\vec{x}}$$

$$= m_i^T \ddot{\vec{x}} \qquad i = 1,2, \dots n \tag{4.5}$$

Where δ_{ji} is the Kronecker delta ($\delta_{ji} = 1$ if $j = i$ and $= 0$ if $j \neq i$), $\vec{\delta}$ is the column vector of Kronecker deltas whose element in the row $i = j$ is equal to 1 and equal to zero for other elements in the rows for which $j \neq i$, and $\vec{m}_i^T$ is a row vector which is identical to the ith row of the matrix $[m]$, so equation (4.5) may be expressed as:

$$\frac{\partial T}{\partial \dot{x}_i} = \vec{m}_i^T \ddot{\vec{x}} \tag{4.6}$$

By differentiation of equation (4.6) with respect to time gives:

$$\frac{\partial}{\partial t}\left(\frac{\partial T}{\partial \dot{x}_i}\right) = \vec{m}_i^T \dddot{\vec{x}} \qquad i = 1,2, \dots n \tag{4.7}$$

It is important to notice that the mass is not a function of time while the kinetic energy is a function of the velocities $\dot{x}_i$ and so

$$\frac{\partial T}{\partial x_i} = 0, \qquad i = 1,2, \dots n \tag{4.8}$$

By taking note of the symmetry of stiffness matrix $[k]$, one can differentiate equation (4.3) as

$$\frac{\partial T}{\partial x_i} = \frac{1}{2}\vec{\delta}^T[k]\vec{x} + \frac{1}{2}\vec{x}^T[k]\vec{\delta} = \vec{\delta}^T[k]\vec{x}$$

$$= \vec{k}_i^T \vec{x}, \qquad i = 1,2, \dots n \tag{4.9}$$

Where $\vec{k}_i^T$ is a row vector identical to the ith row of the stiffness matrix $[k]$, the equations of motion in matrix form can be obtained by substituting equations (4.7) to (4.9) into equation (4.1) as

$$[m]\ddot{\vec{x}} + [k]\vec{x} = \vec{F} \tag{4.10}$$

where

$$\vec{F} = \begin{Bmatrix} F_1 \\ F_2 \\ . \\ . \\ . \\ F_n \end{Bmatrix} \tag{4.11}$$

For a conservative system, there is no non-conservative forces F_i, so the equation of motion will be

$$[m]\ddot{\vec{x}} + [k]\vec{x} = \vec{0} \tag{4.12}$$

By assuming the solution of equation (4.12) is in the form

$$\{x\} = \{x\}e^{j\omega t} \tag{4.13}$$

Where $j = \sqrt{-1}$ and ω is the frequency of vibration, by assuming that transverse vibrations $\omega = \omega(x, t)$, x was previously defined as the column vector of the generalized coordinates, hence both mass and stuffiness matrices in equation (4.14) are in the generalized form. Substituting equation (4.13) into (4.12) for non-trivial solution gives the equation of motion governing the free vibration of the wind turbine blade as:

$$([k] - \omega^2[m])\{x\} = \{0\} \tag{4.14}$$

As the value of x in equation (4.14) cannot be equal to zero and for a non-trivial solution, the determinate of the coefficient matrix must be zero. This gives:

$$|[K] - \omega_n^2\ [M]| = 0 \tag{4.15}$$

Equation (4.15) may be solved to get the natural frequencies $(\omega_i)$and associated mode shapes(Φ_i). The generalized mass matrix $[M]$ and the generalized stiffness matrix $[K]$ are given in the form

$$[M] = [\Phi]^T[\mathrm{m}][\Phi] \tag{4.16}$$

$$[K] = [\Phi]^T[\mathrm{k}][\Phi] \tag{4.17}$$

where $[\ \ ]^T$is the transpose of the matrix. The uncoupled differential equation of motion can be written by using equations (4.16) and (4.17) as:

$$[M]\{\ddot{x}\} + [K]\{x\} = \{0\} \tag{4.18}$$

The wind turbine blade is modelled by a cantilever beam with transverse vibrations. It is assumed that the beam is straight and different cross-sections relative to the beam axis remain flat and perpendicular. As a result of bending, the fibres of one layer of the beam are subjected to tension while those of the second layer are compressed. However, the neutral layer does not bear any deformation. These assumptions are known as the Euler-Bernoulli hypothesis (Meirovitch, 2001).

4.2 Single NREL 5-MW Non-Rotating Blade Numerical Analysis Setup

The numerical analysis setup for a typical 5-MW wind turbine blade is described based on blade coordinates from the manufacturer. The procedure has two steps, drawing the 3D-CAD model in Rhinoceros and then exporting the model to ANSYS-14.5 in order to perform modal analysis of the wind turbine blade.

In this step, the CAD model will be set up. Typical 5-MW wind turbine blade aerofoil profile coordinates were imported from Excel files to Rhinoceros as Comma Separated Values (CSV). The coordinates of the blade were given for seventeen sections in spanwise direction to simulate the blade. Spacing and orientation of different aerofoil sections were given in the 5-MW reference guide (Jonkman et al., 2009). The blade has been strengthened by two shear webs in the middle of the sections. The coordinates of the blade section are given in Table 4.1 (Virk et al., 2012).

Table 4.1: NREL 5-MW wind turbines blade geometric

Section	Blade Radial Location (m)	Chord Length (m)	Twist (degree)	Aerofoil Table
1	4.37	3.542	13.308	Cylinder
2	7.10	3.854	13.308	Cylinder
3	9.83	4.167	13.308	Cylinder
4	13.25	4.557	13.308	DU 40
5	17.35	4.652	11.480	DU 35
6	21.45	4.458	10.162	DU 35
7	25.55	4.249	9.011	DU 30
8	29.65	4.007	7.795	DU 25
9	33.75	3.748	6.544	DU 25
10	37.85	3.502	5.361	DU 21
11	41.95	3.256	4.188	DU 21
12	46.05	3.010	3.125	NACA 64618
13	50.15	2.764	2.319	NACA 64618
14	54.25	2.518	1.526	NACA 64618
15	57.66	2.313	0.863	NACA 64618
16	60.40	2.086	0.370	NACA 64618
17	63.13	1.419	0.106	NACA 64618

Figure 4.1 illustrates the 17 aerofoil sections of wind turbine blade as drawn in Rhinoceros. Spacing of the sections was given in Table 4.1 as the differences between sections radial location.

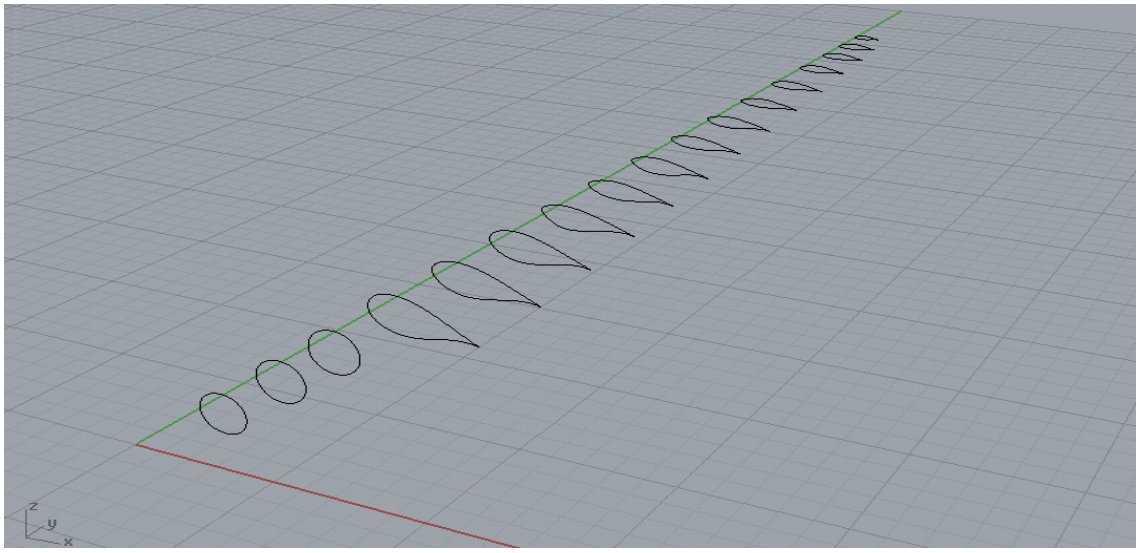

Figure 4.1: Aerofoil sections of the 5-MW wind turbine blade drawn in Rhinoceros

The 3D modelled blade with all aerofoil sections is illustrated in Figure 4.2. The CAD model is now ready to export to ANSYS environment to perform the needed structural and CFD analysis.

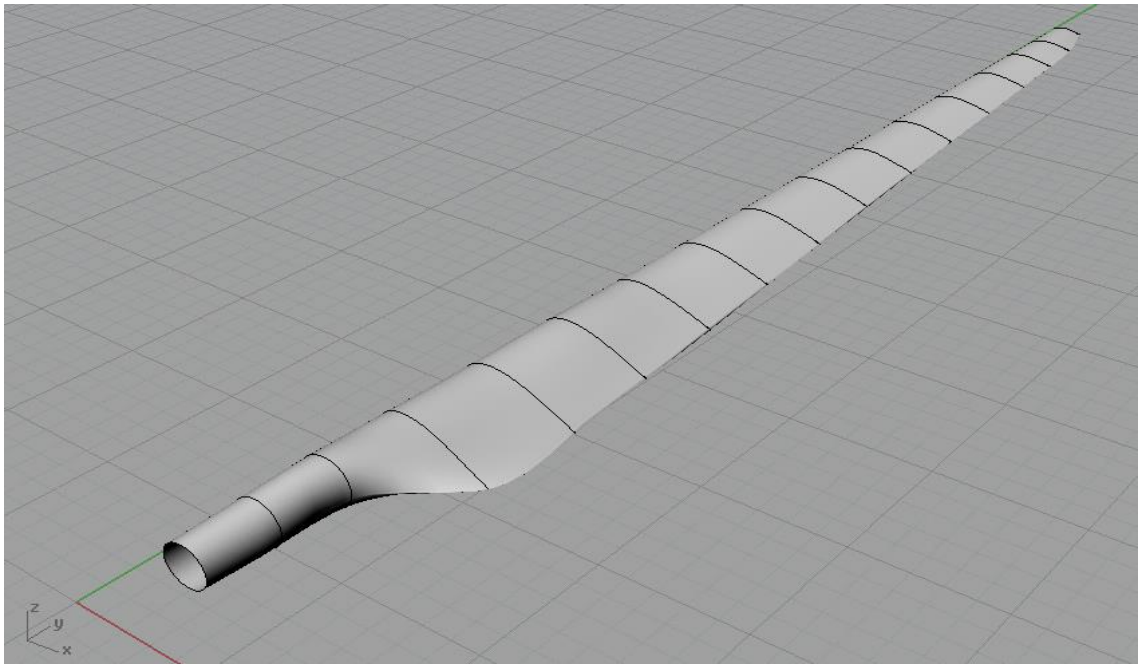

Figure 4.2: The 3D-CAD model as appears in Rhinoceros

4.2.1 Numerical Setup Including the Boundary Conditions and Other Operating Conditions

After setting up the 3D model with CAD software (Rhinoceros 5), the next step is to export it to the finite element software (ANSYS 14.5) as Initial Graphics Exchange Specification “IGES” file.

Element type SHELL63 was selected to model the blade. SHELL63 has both membrane and bending abilities to take both the in-plane and out of plane loads. As for the degrees of freedom, the element has six degrees of freedom at each node: rotations about the nodal x, y, and z-axes and translations in the nodal x, y, and z directions, stress stiffening and large deflection capabilities are also included.

4.2.2 Numerical Model for a typical wind turbine blade

A typical 5-MW wind turbine blade was modelled by using real coordinates of the 17 sections acquired from (NREL) (Jonkman et al., 2009). The cross-sections of the blade are twisted by 13º for the fourth section to 0.11º for last section at the tip. The coordinates of the blade section were given in Table 4.1 (Virk et al., 2012).

From the structural point of view the blade is normally hollow. The outer geometry of the blade usually consists of two shells one on the upper side (suction side) and another one on the lower side (pressure side), it is also strengthened by two structural shear webs, fitted to join the two shells together as shown in Figure 4.3.

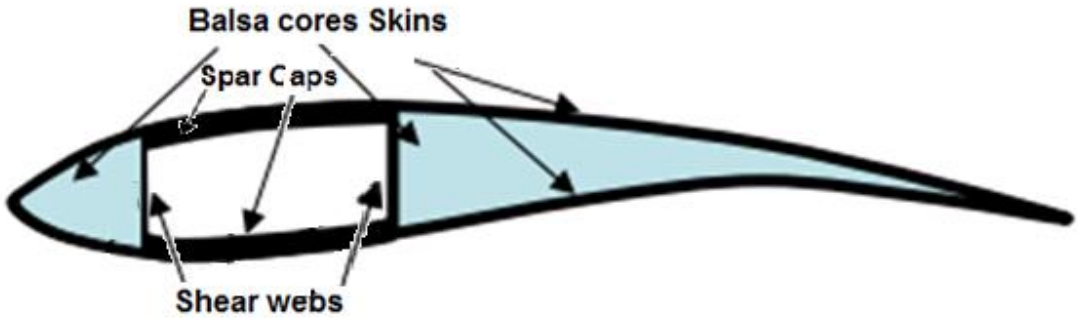

Figure 4.3: Cross section of a typical wind turbine blade (Griffin and Ashwill, 2003)

The wind turbine blade is treated as a cantilever beam mounted on the rotating hub along with two other blades for the three-blade wind turbine design. The boundary conditions for a cantilever beam were applied during ANSYS analysis. The longitudinal box-shaped spars with the outer upper and lower shells support the main loads usually acting on the blade. Wind turbine blades are tapered from the root to the tip along the span this is mainly to reduce the maximum bending moments which lies at the root and increasing the power captured from the wind.

The blade is twisted to lower the required torque for self-starting of the rotor while maintaining optimal wind angle of attack for the rotation process. Moreover, blades are required to maintain an optimum cross-section profile for aerodynamic efficiency in order to generate maximum torque required to drive generators continuously.

In the current study, the blade has been strengthened by two shear webs in the middle of the sections as shown in Figure 4.4. The FEM model is illustrated in Figure 4.5.

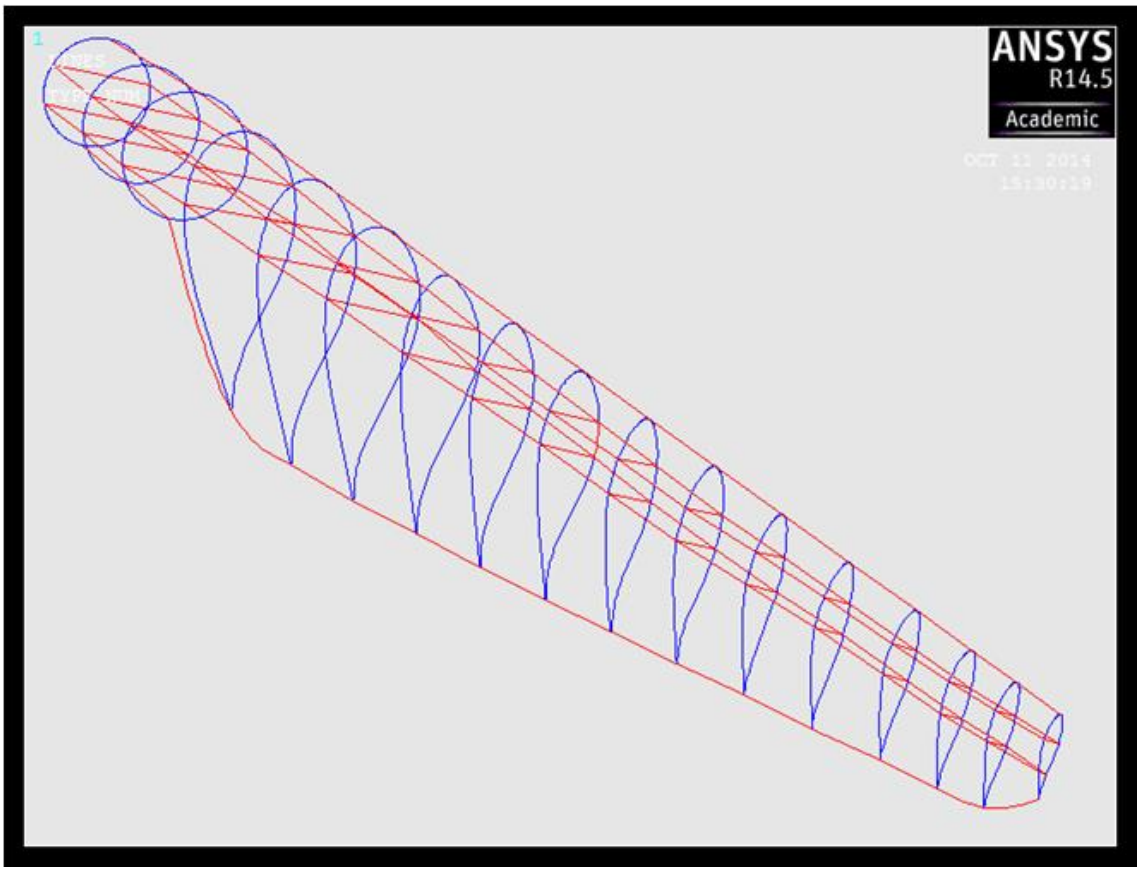

Figure 4.4: All sections of the modelled blade with two shear webs in the middle of the blade

For the wind turbine blades, the designers want a material that is light for a required stiffness. This is to satisfy the blade design criteria to overall blade

weight induced fatigue load which is mainly based on the fatigue damage calculations of the blade material for the main load carrying structure (Standard DNV, 2010). It is worthwhile to notice that decreasing the weight of the wind turbine blade will directly reduce the load on both tower and foundation.

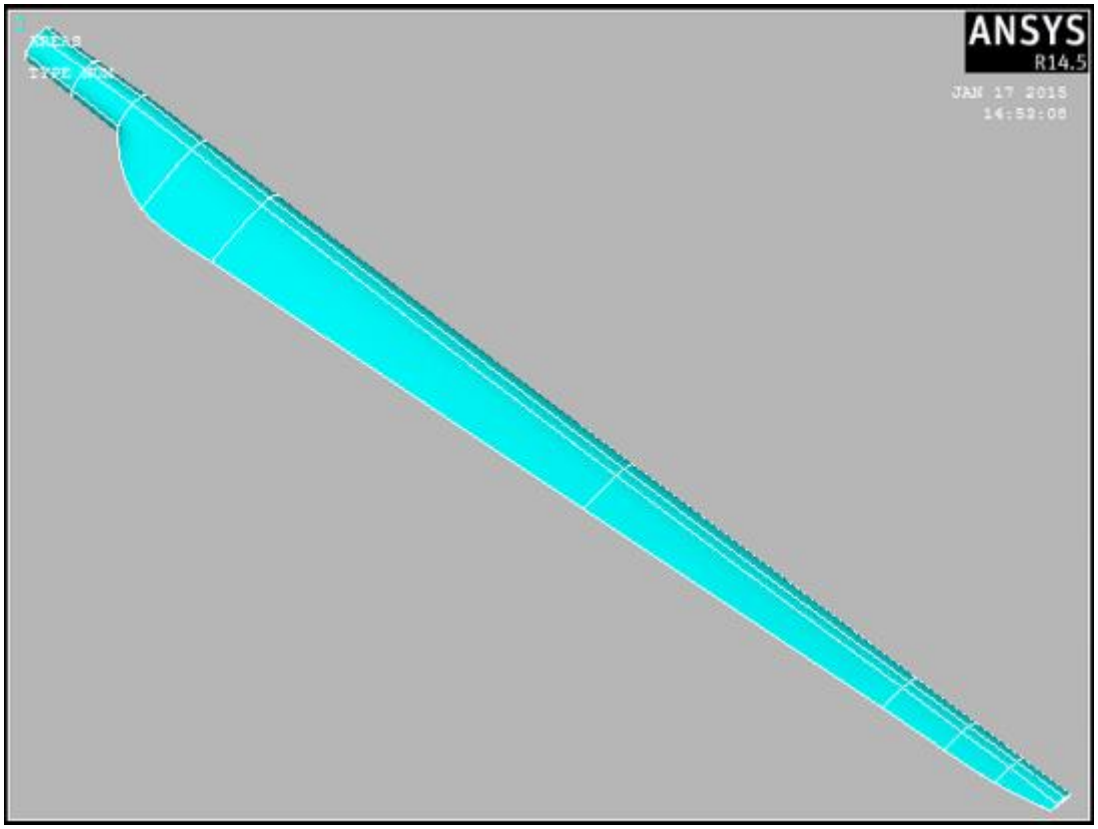

Figure 4.5: The 5-MW wind turbine blade FEM model

Modern wind turbine blade material is switching to carbon fiber-reinforced plastics with tensile modulus between 50GPa and 66GPa and compressive modulus between 43GPa and 60GPa (Hogg, 2010). The average elasticity modulus for glass fiber is 41.8 GPa (Loth et al., 2012). The modulus of elasticity for the proposed model is assumed to be 50 GPa as most of researchers assumed that carbon fiber composites has higher modulus of elasticity (Bortolotti, 2012, Brøndsted et al., 2005, Elger et al., 2014). The authors suggested ultralight pre-aligned rotor for a 10 MW wind turbine that can make an overall system cost

saving of 25% by using carbon fiber reinforced plastics. The advantages of using carbon fiber composites to replace glass fiber composites in wind turbine blades are their higher elastic modulus, higher tensile strength, lower density, and lower fatigue sensitivity, while the main disadvantage is the higher cost (Fuerle et al., 2010), but the increasing use of carbon fiber in wind turbine blade industry will reduce the price gap.

For blades with mixture of glass and carbon fiber, total mass decreases with an increasing share of carbon fiber. (Schueller et al., 1997a). Also carbon-glass fiber hybrid reinforcement can assure a remarkable solution by combining the outstanding processability of glass fiber with the high performance of the carbon fiber (Wilburn, 2011, Hillermeier, 2009). According to (Bortolotti, 2012), the carbon fiber returned the best wind turbine blade performance.

The modern wind turbine blades are usually produced by the use of multiaxial fabrics. The +/- 45º laminates are usually used in the blade skin (Mishnaevsky Jr and Favorsky, 2011). It should be noted that fibre-reinforced plastics (FRP) are considered as structural materials. For the strength load transition area, two materials of different stiffness are usually joined e.g. steel bushing/glass-carbon laminate (Standard DNV, 2010).

It is clear that the wind turbine designers currently tend to reduce the weight of the blade, basically to improve mechanical properties and decrease the load on the rotor and thus increase the overall efficiency. In this research, an ultralight carbon reinforced fiber based material for the blade is suggested, with +/- 45º laminates being used in the blade skin. The material is assumed isotropic. Data for skin thickness and material properties, i.e. modulus of elasticity and density,

were not included in the 5-MW NREL (Jonkman et al., 2009) wind turbine report except for the mass, which is 16,500 kg for the 5-MW Multibrid model and length of 61.5 m (Jonkman, 2006a).

The 5-MW wind turbine blade thickness was assumed by (Tarfaoui et al., 2011) to vary from 20.1 mm to 32.2 mm. (Loth et al., 2012) assumed an average blade thickness of 20 mm. For the current model, a variable blade skin thickness is assumed with 30 mm for the root and 20 mm at the tip. As mentioned above, the materials of the modern wind turbine blade are getting lighter and stiffer as there is gradual shifting towards carbon reinforced fiber (Schueller et al., 1997a) suggested a glass/carbon with equal share mixture blade with density of 1300 kg/m^3. The overall density of the modern wind turbine blade will decrease when considering other materials like the foam which used as laminated core having low density values range between 71-104 kg/m^3 (Schueller et al., 1997b). For this research, the suggested material is ultra-light carbon reinforced fiber with an overall density of 1000 kg/m^3. Material properties for the proposed blade are given in Table 4.2.

Table 4.2: Material properties for the proposed model

Property	Value
Young's modulus (GPa)	50
Poisson's ratio	0.3
Density (kg/m^3)	1000
Blade skin thickness (m)	0.02-0.03
Total mass (kg)	16,150
Total length (m)	61.6

As for properties of accreted ice, density was assumed 900 kg/m^3 for hard rime, for this density, ice has an elastic modulus of 7 GPa and Poisson's ratio of 0.36 (Voitkovskii, 1960). The simulated wind turbine blade is treated as a cantilever beam fixed with the hub at the root and free at the tip end. The CAD model of the blade was set up in Rhinoceros and then exported to ANSYS 14.5 for the structural analyses.

4.2.3 Single Blade Meshing and Vibrational Analysis

For meshing of the blade, quadrilateral element has been selected with free mesh scheme. Knowing the complexity of the blade shape, the using of a free mesh has no restrictions in terms of element shapes, and there is no specified pattern applied to it, while on the other hand, the use of the mapped mesh is restricted in terms of the pattern of the mesh and the element shape it contains, so mapped mesh is not very suitable for complex shapes like wind turbine blade. The meshed wind turbine blade is illustrated in Figure 4.6.

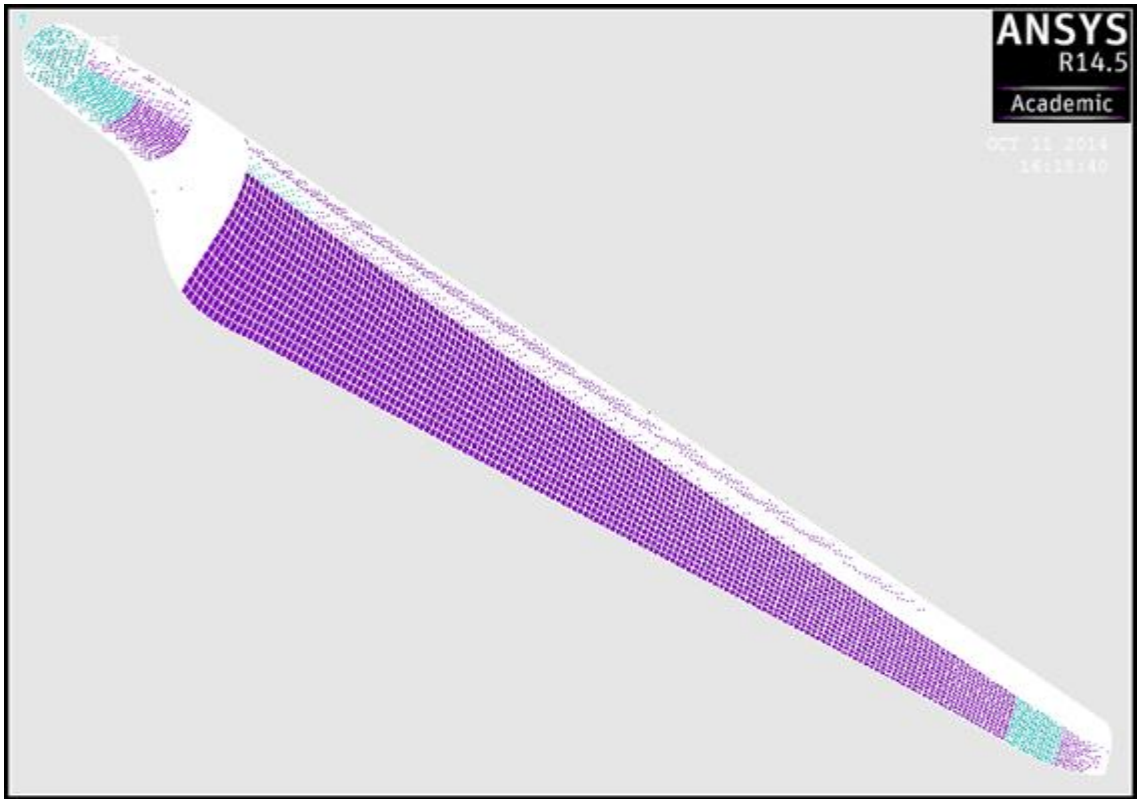

Figure 4.6: The meshed wind turbine blade ANSYS model

The quadrilateral element is very suitable to blade meshing. The blade has large and long rectangular areas in which quadrilateral element may fit easily, the meshing procedure mainly consists of three steps:

1- Select the mesh tool and choosing line set including all lines of the blade.
2- Select the mesh tool and choosing the longest lines.
3- Again select the mesh tool and choosing the lines of the necking area set higher number of divisions in order to refine meshing of this area which experience large stresses.

Difference between elements sizes of necking area and areas to the left and the right is clear as shown in Figure 4.7. The Figure illustrates how finer mesh is used during the meshing in areas where large stress gradients are expected like

necking area. The above procedure was repeated to get courser or finer mesh in order to investigate mesh sensitivity of the blade as explained in next section. The quadrilateral element is very suitable to blade meshing. The blade has large and long rectangular areas in which quadrilateral element fit easily.

The meshing was performed for the clean wind turbine blade and the ice mass has been added by editing the real constant set in ANSYS as added mass per unit area. More explanation of ice mass calculations is given in next Chapter.

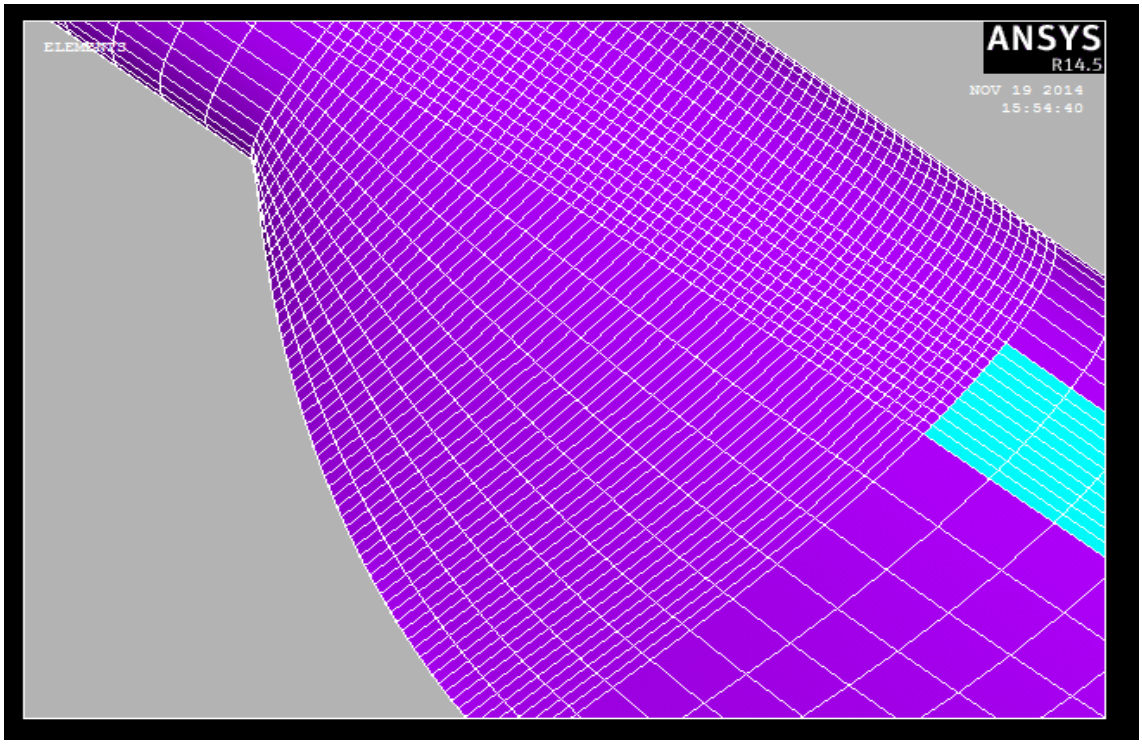

Figure 4.7: Detailed mesh view near necking area

4.2.3.1 Mesh Sensitivity Analysis

To validate a finite element (FE) model, the requirement on the convergence of the model must be satisfied. In this study, eleven sets of mesh schemes are used to determine the convergence of the first three modes where eleven different element sizes are applied to the same structure. It is important to mention that

the lowest three natural frequencies are the most important modes due to higher excitation energy whereas higher modes have little excitation energy (Hau, 2010a) .Eleven modal data sets are presented in Table 4.3. The difference in natural frequency between the same modes of these eleven sets can then be used to determine the convergence of the simulation results.

Table 4.3: First three natural frequencies obtained for eleven mesh schemes (Hz)

No. of Elements	7000	9120	11480	14080	16920	20000	23320	26880	30680	34720	39020
1st Mode	0.699	0.699	0.700	0.701	0.701	0.701	0.701	0.701	0.701	0.701	0.701
2nd Mode	1.028	1.030	1.031	1.031	1.032	1.032	1.033	1.033	1.033	1.033	1.033
3rd Mode	2.348	2.350	2.352	2.353	2.353	2.354	2.354	2.354	2.354	2.354	2.354

Table 4.4: Deviation percentage of natural frequencies from the last set

No. of Elements	7000	9120	11480	14080	16920	20000	23320	26880	30680	34720
1st Mode	0.38%	0.23%	0.15%	0.09%	0.07%	0.05%	0.03%	0.02%	0.01%	0.01%
2nd Mode	0.52%	0.36%	0.25%	0.18%	0.14%	0.10%	0.07%	0.05%	0.03%	0.02%
3rd Mode	0.29%	0.18%	0.12%	0.07%	0.05%	0.04%	0.03%	0.02%	0.01%	0.01%

During the process of meshing as the number of lines across the blade changed, the size of each element changed; consequently, the number of elements in each meshing set changed. Table 4.4 shows natural frequencies deviations from the last set in Table 4.3. Please note that Table 4.4 contains ten sets as it shows

deviation percentages of the first ten sets from the last set. The deviations for the first and the third modes are very similar as both modes represent first and second frequencies in the flapwise direction while larger deviations were noticed for the second mode which is the first bending frequency in the chordwise direction. It can be seen that for blade model the difference is less than 0.52% which gives confidence of the results and less simulation time and memory. As such, the mesh scheme of 7000 elements is used for the subsequent analysis. The percentage deviation of the values of natural frequencies from the last set is shown in Figure 4.8, it is clear from the Figure that as the number of elements gets bigger, less deviation is noticed in natural frequencies.

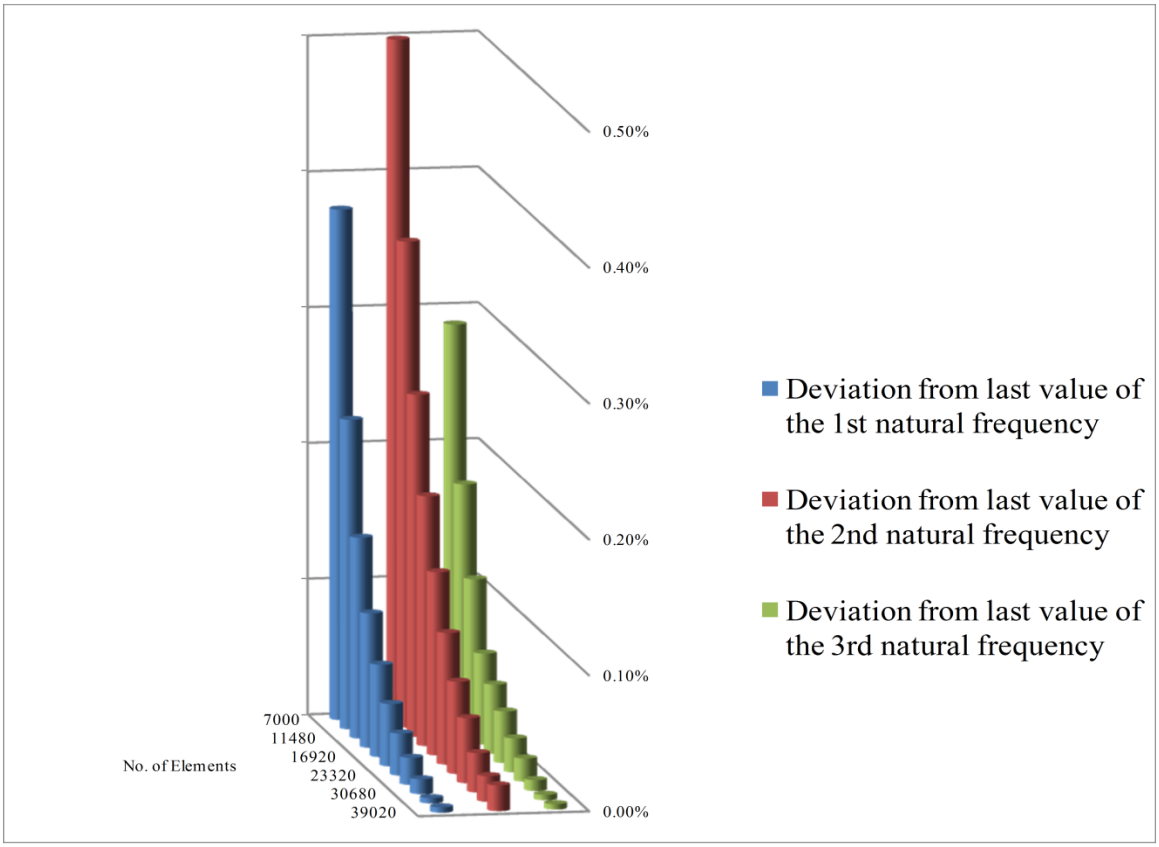

Figure 4.8: Deviation percentage of natural frequencies from the last set

4.3 Icing of Wind Turbine Blade

The ice load on wind turbine blade increases with ice density as the maximum ice density used for severe conditions. The ice assumed to be in hard rime to glaze form. Glaze has density of 800-900 kg/m^3 in harsh conditions with strong adhesion (Makkonen, 2000). Also (Myers and Charpin, 2004) stated in their work that for severe cases the ice density is taken as an average between typical glaze and rime values and suggested 898 kg/m^3. In this research, the accreted ice is assumed to have a density of 900 kg/m^3 and the temperatures are in the range of 0 ºC to -10 ºC as hard rime formed in this range of temperatures (ISO, 2001b).

4.4 A Novel Approach to Estimate the On-Blade Accreted Ice Mass and Thickness

The approach developed in this research is an approach to estimate the accreted icing load and thickness based on the geometry of the blade sections. Load increases with the increase of ice accretion thickness and its density. A linear increase is assumed as the ice accretion is considered to have linearly tapered shape (ISO, 2001a). It is assumed that the taper goes from the tip through 46 m of the blade length, which covers five zones for the region over the leading edge where most of ice accretion occurs, as mentioned earlier, due to tendency of ice to accumulate around stagnation points and taper shape structure of the blade ((Fu et al., 2006), (John, 2001) , (Seifert and Tammelin, 1996)) . This region is divided into five zones. The area and length of the five zones are given in Table 4.5.

Table 4.5: Iced zones dimensions

Zone Number	Length(m)	Area(m^2)
1	2.7	3
2	2.9	3.36
3	4	4.52
4	16	24.87
5	21	39.89
Total	46.6	75.64

Ten areas will cover the five zones. Each zone consists of two identical areas to the left and to the right of the leading edge. Figure 4.9 illustrates the targeted areas on the leading edge.

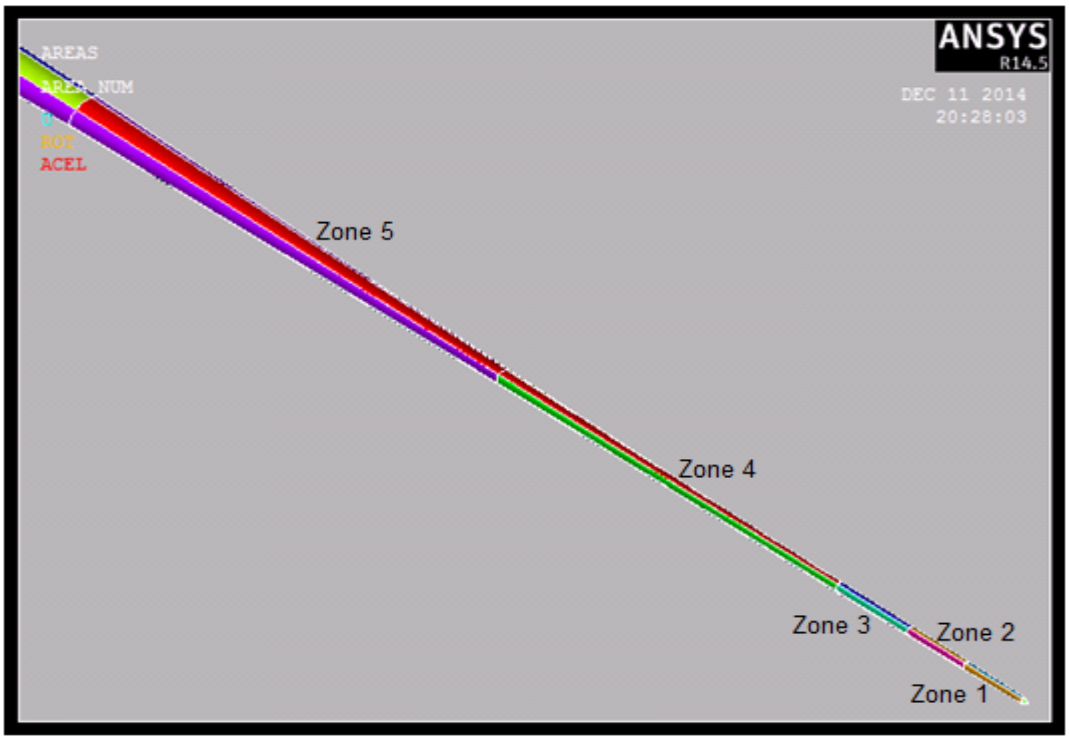

Figure 4.9: The five icing zones on the top of the leading edge of the wind turbine blade model

The approach consists of the following procedure:

1) Examine key points of the blade section profile for each selected zone

2) Measure the distance between each opposite key points as illustrated in Figure 4.10.
3) Choose the largest distance between opposite key points which represent the largest thickness of the blade.

To demonstrate the approach of estimating accreted ice thickness and mass calculation, section DU21 of the 5-MW blade was chosen, the section lies in zone 3 which is in the middle of the icing zones. Figure 4.10 illustrates section DU21 with four key points connecting two distances. The largest distance will represent the thickness of the section to be considered for the accreted ice thickness and mass calculation.

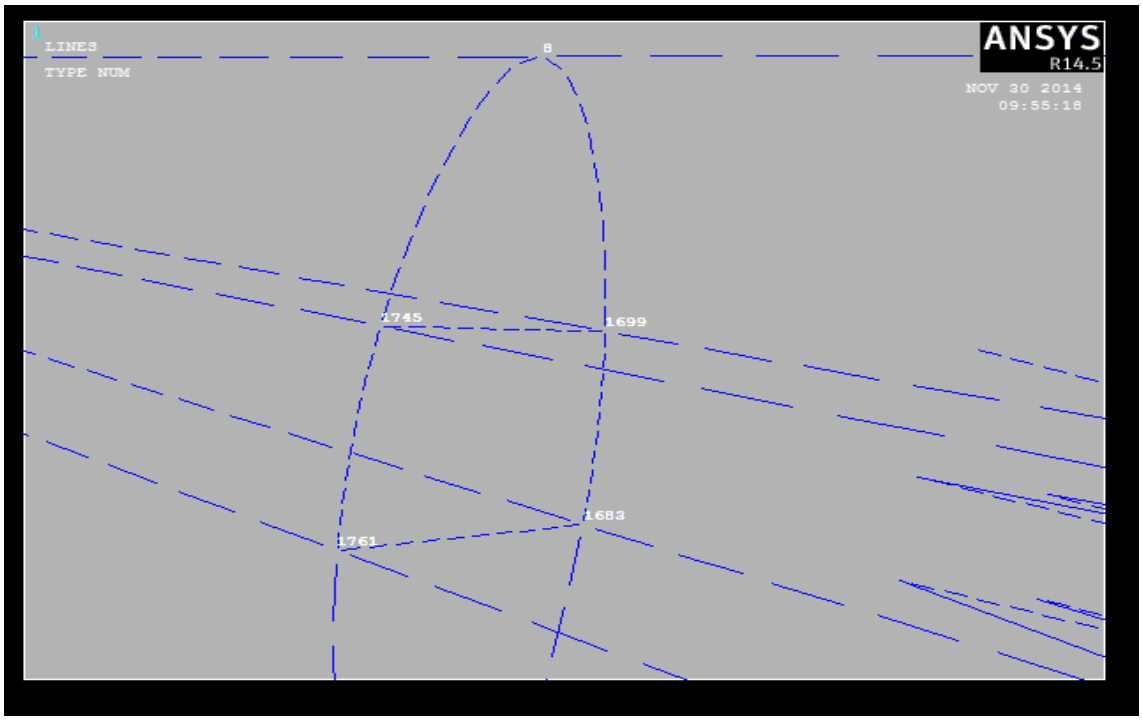

Figure 4.10: A detailed view of section (DU21) with largest width distance between key points 1761 and 1683.

It is clear from Figure 4.11 that the thickness of the wind turbine blade section is associated with the Z-axis of the coordinate system. The correspondent Z-axis coordinates of the illustrated four key points in Figure 4.10 are given in Table 4.6

Table 4.6: Key points coordinates in Z-axis for the section DU21

Key points	Corresponding coordinates in Z-axis (m)	Width of the line connecting key points (m)
1699 and 1745	0.4057 and -0.2609	0.67
1761 and 1683	0.4109 and -0.3176	0.73

It is important to notice that by using the simple and direct new approach, the thickness and the mass of the accreted ice on the wind turbine blade can be estimated, while similar tasks usually need special software as 'FENSAP-ICE' which was specially designed for ice shape, thickness and mass estimation (Shin and Berkowitz, 1994, Homola et al., 2012) or for example, the use of 'TURBICE' for ice accretion simulation and mass estimation (Laakso et al., 2010). Furthermore, the approach can be used for estimating heavily icing events which usually lasts for several weeks, this is simulate the real cases of harsh blizzards, while the available software deal with short-time simulations which does not reflect the real icing scenarios. The three assumed icing scenarios represent icing events in cold countries which varies from moderate to heavy icing in the severe weather conditions.

Table 4.6 shows that largest width is 0.73 m for the longest distance between these two key points which actually represents the largest thickness of wind turbine blade at that section. Knowing the largest width of the aerofoil section, the thickness of ice for each assumed icing scenario may be calculated.

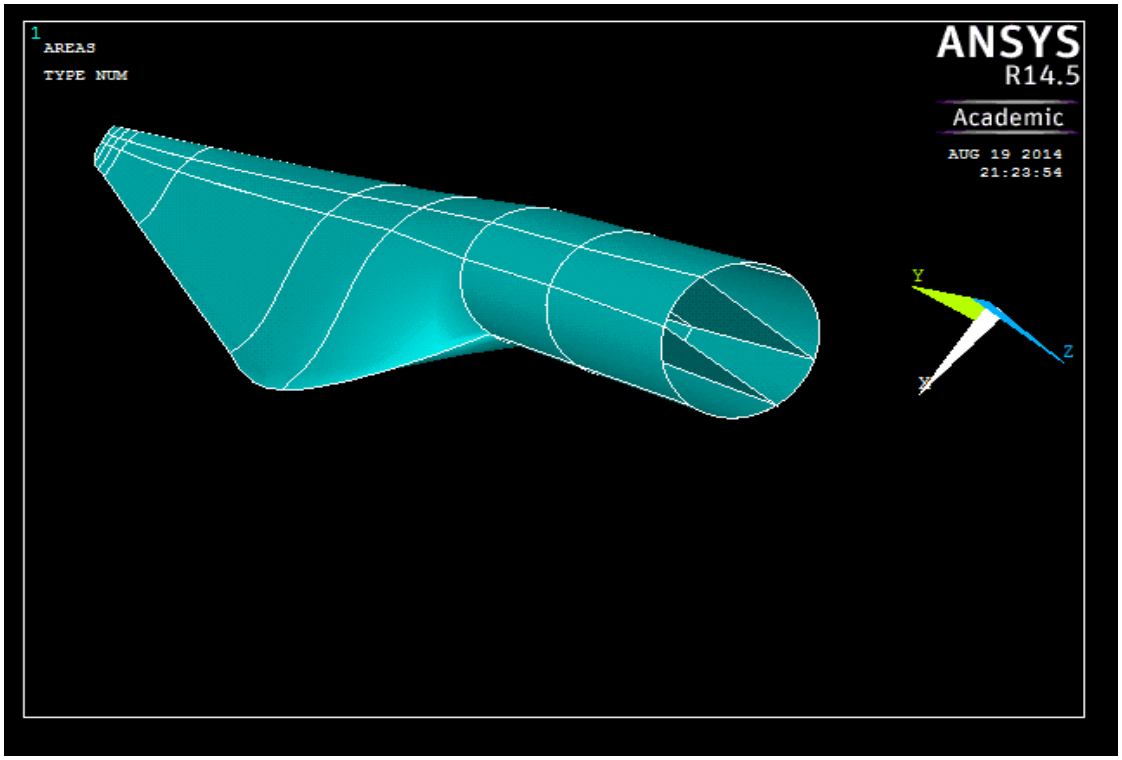

Figure 4.11: The width of blade sections associated with the Z-axis.

The icing load was estimated based on assumed icing scenario according to ISO 12494 Standards (ISO, 2001b). The areas for all zones were given in Table 4.7. For icing zone 3, it has been shown that largest section width is 730 mm, by using Table 4.8, considering R5 for moderate icing scenario and the value 730 mm lies between object width 500-1000 mm, ice mass estimation can be interpolated between 9.2-19.9 kg/m to be 14.1 kg/m as given in Table 4.7 which is for moderate icing scenario. Detailed results for heavy icing scenarios are given in Appendix A.

Table 4.7: Details for ice estimated mass and load with for moderate scenario

Icing Zone	Longest Distance Across Sections *W* (mm)	Length of Selected Zone (m)	Estimated Accreted Ice Mass (kg/m)	Estimated Accreted Ice Load (kg/Zone)
1	380	2.7	6.7	18.1
2	420	2.9	7.5	21.8
3	730	4	14.1	56.4
4	1480	16	30.6	489.6
5	1870	21	38.3	804.3

The largest width distance for other different sections of the wind turbine blade can be calculated using coordinates of the key points for each section as explained above. The ice thickness is assumed uniform through each individual zone as the ice thickness doesn't change dramatically along the blade length rather than gradually (Tammelin and Seifert, 2001, Homola et al., 2011).

The ISO 12494 has been set up for different situations of icing events. The reference is suitable for small objects, i.e. less than 300 mm in thickness or diameter for round objects according to (ISO, 2001b) and also for large objects. The 5-MW wind turbine blade is however a large object, in fact very large as compared to 300 mm. So by considering wind turbine blade sections which are larger than 300 mm, type A of Figure 4.12 will be used where *t* is the ice thickness, $\hat{W}$ is the largest width of the object, Ł is the length of the ice vanes which is the maximum accreted ice thickness at the leading edge, and *D* is the total rime accreted diameter. For the selected ice accretion model, three icing scenarios will

be discussed in the next Chapter. The different icing scenarios will be analysed in terms of the vibration behaviour due to icing and rotation motion.

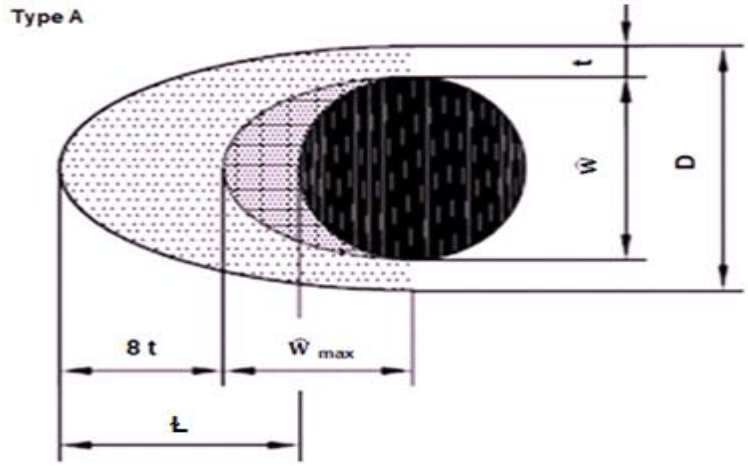

Figure 4.12: Typical ice accretion model (ISO, 2001b)

Table 4.8: Accreted ice dimensions and masses for large, round objects (ISO, 2001b)

Cross-sectional shape of ice objects: Large round objects						
Object width (mm)		300	500	1000	3000	5000
Icing condition IC	Preliminary Ice mass, m, (kg/m)	Accreted ice mass (kg/m)				
R1	0.5	0.5	0.9	2.0	6.2	10.5
R2	0.9	0.9	1.7	3.6	11.2	18.9
R3	1.6	1.6	3.0	6.4	19.9	33.5
R4	2.8	2.8	5.2	11.1	34.9	58.7
R5	5.0	5.0	9.2	19.9	62.3	105
R6	8.9	8.9	16.5	35.3	111	186
R7	16.0	16.0	29.6	63.5	199	335
R8	28.0	28.0	49.7	104	321	538
R9	50.0	50.0	84.4	171	515	859

Table 4.8 summarizes the ice mass based on the blade geometry for different icing scenarios started from R1 for very light icing through R5 which lies in the middle of the table as a moderate icing case, the severity of icing event is increased as going for R7 to R9. It is worthwhile to mention that second and third columns of Table 4.8 are identical as the preliminary ice mass is assumed for

blade thickness of 300 mm for all icing cases. The most severe case that could happened is the heavy icing scenario R9. So R8 and R9 cases have been chosen to represent the heaviest possible icing case that may occur in the cold regions.

Another way to explain the novel approach is to imagine a circle drawn in the wind turbine blade section, the diameter of the circle represents the largest width of the blade and this circle is the largest possible circle can be drawn inside the blade section as illustrated in Figure 4.13. This distance plays a key role in the developed approach for calculating both the estimated accreted ice mass and thickness.

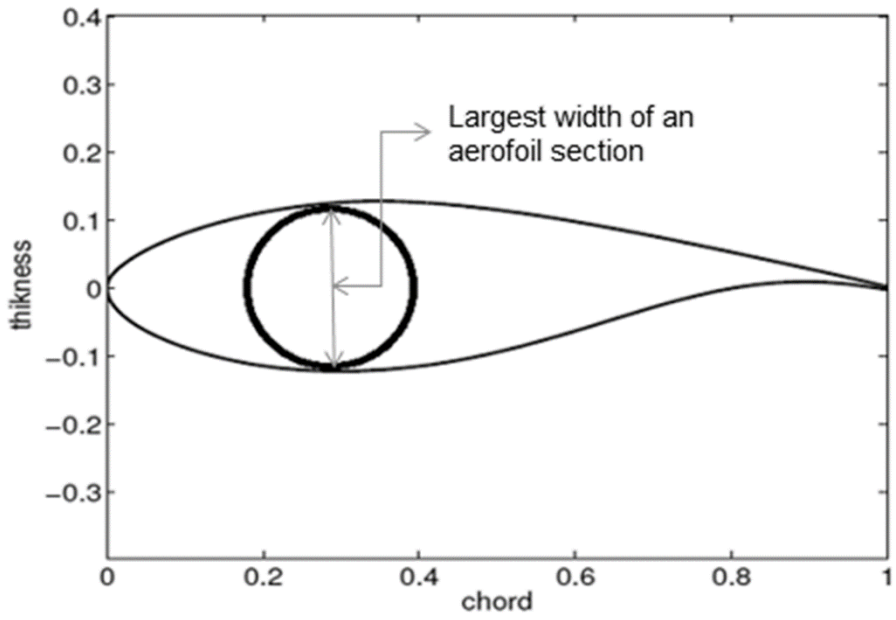

Figure 4.13: Typical 5-MW aerofoil section assuming a circular shape in the middle

It is important to notice that the mass of ice per given zone is increased gradually from zone 1 to zone 5 as the area of the leading edge on the top of wind turbine blade is increased. Also the assumed zones represent three quarters of the blade length because most of accreted ice lies on this area for typical operating rotor (Tammelin and Seifert, 2001). By referring to ISO (12494) International Standard (ISO, 2001a), mass of accreted ice on the wind turbine blade could reach

considerable amount of that of blade in severe weather conditions. In some harsh weather conditions mass of ice can be as heavy as the mass of the blade itself (Frohboese and Anders, 2007b).

4.5 Numerical Setup of Assembled Rotor

4.5.1 The Hub Rotor

Wind turbines usually consist of four main components: the rotor, transmission system, generator, and yaw and control systems. Each of the four components is designed to work together in order to efficiently convert the motion of the wind into electricity. The nacelle which is mounted on the tower, contains the transmission system, generator, yaw and control systems and the rotor is fixed on it. The nacelle rotates (or yaws) according to the wind direction. A typical nacelle with proper connection with the hub is illustrated in Figure 4.14.

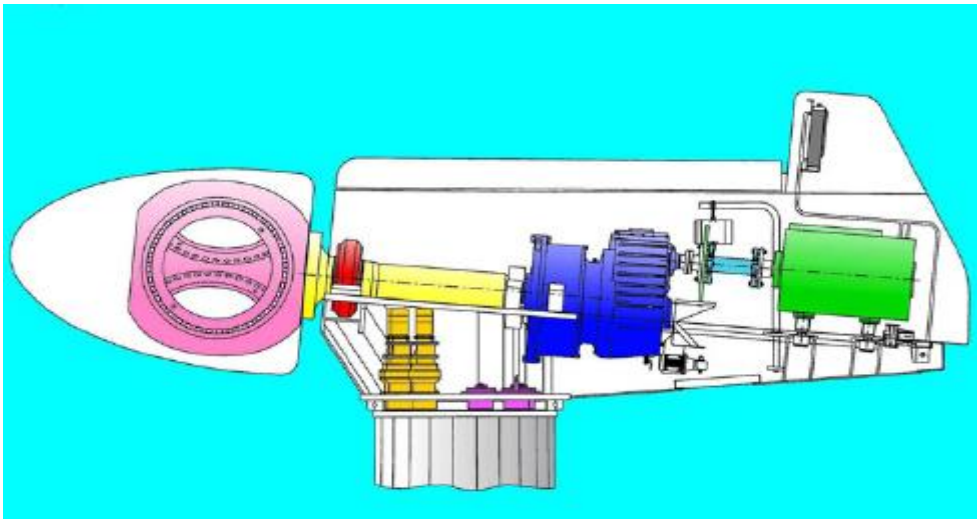

Figure 4.14: Typical nacelle with transmission system (Risø, 2002)

The blades are attached to the rotor shaft through the hub. The later is usually consists of nodular cast iron components for transferring the blade loads to the wind turbine support structure. The complexity of the hub is the major reason for

using cast iron, which makes it practically hard to produce in any other manufacturing method. In addition to that, the requirement of higher impact and fatigue resistance can be satisfied by the nodular cast iron due to its nodular graphite inclusions.(Song et al., 2003) experimentally investigated the effects of nodular graphite on the vibration fatigue resistance and confirmed above claims.

Three element types were used for the mesh of the turbine rotor. Quad4 is a four node linear quadrilateral element for the blades. Tri3 is three node linear triangle element and Tit10 is ten-node tetrahedron for the hub as it appears in Figure 4.15.

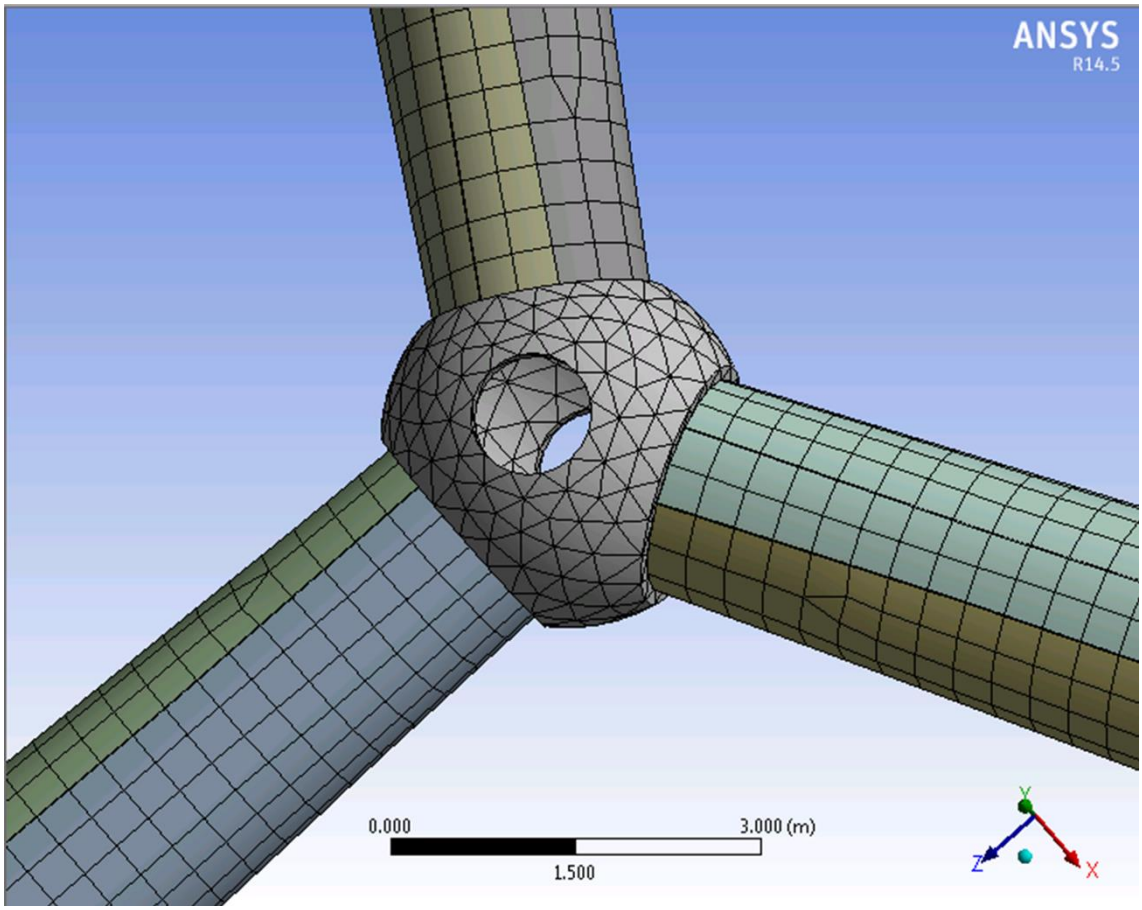

Figure 4.15: Detailed view for meshing of the assembled model

Mesh quality has been checked using mesh statistic metric analysis. Element quality had an average of 0.85 out of a unity. Aspect ratio was 1.27 in a minimum to maximum range of 1-126.5 and skewness average of 0.146 of a maximum value of unity. Figures 4.16- 4.18 show meshing quality results confirming the validity of the mesh.

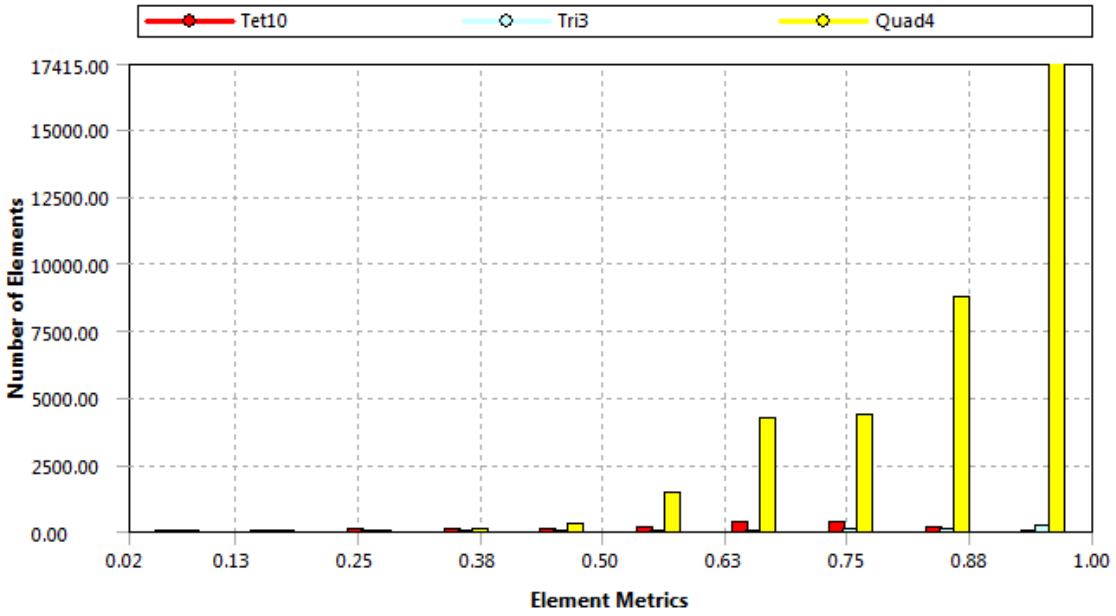

Figure 4.16: Mesh element quality with an average of 0.85

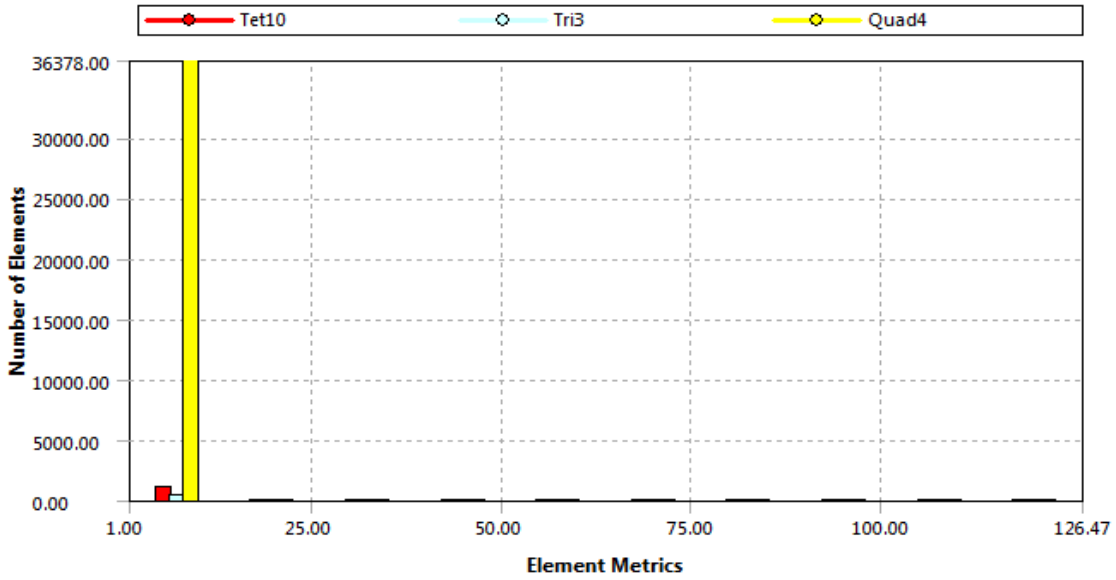

Figure 4.17: Mesh aspect ratio with an average of 1.27

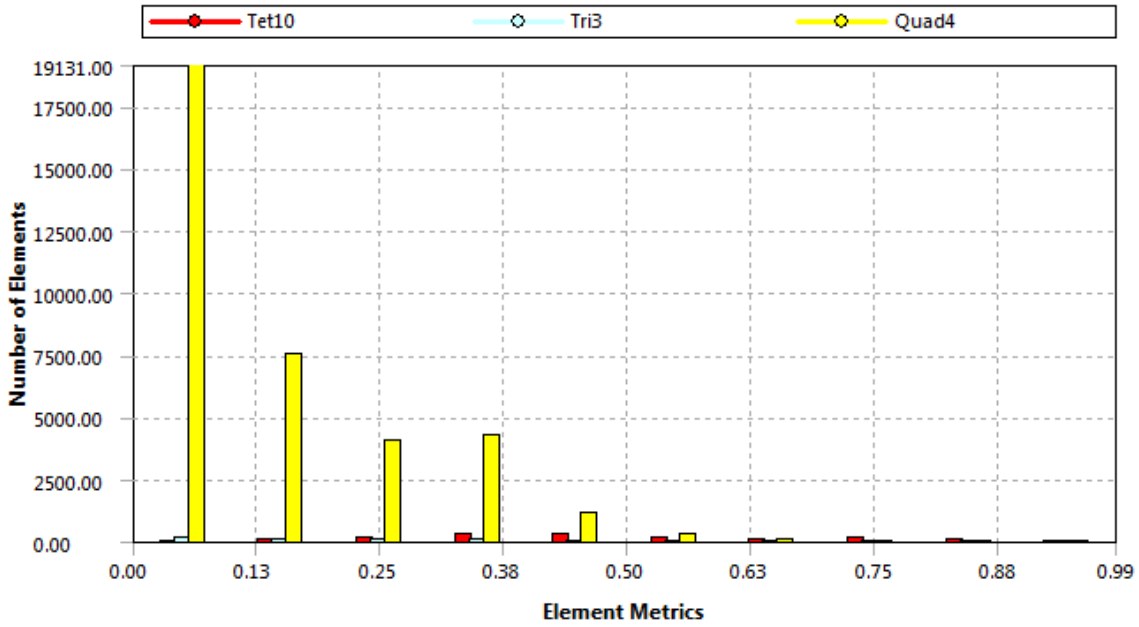

Figure 4.18: Mesh element skewness with an average of 0.15

To model the hub in ANSYS Parametric Design Language (APDL) environment, two spheres were made and be subtracted from each other to get a hollow sphere with the required thickness. The upper hole was created by using a suitable cylinder using 'divide volume by area'. After that, with the help of ANSYS WORKBENCH, a new coordinate system was defined by 3 key points in the rotating plane. A cylinder with same diameter of blade root was subtracted in the three planes separated by 120^0 each. The other two holes on the hub were for the shaft and the front nose cover of the hub. A typical hub for a large wind turbine and the modelled one are shown in Figure 4.19.

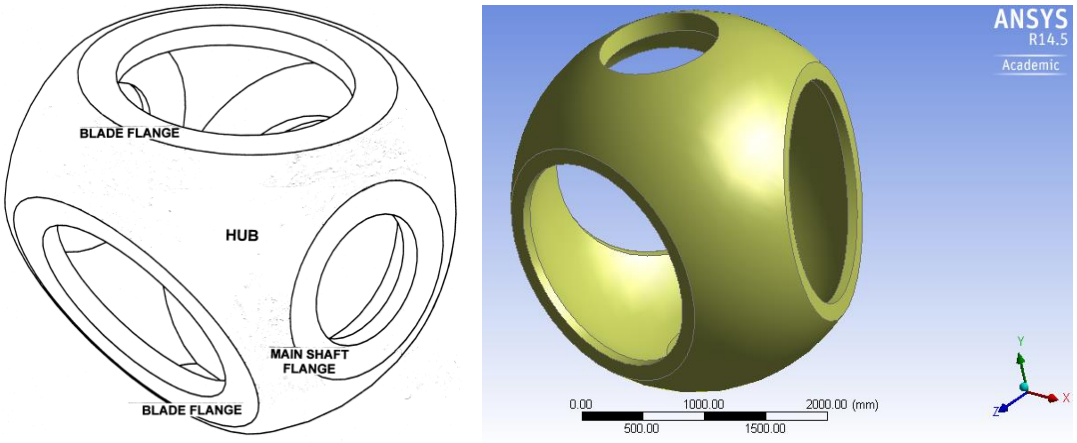

Figure 4.19: Typical hub for large wind turbines (Risø, 2002) left and the modelled hub to the right

The assembly has been completed in the ANSYS WORKBENCH environment as shown in Figure 4.20. Shell181 has been used for the blades while Solid187 was used for the hub. The new shell element has the advantage of being able to accommodate the hub. The blades are fixed on the hub and thus their modes of vibration are similar to the modes of a cantilever beam.

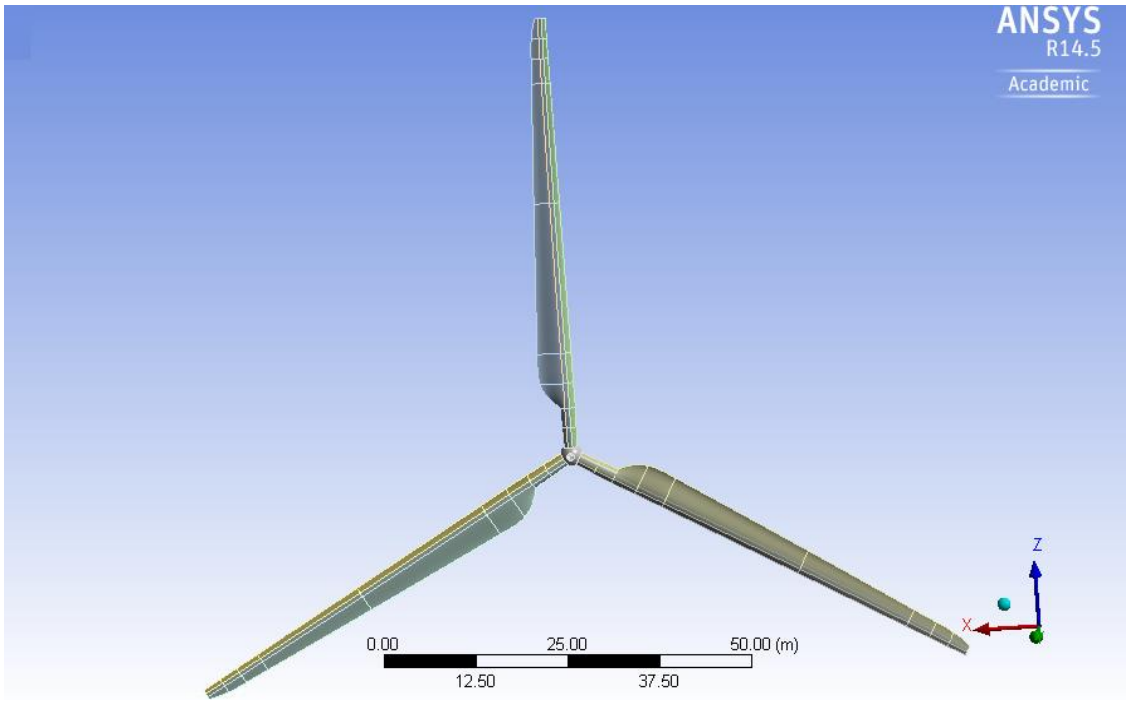

Figure 4.20: The assembled model using ANSYS WORKBENCH

4.6 Summary

The 3D-CAD model was built in Rhinoceros and exported to APDL ANSYS. Numerical setup was presented including meshing for single wind turbine blade. A novel approach to estimate the on-blade accreted ice mass and thickness calculations was explained. The approach relates the estimated ice thickness and mass directly to the geometry of the wind turbine blade section by considering the maximum width at any given section, this represents a shortcut for the estimation of accreted ice mass and thickness rather than using special software and by so saving time and money. The assembly of the three blades with a proper hub has also been established in ANSYS WORKBENCH. Both single blade and the assembled model will be used in next Chapter to extract natural frequencies for clean and iced cases.

CHAPTER FIVE

RESULTS AND DISCUSSION OF STRUCTURAL NUMERICAL ANALYSIS

5.1 Background

In this Chapter, results of structural numerical analysis will be discussed. Firstly, an overview of wind turbine blade icing phenomena is presented. Then a typical 5-MW wind turbine blade was modelled and natural frequencies were extracted. To investigate vibrational behaviour of wind turbine blade under different icing events, three assumed icing scenarios were investigated, which include a moderate icing case and two heavy icing cases according to ISO Standards (12494). The vibrational analysis for the assembled numerical model is performed for these three different scenarios.

5.2 Single Non-Rotating Blade Numerical Results

The NREL 5-MW wind turbine blade was numerically modelled. It is observed from Table 5.1 that the first two natural frequencies of the clean blade are very near to the values listed in the NREL 5-MW turbine specifications (Jonkman et al., 2009).

Table 5.1: Natural frequencies for the clean and the iced modelled blade

Mode No.	Natural frequency for clean blade (Hz)	NREL Specifications (Jonkman et al., 2009)	Relative Error As Compared to NREL	Natural frequency heavily iced blade R9 (Hz)
1	0.71	0.70	1.4%	0.5
2	1.04	1.07	2.8%	0.72
3	2.37	2.02	17.3%	1.64

Natural frequencies are reduced considerably by the increase of the mass of the blade due to accreted ice mass. On the other hand, natural frequencies remained in very good coherence during the mesh density analysis given in Chapter 4. It is

concluded that more accumulated ice will lower the natural frequencies to values closer to the first resonance frequency, which is associated with the first natural frequency of the tower of the wind turbine and so approaching to the self-excitation region. More focus in this research is given for the first natural frequency because of the possible exciting with the first natural frequency of the wind turbine tower. According to (Hau, 2010b), The rotor-tower system is continuously subjected to the risk of self-exciting.

The modes of blade in wind turbine are of the most important characteristics of free vibration of rotor system. For on-shore turbine, the lowest first natural bending frequency of the tower can reach 0.4Hz ((Larsen and Hanson, 2007a) ,(Dunne et al., 2012)). Although (Jonkman et al., 2009) stated in the specification of NREL 5-MW wind turbine that the tower frequency is about 0.32 Hz, but (Larsen and Hanson, 2007b) have emphasized in their paper that higher tower frequencies are associated with those off-shore turbines. This research mainly investigated the dynamic effects on wind turbines due severe icing events which basically located off-shore in cold weather countries, so by taking the first tower flexural natural frequency as 0.4 Hz, according to (Hau, 2010b), 25% of this frequency should be added as a safety distance for the excitation region leading to a safe tower natural frequency of 0.50 Hz.

5.3 Non Rotating Rotor Assembly Numerical Results Due To Atmospheric Icing

Dynamical behaviour of assembled wind turbine blades with the hub due to ice accretion is investigated and compared with the result of a single blade. Literature

review for the general rotary machinery was given with emphasis on dynamic effects on wind turbines in Chapter 2.

The three blades of a NREL 5-MW wind turbine have been assembled with the hub as shown in Chapter 4. The model is then simulated by using finite element software ANSYS to find the fundamental natural frequencies of the assembly. An investigation is carried out to check how natural frequencies are changed due to different ice loading. The ice loading has been adopted based on ISO 12494 International Standard (ISO, 2001b).

5.3.1 Calculations for ice load using ISO 12494

In subsequent sections, the vibrational effects due to the three icing scenarios, namely moderate icing case R5, heavy icing R8 and heavy icing R9, will be discussed. These three scenarios represent the mostly practical cases in the cold regions ranging from moderate cases to heavy cases. R5 case represents a mild icing scenario which lies in the middle of icing scenarios (ISO, 2001b). As mentioned earlier, the on-blade accreted ice can reach 135 kg/m for one week simulation (Frohboese and Anders, 2007a). During real icing events, blizzards may stays for three weeks (Walsh, 2010), so in order to simulate real icing cases two other scenarios are chosen for the heavy icing events with R8 representing a heavily icing event and R9 representing a severe case.

The leading edge of the wind turbine blade section is considered as a large round object as illustrated in Figure 4.14. It is obvious that the real cross sectional shape of wind turbine blade is not perfect round, but according to (Wadham-Gagnon et al., 2013), wind turbine blade may be assumed that it is round near the leading

edge. The authors suggested to use type (A) in Figure 4.14 to represent ice accretion on NREL 5-MW blade. It is also stated in the International Standard (ISO, 2001b) that its tables and figures may be used for the wind turbine blade. Table 4.8 was used to calculate the ice mass load according to the ISO Standard reference. It is important to note that all the assumed cases were referred to Table 4.8.

5.3.2 Case 1: Moderate Icing Scenario

According to the method explained in Section 4.4 and Table 4.8 the preliminary mass for moderate icing case is equal to 5 kg/m. ρ_{ice} is the density of the ice which is considered as hard rime with the density of 900 kg/m^3 (Makkonen, 2000). Figure 5.1 represents the accreted ice mass per length and blade width $\hat{W}$ of different zones for the moderate scenario. It is clear that mass of accreted ice is increased as the width of the section increases

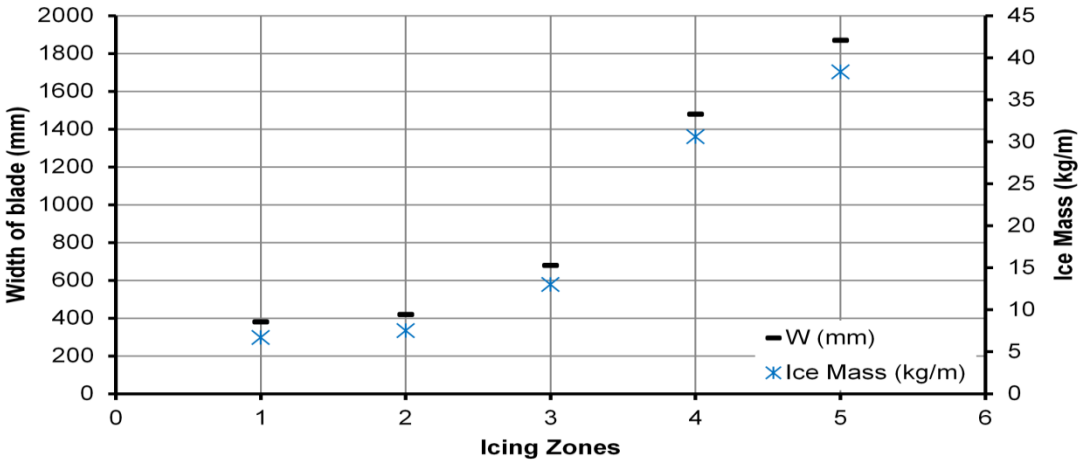

Figure 5.1: The accreted ice mass per length and per zone and blade width for moderate scenario

5.3.3 Sample Calculation

By referring to the method presented in Section 4.4 for the first zone, the longest distance across the blade section, $\hat{W}$, is 380 mm. By referring to Table 4.6 for the moderate R5 icing case, the width $\hat{W}$ lies between 300 mm and 500 mm associated to ice mass between 5 kg/m and 9.2 kg/m. By interpolation, the accreted ice mass is 6.7 kg/m. The length of the selected zone is 2.7 m which is taken from Table 4.7. So the estimated accreted ice mass for the first zone under the moderate icing scenario will be 6.7×2.7=18.1 kg.

Total accreted ice mass for moderate icing scenario is about 9% of the blade mass. It is clear from Figure 5.2 that ice mass is increased from tip of the blade towards the root because of the increased area of the leading edge.

5.3.4 Case 2: Heavy Icing Scenario R8

The severe weather hits the northern areas and high Arctic and must be taken into account. R8 case is an example of an assumed heavy icing case according to Table 4.8 in the standard (ISO, 2001b). For R8 case, the same value of ice density as in moderate icing case is considered. The preliminary value for ice mass is 28 kg/m. It is important to notice that the preliminary ice mass value is valid for all zones when dealing with the same icing case. Summary of calculated ice mass per length and ice mass per zone as related to the maximum width of each zone for R8 case is given in Table A1 in Appendix A. A big increase in the accreted ice mass is noted in this heavy icing scenario.

5.3.5 Case 3: Heavy Icing Scenario R9

According to the ISO Standard given in Table 4.8, the preliminary value for ice mass for R9 is 50 kg/m. The same calculation was carried out for icing case R9. Results of the detailed summary calculations for R9 case are given in Table A2 in Appendix A.

To get more details of all cases, the accreted ice mass per unit length for the three assumed scenarios is illustrated in Figure 5.2. The accreted ice per zone is shown in Figure 5.3. It is clear that tremendous amount of ice is accumulated in both R8 and R9 cases compared with that in moderate icing case.

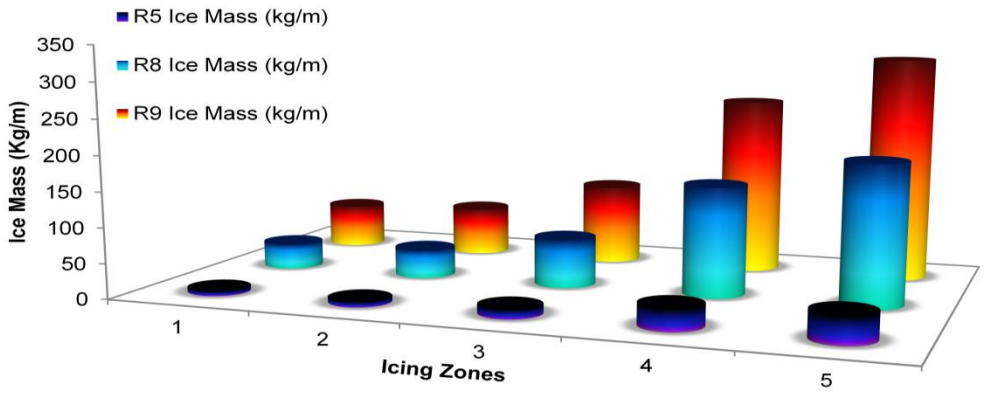

Figure 5.2: The accreted ice mass per unit length for the three assumed scenarios

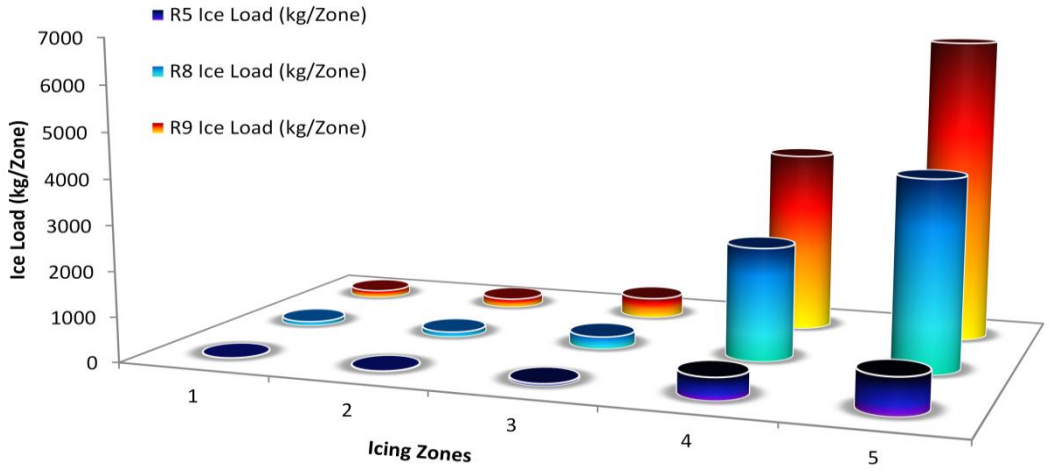

Figure 5.3: Accreted ice mass for different zones for all icing cases

It is clear from Figure 5.3 that ice mass is increased as severity of icing event increases with the minimum ice mass values observed for moderate case. The mass is increased as moving from tip to root of the blade, which is obvious due to the fact that area is increased towards the root of the blade. The Figure also shows the huge increase of ice mass for the two heavy assumed cases. Heavy icing case R9 has the highest accreted ice mass.

The thickness of the accreted ice is bigger at the tip area of the blade and smaller as moving towards the root of the blade as the thickness of the accreted ice inversely related to the chord each section of the blade (Homola et al., 2009) which is minimum near the tip and maximum near the root. It is interesting to note that, despite thickness of ice is more at tip area; the mass is increased towards the root of the blade as the area of leading edge is smaller near the tip and larger near the root of the blade.

5.4 Effects of Heavy Icing on Vibrational Behaviour of Wind Turbine

The total accreted mass for icing case R8 is 7159 kg per blade and 11633 kg per blade for icing case R9. Knowing that the structural mass of the blade is 16265 kg means that the mass of icing for Case R8 and Case R9 represents 44% and 70% of the mass of the blade, respectively. The vibrational effects due to both icing scenarios are analysed using ANSYS 14.5. This analysis has been performed for rotating and non- rotating cases. It is clear from the Table 5.2 which is for all icing scenarios, that all natural frequencies values are increased for rotating conditions as compared to those under non-rotating conditions.

For Figure 5.4, abbreviations are used as:
bl: blade

CA-NR: Clean assembly non-rotating

ML-NR: Moderate loading non- rotating

ML-R: Moderate loading-rotating

HLR8-R: Heavy loading, R8 case, rotating

HLR9-R: Heavy loading, R9 case, rotating

HLR8-NR: Heavy loading, R8 case, non-rotating

HLR9-NR: Heavy loading, R9 case, non-rotating

Table 5.2: Vibrational results for assembled model for all icing scenarios

Mode No.	Natural Frequencies for clean single blade (Hz)	Natural Frequencies for clean Rotating assembly (Hz)	Natural Frequencies for clean assembly Non-Rotating (Hz)	Natural Frequencies for the iced assembly (Hz)					
				Moderate Loading		Heavy Loading (R8)		Heavy Loading (R9)	
				Non-Rotating	Rotating 12 RPM	Non-Rotating	Rotating 12 RPM	Non-Rotatin	Rotating 12 RPM
1	0.71	0.73	0.66	0.63	0.66	0.55	0.58	0.5	0.53
2	1.04	1.07	0.95	0.91	0.92	0.77	0.81	0.72	0.74
3	2.37	2.47	2.18	2.1	2.18	1.77	1.92	1.64	1.76

Figure 5.4 shows a bigger gap between the clean rotor natural frequencies and the iced rotor during heavy icing cases. As severity of the icing event increases according to scenario R8 and scenario R9, the gap is increasing and approaching the unfavourable vicinity of the wind turbine tower frequency.

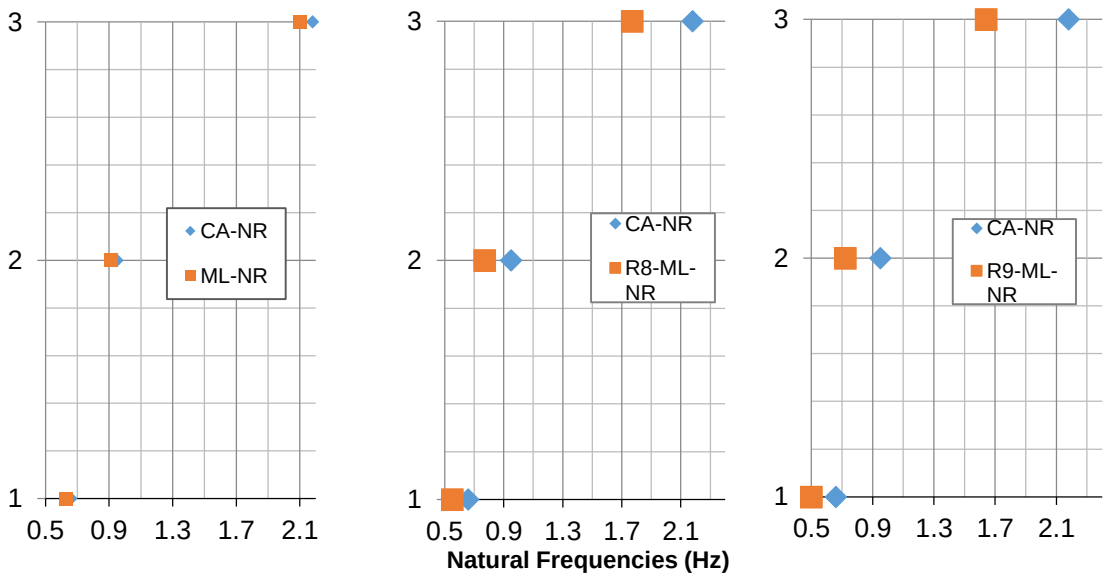

Figure 5.4: Reduction in natural frequencies due to icing for the three assumed scenarios, heavy icing R9 (right), heavy icing R8 (middle) and moderate case (left)

The first three mode shapes for the clean and iced blade according to the three assumed scenarios are illustrated in Figures 5.5-5.7

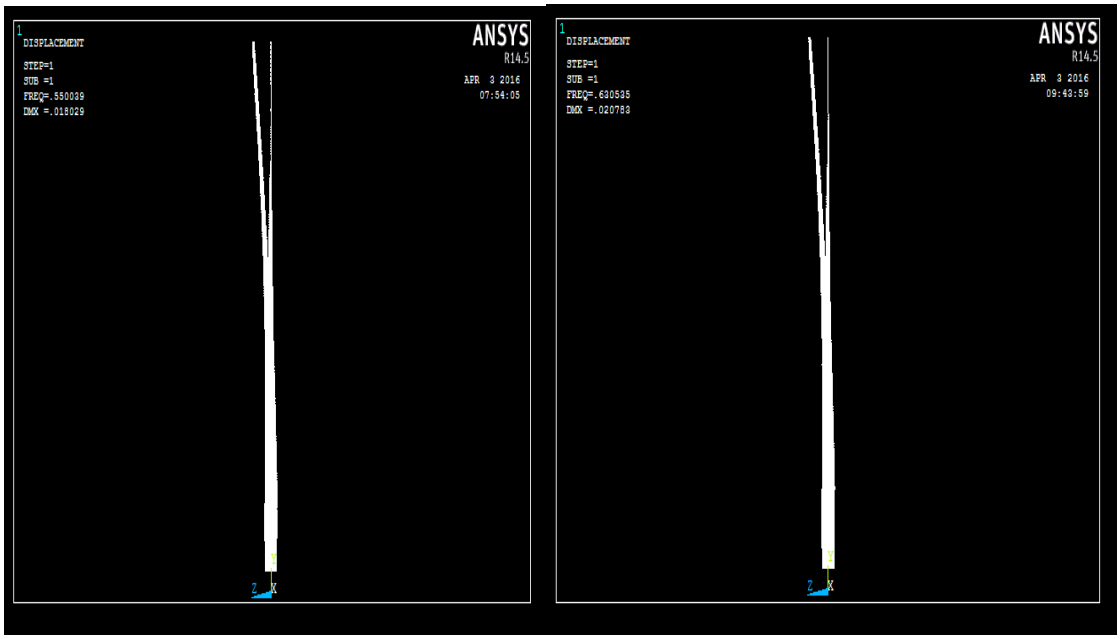

(a) (b)

(c) (d)

Figure 5.5: The first mode shape of vibration, (a) clean blade, (b) moderate icing, (c) heavy icing R8 and (d) heavy icing R9

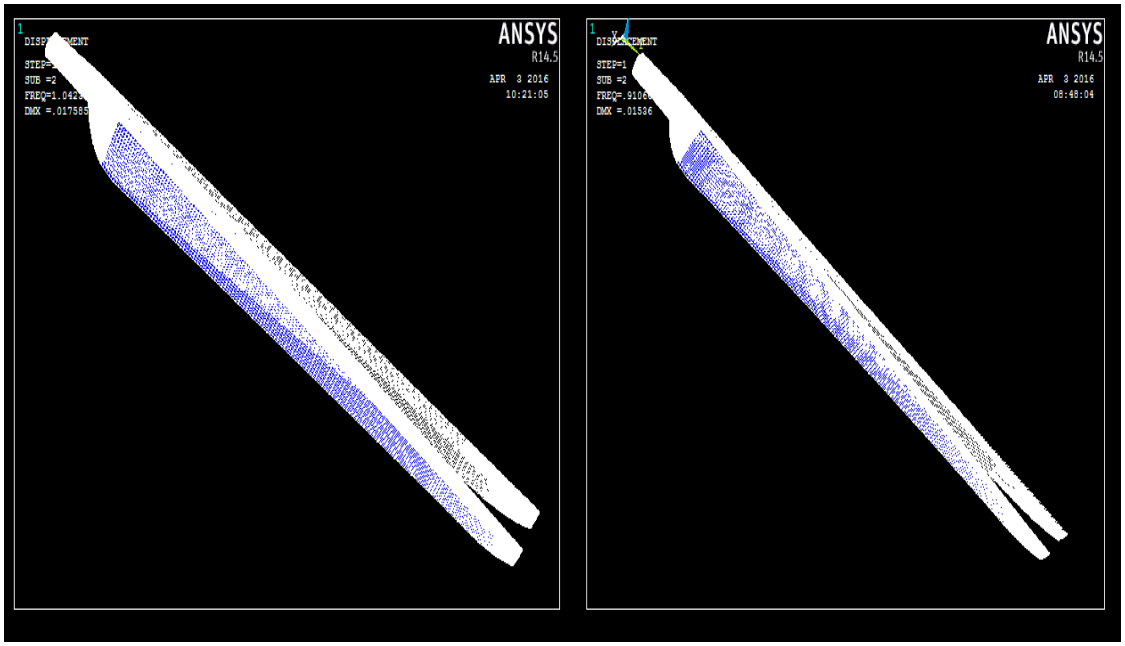

(a) (b)

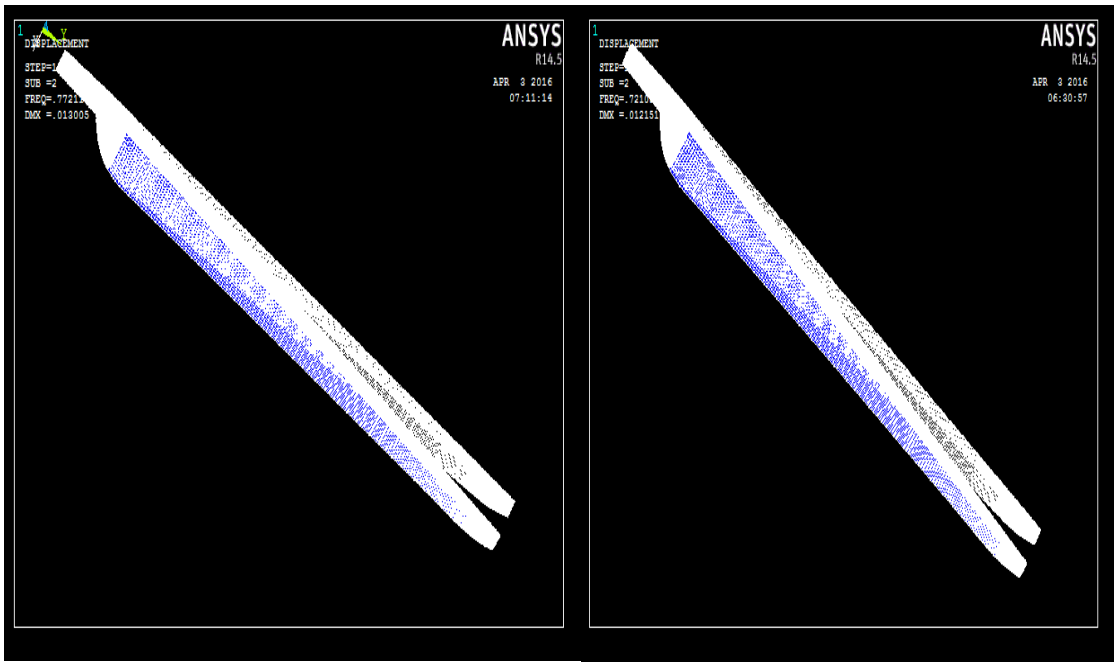

(c) (d)

Figure 5.6: The second mode shape of vibration, (a) clean blade, (b) moderate icing, (c) heavy icing R8 and (d) heavy icing R9

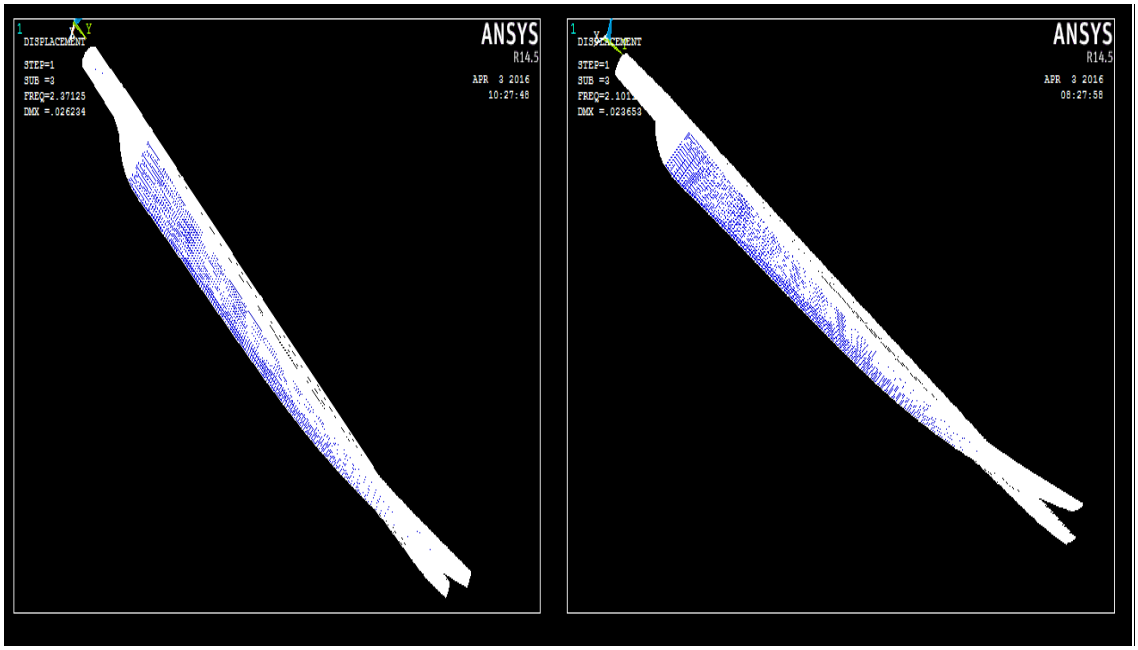

(a) (b)

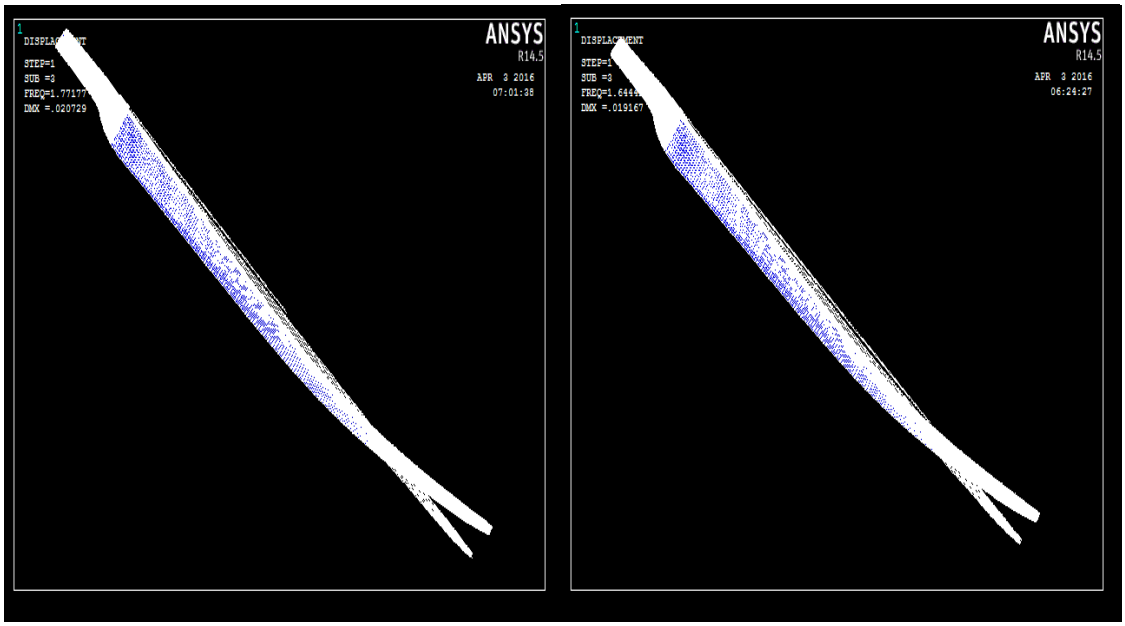

(c) (d)

Figure 5.7: The Third mode shape of vibration, (a) clean blade, (b) moderate icing, (c) heavy icing R8 and (d) heavy icing R9

As illustrated in Figures 5.5-5.7, the mode shapes for clean blade and assumed icing scenarios are given.

The results show that a small reduction in the natural frequencies has happened due to the assembly. The assembled model has experienced a reduction of 6%-8% for the first three mode of vibration as compared to the single non rotating blade because of the excess weight that has occurred as a result of the assembly. This is consistent to the work of (Hu et al., 2012) in which the assembly of the NREL 5-MW wind turbine blades experienced a reduction in the first three modes of natural frequencies of about 5%.

For the icing effect, comparison will be firstly made between non-rotating iced blades and clean assembly. A reduction of the first mode by 5% and 4% for second and third modes has been noted for moderate loading case. For the icing scenario R8, the first mode has experienced a reduction of 17% and 19% for the second and third mode. As for the severe icing scenario R9, the first and second modes of vibration have reduced by 24% and the third mode by 25%.

Second comparison will be made between rotating blades and clean assembly to investigate the rotating effects due to atmospheric icing on the blades. For moderate icing scenario, natural frequencies have experienced small reduction. No change was noted for the first and the third mode, while second mode has reduced by 3%. This could be explained by the fact that the small reduction in natural frequencies for the moderate icing scenario has been compensated by the increase in the natural frequencies which has happened due to rotational stiffening. For R8 icing scenario, the first and third modes have been reduced by 12%, and 15% reduction for the second mode. As for the severe icing scenario R9, the first mode has been reduced by 20%, 22% for the second mode and 19% for the third mode. Big reduction was observed for heavy icing scenarios as

compared to moderate icing scenario. A summary for results of estimated accreted ice were presented in Tables A1-A3 of Appendix A.

The numerical analysis of the assembled model shows the effect of the ice loading on the dynamic behaviour of wind turbine blades. Considerable reduction in the natural frequencies was noticed for the iced assembled model as compared to the clean one. Investigations also made it clear that vibrations became more and more serious when the exciting frequency approaches the natural frequency of the wind turbine tower, resulting in a high likelihood of resonant amplification and consequently structural instability.

5.5 Effects of Rotation on Vibrational Behaviour of Wind Turbine

The natural frequencies have increased for the rotating clean assembly as compared to the non-rotating assembly. The first mode of vibration has increased by 11% while the second and third modes have increased by 13%. These results are consistent with the literature results on the effect of rotation of beam structures without considering ice accretion. (Kim and Kim, 2011) addressed the issue of rotating 5-MW wind turbine and found that first and second natural frequencies had been increased due to rotation (13 rpm) by 9% and 12%, respectively. (Lee et al., 2012) concluded in his study about the performance of NREL 5-MW that an increase in the first natural frequency of 12% has happened because of the rotation. According to the results of (Park et al., 2010) for 2-MW or 3-MW wind turbines, frequency variations due to rotation are between 8% and 17%. (Khulief, 1989) investigated the vibration frequencies of a rotating tapered beams and concluded that as the speed of rotation increases, the first and the second modes experience an increase for all taper ratios.

It is worth noting that the present results in this work were for both clean and iced wind turbine blades, while the literature results mentioned above were for clean blades.

As for the three assumed icing cases, natural frequencies have been increased for the moderate scenario by 5% for the first mode, 1% for the second mode and 4% for the third mode. For scenario R8, both the natural frequencies of the first and the third modes have been increased by 5% and the second mode by 3%. As for the heavy icing scenario R9, natural frequencies of the first three modes have been increased by 6%, 3% and 5%, respectively. By comparing non-rotating iced blade with the rotating iced assembly under the same heavy loading scenario, it was clear that all natural frequencies have been increased due to rotation. It's important to notice that the increase in the frequency is almost similar for the first and third mode of vibration. This is basically because the two modes are for the first and second flapping modes respectively, while the second mode is the first edgewise mode. It is clear from above results that hub rotation has a stiffening effect in terms of the natural frequencies. The proposed numerical model result is consistent with several documented literature results and has a close relationship to the issue of rotating wind turbines.

One of the important reasons to the increase in natural frequencies for all modes during rotation is the centrifugal stiffening. The centrifugal forces lead to a higher bending stiffness of the blade as compared to the case of a non-rotating one. The rotation of the assembled blades produces a centrifugal stiffening effect that is referred to the centrifugal stiffening (Berzeri and Shabana, 1999). The change in stiffness of the blade from the centrifugal forces is mainly due to the induced

normal force which for motions in the rotor plane of the wind turbine is partially counteracted by the centrifugal forces, as they are always directed away from the centre of rotation towards the tip of the blade (Madsen et al., 1984). This effect is more dominant for the higher rate of rotation. For the current study, the increase in natural frequencies due to centrifugal stiffening is limited due to low rotational velocity which is rated as 12 rpm (Jonkman et al., 2009).

5.6 Discussion of the Numerical Results

As a result of the numerical analysis, it was found that the wind turbine under R9 case will not stand the vibrational sequences because of the low value of its first natural frequency and the fact that 0.5 Hz is the resonant frequency at which the blades will experience substantial amplitude enlargement leading to destructive consequences. The R8 scenario is not in a much better position considering 0.55 Hz as the lowest frequency, which is away from the resonant vibration by 0.05 Hz, a small amount of gaping for such a large wind turbine. This frequency is prone to be lowered to 0.5 Hz due to the aerodynamic fluctuation forces exerted on the blades resulting from variable wind velocity or by the expected uneven ice loading on different blades. Consequently, considering current trends in the design of wind turbines, operation should be halted under conditions of both heavy icing scenarios. When icing conditions are less severe, as in R6 and R7 icing conditions, the wind turbine is capable of withstanding those conditions for a short period of time before the icing accreting on the blades reaches a critical amount that can lead to lowering the natural frequency of the wind turbine near to the resonance frequency. In such cases, prompt steps should be taken to remove the accreted ice. Moreover, it is strongly recommended to prevent

tremendous amounts of ice accumulation on the wind turbine by adopting efficient de-icing methods in spite of the high cost of such heating systems in some countries and their power consumption which can reach up to 25% of the net output energy of the wind turbine.

5.7 Summary

In this Chapter, the numerical results for a single blade and the rotor were discussed for rotating and non-rotating conditions. Atmospheric icing of wind turbines and its effects on the vibration behaviour was investigated. The three icing scenarios (moderate, R8, and R9) according to ISO standard were introduced and applied to the rotor. Natural frequencies and mode shapes were extracted for all assumed icing cases and clean blade, which showed various extent of reduction in natural frequencies of all icing cases. The effect of rotation on vibrational behaviour was investigated. Lastly, the effects of uneven ice loading on wind turbine blades were discussed.

CHAPTER SIX

EFFECTS OF ICING ON STRUCTURAL INTEGRITY

6.1 Background

Material properties are affected by low temperature for structural components of wind turbine like blades, nacelle and tower. Blades play a key role in energy production as through their rotation and interaction with the incoming airflow power is produced. The severe weather conditions occurring in the cold climate and high altitude countries affect wind turbine industry in different ways including the problem of adding more stress to the wind turbine causing issues of structural integrity.

Fatigue is the progressive deterioration of mechanical properties of a material under fluctuating stresses and is particularly important in components subjected to repeated and often rapid load fluctuations such as wind turbine blades, aircraft components, vehicle suspensions, rotors, etc. (Homola et al., 2011).

In this Chapter, the effect of atmospheric ice accretion on the fatigue life of wind turbine blades under the three icing scenarios will be investigated.

6.2 S-N Study and Estimated Life of Wind Turbine Blade

The S-N curve presents the relation between the stress amplitude and number of cycles to failure. The fatigue life of the wind turbine blades must be carefully considered by the designers. According to the Germanischer-Lloyd (GL) regulations and the design requirements of the IEC 61400-1 international specification (IEC, 1999, GL, 2000, Lloyd, 1999), the fatigue life for wind turbine blade should be about 20 years which means life up to 10^7-10^8 cycles.

The three major fatigue life methods used in design and analysis are the strain-life method, the linear-elastic fracture mechanics method and the stress-life

method, (Budynas and Nisbett, 2006). The three methods try to predict the life of a structure in number of cycles to failure, N, for a component under a given fatigue loading spectrum. Generally, life of $1 \leq N \leq 10^3$ cycles is classified as low-cycle fatigue, whereas a fatigue life greater than 10^3 cycles is considered to have a high-cycle fatigue life. So wind turbine blade is classified as high-cycle fatigue component. (Mishnaevsky Jr and Favorsky, 2011) focused their research on the main requirements to wind turbine blades and highlighted the importance of high fatigue resistance and reliability to ensure the stable long term functioning.

As mentioned in Chapter 4, the wind turbine blades are usually produced with +/- 45º multiaxial fabrics laminates used in the blade skin (Mishnaevsky Jr and Favorsky, 2011). According to Guidelines for Design of Wind Turbines (Risø, 2002), ultimate strength of wind turbine blade structural materials should be considered for both tension and compression design. The average longitudinal fracture strength for carbon fiber reinforced plastic with +/- 45º layup orientation is 1243 MPa (Fuerle et al., 2010). While for the same material, (Brøndsted et al., 2005) presented in their paper a value of 470 MPa for composite with 30% volume fraction of fibers arranged in random orientation.

Stress analysis is a major step to investigate the effect of different icing loads on the fatigue life of the wind turbine blade. One good way is to consider an equivalent and effective stress represent the state of stress. This effective stress is usually called von Mises stress named after Dr. R. von Mises in his research about the distortion energy theory which predicts the yielding when the distortion strain energy per unit volume reaches or exceeds, for the same material, the critical value in tension or compression test (Budynas and Nisbett, 2006).

6.3 Wind Turbine Blade Life Estimated under Different Icing Scenarios and Wind Velocities

The structure of the wind turbine must be insured for both cases of static and dynamic loads. The static load originally initiated from the weight of the blade including the accreted ice while the dynamic load including the fluctuating of the incoming wind velocities on the blades (Perkins and Cromack, 1978), in this section, the lift forces will be calculated for a rotating blade with 12 rpm for two wind velocities of 10 m/s and 20 m/s and also for both clean and iced blade cases.

The aerodynamic pressure is changing throughout the blade mainly due to the geometry of the blade and the relative wind velocity. The lift coefficients will be calculated for all sections of the blade given in Table 4.1 and for angle of attack of 15 º as maximum lift force can be captured at this angle (Homola et al., 2012).

The lift force equation may be derived by considering the flow of gas over an aerofoil so the difference in the gas mechanical energy is simply equal to the work of the gas:

$$\Delta E_{mech} = ₩ \tag{6.1}$$

where ΔE_{mech} is the change in mechanical energy and $₩$ is the work which can be given as the sum of the kinetic energy and potential energy

$$₩ = \Delta T + \Delta V \tag{6.2}$$

where ΔT and ΔV are the change in the kinetic and potential energy respectively. Between any two arbitrary points, 1 and 2, both kinetic and potential energy can be given as

$$\Delta T = \frac{1}{2} m\, u_2^2 - \frac{1}{2} m\, u_1^2 = \frac{1}{2} m\, (\, u_2^2 - u_1^2\,) \tag{6.3}$$

$$\Delta V = m\, g h_2 - m\, g h_1 = m\, g(h_2 - h_1) \tag{6.4}$$

where m is the mass and h_1 and h_2 are the elevations of the two arbitrary points 1 and 2 respectively from a reference, but mass is density multiply by volume, so

$$\Delta T = \frac{1}{2} \rho \times \tilde{\mathrm{V}}\, (\, u_2^2 - u_1^2\,) \tag{6.5}$$

$$\Delta V = \rho \times \tilde{\mathrm{V}}\, \times g(h_2 - h_1) \tag{6.6}$$

where $\tilde{\mathrm{V}}$ is the volume. It is important to notice that the work is an activity involving both forces and movement for distance Δ_x in the direction of the force, so

$$₩ = F_1 \Delta_x - F_2 \Delta_x \tag{6.7}$$

The force can be expressed as pressure by the area

$$₩ = P_1 \times A \times \Delta_x - P_2 \times A \times \Delta_x \tag{6.8}$$

where P_1 and P_2 is the pressure at points 1 and 2 respectively and A is the area, but the area times the length is the volume, so

$$₩ = P_1 \times \tilde{\mathrm{V}} - P_2 \times \tilde{\mathrm{V}} = (P_1 - P_2) \times \tilde{\mathrm{V}} \tag{6.9}$$

By substituting in equation (6.2) we get

$$₩ = \frac{1}{2} m\,(\,u_2^2 - u_1^2\,) + \,\rho \times \tilde{\mathrm{V}}\, \times g(h_2 - h_1)\, = (P_1 - P_2) \times \tilde{\mathrm{V}} \qquad (6.10)$$

One can notice that the potential energy depends on the difference in height between the top and the bottom of the aerofoil which is minimal (McCormick et al., 1995), equation (6.10) can be reduced to the following:

$$\frac{1}{2} m\,(\,u_2^2 - u_1^2\,) = (P_1 - P_2) \times \tilde{\mathrm{V}} = \frac{1}{2}\rho \times \tilde{\mathrm{V}}\,(\,u_2^2 - u_1^2\,) \qquad (6.11)$$

Dividing by $\tilde{\mathrm{V}}$ yields

$$(P_1 - P_2) = \frac{1}{2}\rho\,(\,u_2^2 - u_1^2\,) \qquad (6.12)$$

Change in pressure is the force over the area, so

$$(P_1 - P_2) = \Delta F/A = \frac{1}{2}\rho\;(\,u_2^2 - u_1^2\,) \qquad (6.13)$$

And so

$$\Delta F = \frac{1}{2}\rho\, A\,(\,u_2^2 - u_1^2\,) \qquad (6.14)$$

The averaged force is the lift force, by multiplying equation (6.14) by a dimensionless constant which is the lift coefficient, one may get the lift force as:

$$\mathrm{L}_f = \frac{1}{2}\rho\, C_L\, A\,(\,u_2^2 - u_1^2\,) \qquad (6.15)$$

According to (Fay, 2001, Hau, 2010a), ($u_2^2 - u_1^2$) represents the relative air velocity passing over the wing which is perpendicular to the lift force and parallel to the drag force, so the lift force given in equation (6.15) can be written as:

$$\mathrm{L}_f = \frac{1}{2} C_L \rho c \mathrm{W}^2 \tag{6.16}$$

where W is the air relative velocity, for the drag force equation, one may start from kinetic energy of the air in front of an aerofoil as:

$$T = \frac{1}{2} m u^2 \tag{6.17}$$

Substitute $\rho \times \tilde{\mathrm{V}}$ for the mass yields

$$T = \frac{1}{2} \rho \times \tilde{\mathrm{V}} \times u^2 = \frac{1}{2} \rho A \times \Delta_x \times u^2 \tag{6.18}$$

Since kinetic energy represents the work here, so the force is

$$F = \frac{T}{\Delta_x} = \frac{1}{2} \rho A \times u^2 \tag{6.19}$$

The dynamic pressure is force by area and given by:

$$P_{dynamic} = \frac{1}{2} \rho u^2 \tag{6.20}$$

So dividing by the area for both sides of equation (6.20), the aerofoil profile drag force may be expressed as:

$$\mathrm{D}_f = \frac{1}{2} \rho A u^2 \tag{6.21}$$

Usually the drag force is given per unit length as:

$$\mathrm{D}_f = \frac{1}{2} C_D \rho c \mathrm{W}^2 \quad (6.22)$$

where C_D is the drag coefficient and c is the chord of an aerofoil. From equations (6.16) and (6.22), the lift and drag coefficients C_L and C_D may be written as:

$$C_L = \frac{L_f}{\frac{1}{2}\rho \mathrm{W}^2 c} \quad (6.23)$$

$$C_D = \frac{D_f}{\frac{1}{2}\rho \mathrm{W}^2 c} \quad (6.24)$$

Relative wind velocity at each section may be calculated using following formula (Manwell et al., 2009):

$$\mathrm{W} = \sqrt{\left(\hat{\mathrm{U}}_o(1-a)\right)^2 + \left(\hat{\mathrm{U}}_o \lambda_r\right)^2} \quad (6.25)$$

where $\hat{\mathrm{U}}_o$ is the incoming air velocity, a is the axial induction factor and λ_r is the local speed ratio and can be calculated as,

$$\lambda_r = \frac{\lambda \bar{r}}{r} \quad (6.26)$$

where $\bar{r}$ is the local radius of the blade section, r is the rotor radius and λ is the speed ratio. For large wind turbines, a value of 0.5 usually used for a (Homola et al., 2012).

It is important to notice that in order to get the lift force acing on certain area, the chord distance should be multiplied by the span covering that area (Houghton

and Carpenter, 2003), so the lift force associated with each segment will be multiplied by the span of the segment. All segments of the blade are illustrated in Figure 6.1.

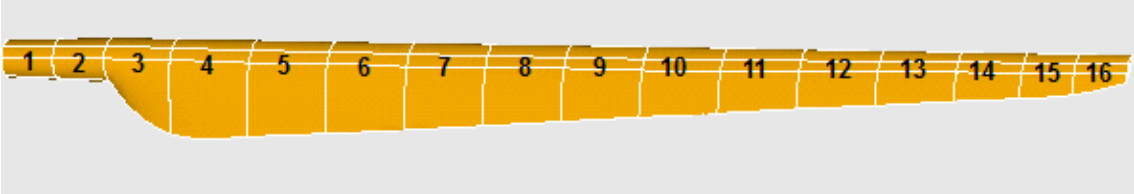

Figure 6.1: The successive segments of the wind turbine blade

The spacing between all sections and chords of the blade were given in Table 4.1, so the lift force acting on certain are is given by:

$$\mathrm{L}_{fa} = \frac{1}{2}\, C_L\, \rho\, c\, s_p\, \mathrm{W}^{\mathbf{2}} \tag{6.27}$$

where s_p is the span for each segment which represent the spacing between the blade different sections.

The total lifting force will be estimated by adding up the lift forces for sixteen successive segments as shown in Figure 6.1. The chords and spacing for all segments were given in Table 4.1 covering the whole outer surface area of the blade. This will be done for two velocities, 10 m/s and 20 m/s and for both clean and heavily iced blade case R8. The lift coefficients were calculated by using STAR CCM+ with the air density for the clean and iced blade cases having values of 1.21 kg/m^3 at 20 ºC and 1.26 kg/m^3 at -10 ºC respectively (McCormick et al., 1995).

As an example of the calculations, the results for the lift coefficients and forces for segment number 11 which include aerofoil section DU21 for both clean and iced cases and for wind velocities of 10m/s and 20m/s are given in Table 6.1.

Table 6.1: Lift forces for segment number 11

State of blade	Incoming wind velocity	relative air velocity	lift coefficient	Area $c \times s_p$ m^2	Lift force kN
Clean	10m/s	52.9	1.88		42.41
Clean	20m/s	53.7	3.28		76.25
Iced R8	10m/s	52.9	1.73	13.37	40.64
Iced R8	20m/s	53.7	3.06		77.16

The effect on the blade segments due to air lift force are fed on the FEM model of the blade in APDL environment of ANSYS through an added pressure. This will increase the load on the blade as the aerodynamical effect is taken into account for two different assumed incoming air velocities and heavy icing regime R8. The difference between relative velocity for 10 m/s and 20 m/s is small because in equation (6.25) the air velocity is multiplied by the speed ratio which is tip speed divided by the air velocity. It's worthwhile to mention that the lift force for the iced blade affected by wind velocity of 20 m/s has higher value than that for the clean one because the increase in the cold air density is higher than the reduction in the lift coefficient, but this increase in the lifting force for the iced blade is not an advantage because, at the end, the huge added ice mass increases the stress on the blade.

To estimate fatigue life for the wind turbine blade made of +/- 45° fiber composite materials, tensile fatigue life curves (S-N) are adopted by referring to a report prepared by the Oak Ridge National Laboratory (ORNL) which is managed and operated by Lockheed Martin Energy Research Corporation (USA) (Corum et al., 2000). The authors stated that stiffness varied linearly and the stress-strain response is essentially linear up to failure. The report has also investigated the temperature influence on the tensile strength for carbon reinforced polymer which shows an increase of 29% for sub-zero temperatures when compared to room temperature. Figure 6.2 illustrates effect of temperature on fatigue strength for reinforce carbon polymer of 0/90 and +/- 45° fibers orientation and Figure 6.3 presents some results under sub-zero temperatures.

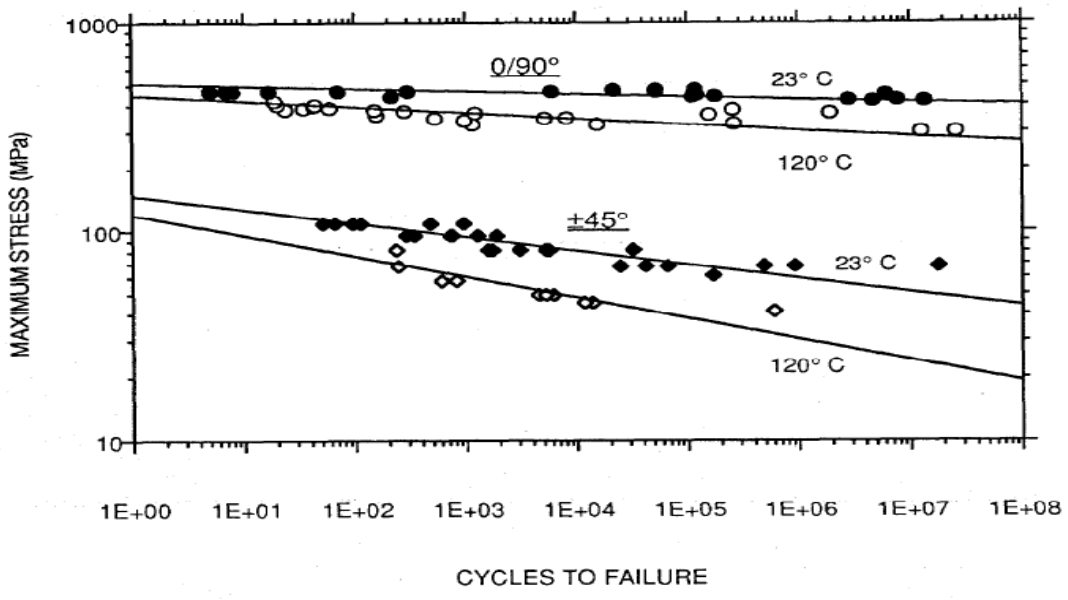

Figure 6.2: Fatigue curves for +-45° and 0/90° reinforced carbon fiber orientation (Corum et al., 2000)

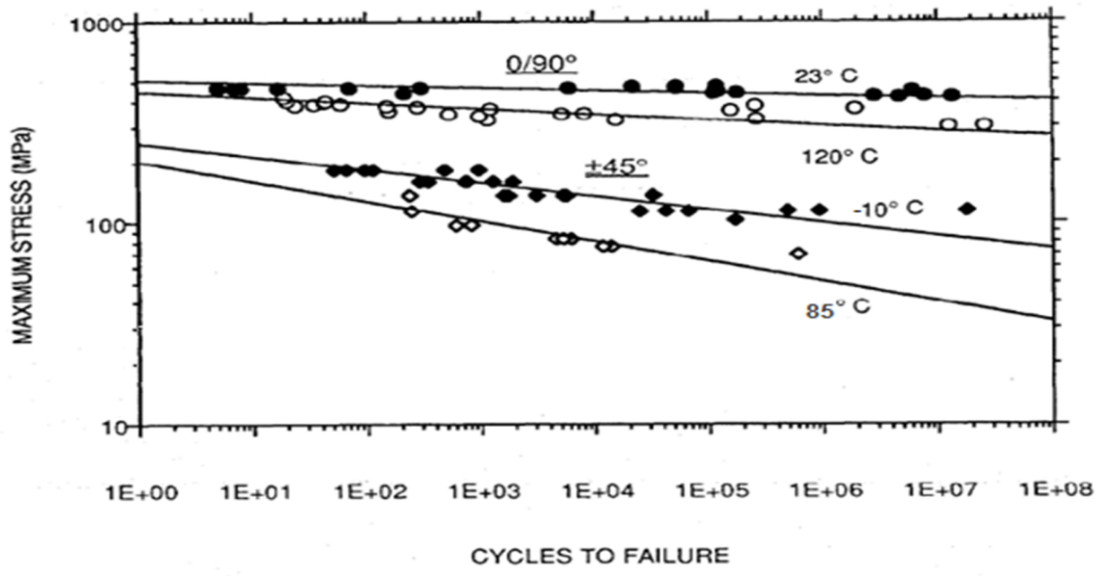

Figure 6.3: Fatigue curves for +-45° and 0/90° reinforced carbon fiber orientation for sub-zero temperatures (Corum et al., 2000).

By referring to Figure 6.3, the fatigue life of the wind turbine blade under two different air velocities 10 m/s and 20 m/s and for clean and heavily iced blade, R8 scenario case have been estimated using the cyclic von Mises stresses in Table 6.2 the blade experienced during the cycle of rotation.

Table 6.2: Estimated fatigue life for clean and iced modelled wind turbine blade

Blade condition	**Wind Velocity m/s**	**Maximum cyclic stress σ_{vm} (MPa)**	**Estimated fatigue life for blade (Cycle to failure)**
Clean	10	93.8	1×10^{7}
	20	104.0	2×10^{6}
Heavy icing R8	10	149.0	5×10^{4}
	20	173.0	$<1\times10^{4}$

Stresses have been increased significantly by adding the aerodynamic effect of the incoming air with different velocities to the effect of accreted ice due to the heavy icing scenario R8 compared with those stresses considering only the

structural effects due to the weight of the clean blade. Cycles to failure dropped dramatically for high velocity case and also for the heavy icing case which gives an indication that this kind of icing must be dealt with immediately to avoid the damage to the structure. Figure 6.4 and 6.5 shows the von Mises stress for clean blade exposed to wind velocity of 10 m/s and an iced blade with wind velocity of 20 m/s, it's clear that the most affected area is at the root near the necking area of the blade.

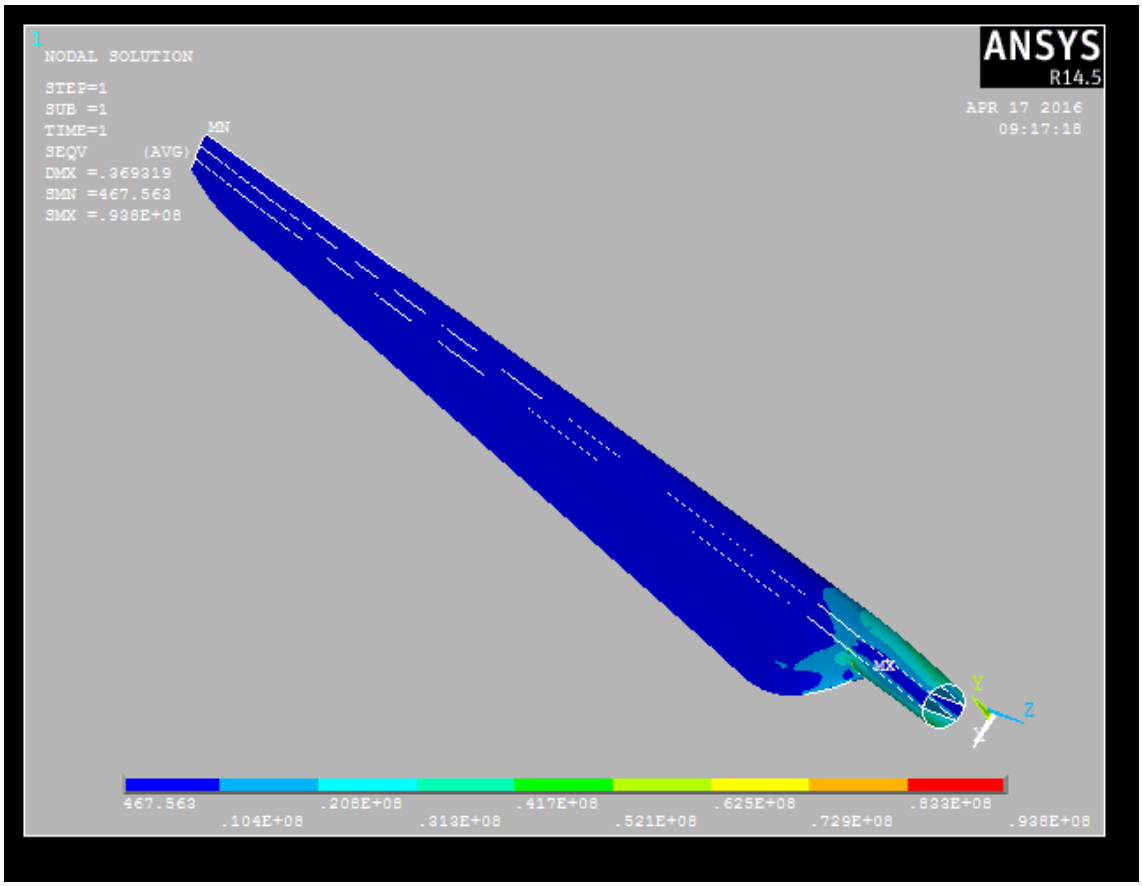

Figure 6.4: Stress concentration areas around the necking area of a clean blade with wind velocity of 10 m/s

.

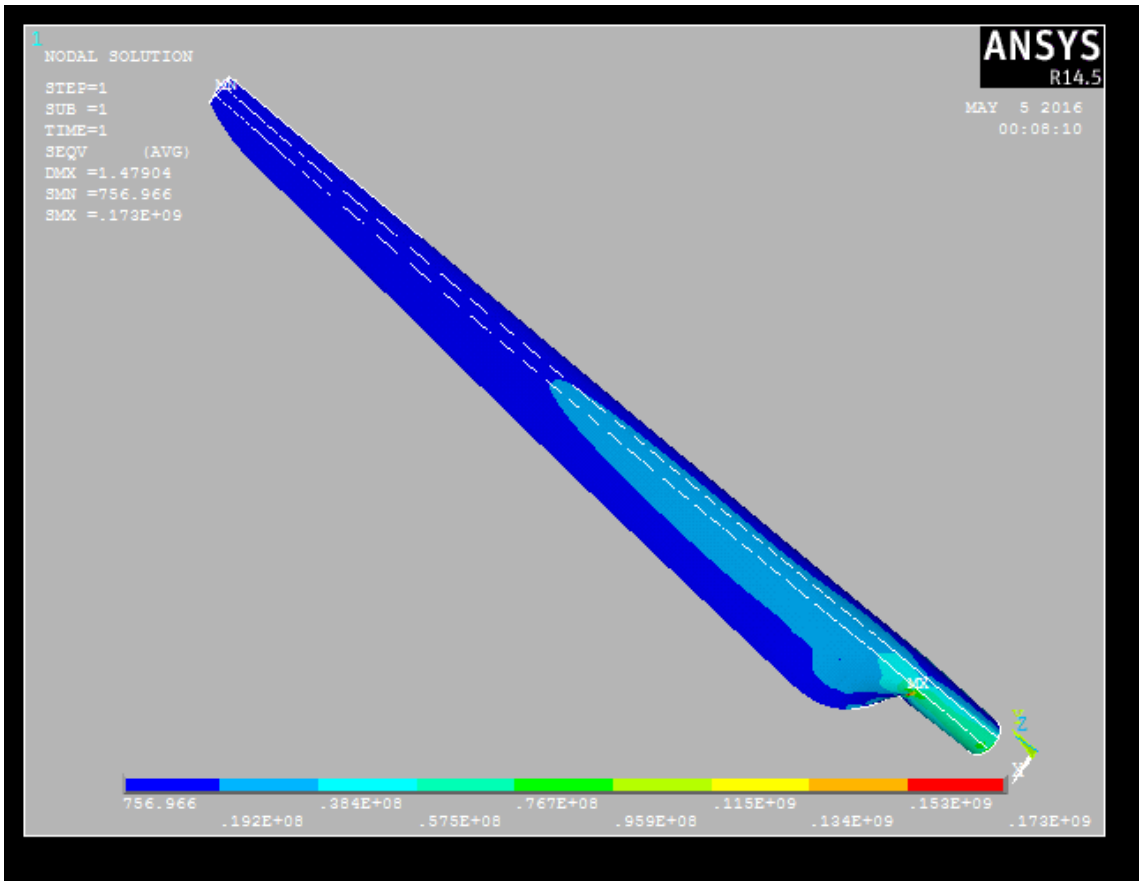

Figure 6.5: Stress concentration areas around the necking area of an iced blade with wind velocity of 20 m/s

6.4 Effect on the Structural Loading Due to the Reduction of the Natural Frequency

The reduction of the natural frequency of the turbine blade due to the ice accretion changes the structural dynamic response of the system and will have an impact on the integrity of the structure. This can be demonstrated by the effect of the ice accretion on the dynamic magnification factor associated with the vibration. Dynamic magnification factor is the ratio of the dynamic deflection at any time to the static deflection which would have resulted from the static application of the external load (Biggs, 1964). This factor reflects the increase of the structural

loading due to the vibration and thus closely related to the reduction of the fatigue life of the structure.

Figure 6.56 shows the variation of the dynamic magnification factor with the frequency ratio and the damping factor based on the structural dynamic analysis of a single degree of freedom system. As a first approximation, it can be used to illustrate the impact of the reduction of natural frequencies due to added mass of accreted ice on the dynamic load acting on the structure.

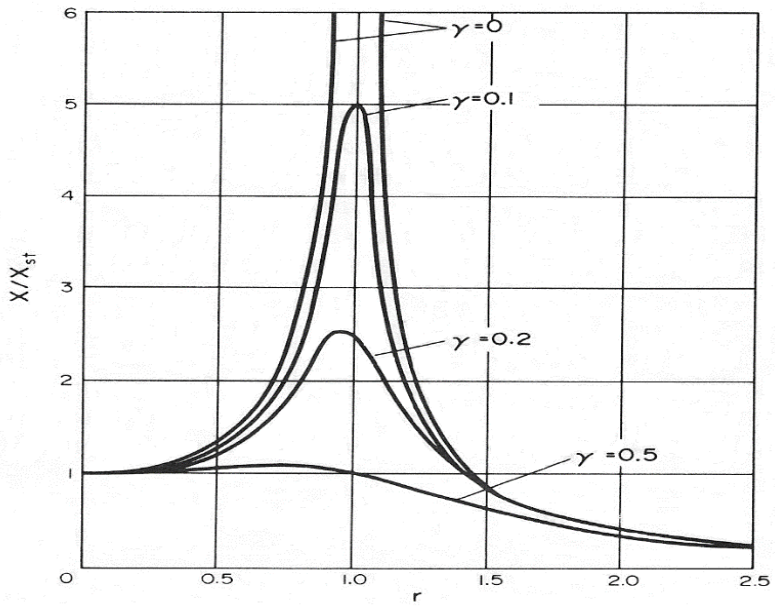

Figure 6.6: Variations of dynamic magnification factor X/X_{st} with frequency ratio r and damping factor γ, (Biggs, 1964)

The dynamic magnification factor is given by:

$$\frac{X}{X_{st}} = \frac{1}{\sqrt{[(1-r^2)^2+(2\gamma r)^2]}} \tag{6.27}$$

where r is the ratio of the excitation frequency to the natural frequency and γ is the ratio of the damping coefficient to the critical damping coefficient of the dynamic system. The rated rotating velocity for the 5- MW blades is 12 rpm which

is equivalent to 0.2 Hz and the structural damping ratio for the 5-MW wind turbine blade for all modes is 0.0047 (Jonkman, 2006b). The natural frequencies for the clean and all assumed icing scenario iced wind turbine blade for all were given in Table 5.2. By substituting in equation (6.27), the dynamic magnification factor can be calculated.

Table 6.3 presents the results of dynamic magnification factor for the iced and clean turbine blade under different icing scenarios. Under the damping factor of 0.0047 the dynamic magnification factor has been increased 4% for the moderate icing case R5, 8% for icing case R8 and 11% increase for the icing scenario R9. It can be expected that the fatigue life of the component will be reduced due to the increase of the dynamic load caused by the ice accretion.

Table 6.3: Dynamic magnification factors of iced and clean blades for damping ratios of 0.0047

State of the blade	$\frac{X}{X_{st}}$	% of increase for the magnification factor
clean	1.07	-
Moderate icing R5	1.11	4%
Heavy icing R8	1.15	8%
Heavy icing R9	1.19	11%

6.5 Summary

In this Chapter, effects of the heavy icing scenario R8 with two different wind velocities on the structural integrity of the wind turbine were investigated. ANSYS was used to perform stress analysis of the 5-MW wind turbine blade. von Mises stresses were obtained for the clean and iced blade under the two assumed wind velocities and R8 icing scenario. Remarkable reduction in the fatigue life of the blade was observed when combined the aerodynamic effect with the effect of added load due to heavy icing scenario. The effect of atmospheric icing on the dynamic magnification factor was also investigated. The magnification factor has increased under all assumed icing scenarios, which will lead to further reductions of fatigue life.

CHAPTER SEVEN

CFD ANALYSIS FOR TYPICAL AEROFOIL PROFILES

7.1 Background

Computational fluid dynamics (CFD) is a division of fluid mechanics that uses numerical methods in order to solve and analyse problems that involve different fluid flows. Computer software are used to do the calculations needed to simulate the interaction of gases and liquids with surfaces defined by boundary conditions. Furthermore, CFD offers a very powerful tool to simulate and capture the aerodynamic behaviour of a wind turbine rotor.

In this Chapter, two typical wind turbine blade aerofoils are examined to investigate aerodynamic effects due to ice accretion. Drag and lift forces are investigated for the three icing scenarios given in Chapter 5 using the CFD approach. 3D-CAD models for all cases are prepared using Rhinoceros® 5 and the CFD analysis has been achieved by commercial CFD software STAR-CCM®+. All the CFD analyses have been performed for the 2D cases using the aerofoil sections at different locations in the spanwise direction of the blade.

7.1.1 Aerofoil Geometry and Aerodynamics

In this research the linear momentum theory is used along with STAR-CCM+ for the calculation of the aerodynamic forces and the power generated for typical aerofoils. This method, as with any other method, has a number of simplifications and idealizations, which make it practical for use.

A two-dimensional flow is assumed in this research. For a long blade, which is the case of the 5-MW wind turbine blade, the spanwise velocity component is normally small as compared to the streamwise component which is perpendicular to the blade longitudinal axis.

Figure 7.1 illustrates major forces acting on a typical NACA aerofoil, as mentioned in Chapter 6, D_f is the drag force, L_f is the lift force, W is the relative air velocity, $\propto$ is the angle of attack, c is the chord of aerofoil which previously mentioned in Chapter 6, LE is the leading edge and TE is the trailing edge. The upper surface is the suction side with low air pressure and the lower surface is the pressure side with higher air pressure.

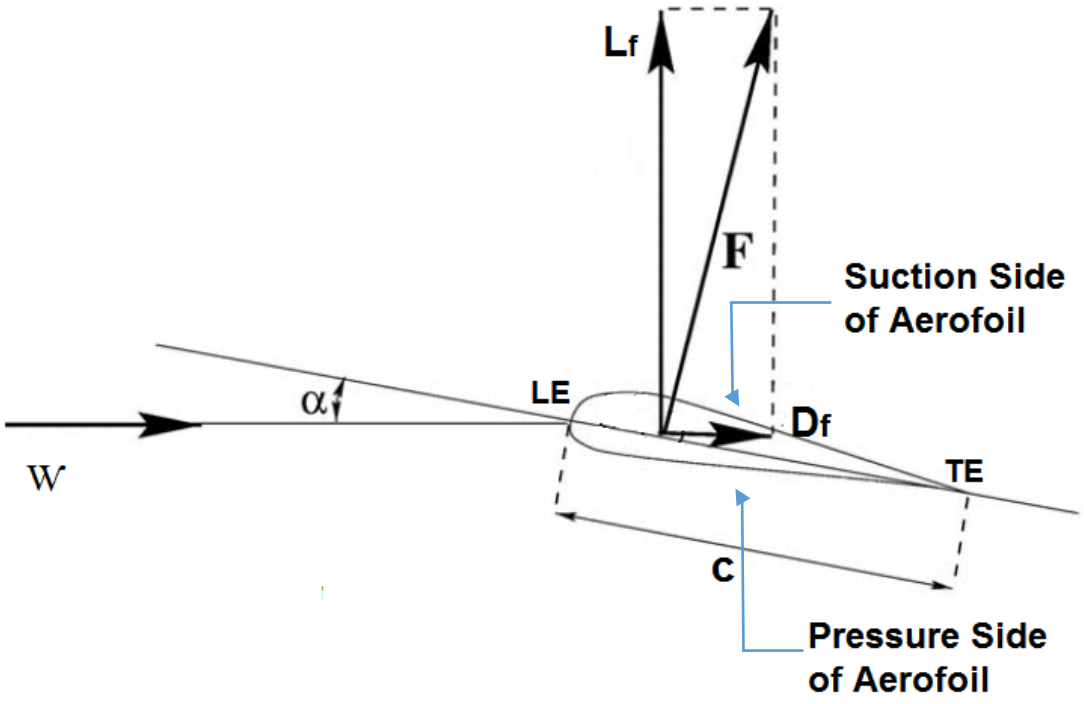

Figure 7.1: Shape of a typical NACA aerofoil (Hansen, 2015)

The resultant force F has two force components: lift force component L_f is perpendicular to the direction of the resulting relative wind velocity W and drag force component D_f is parallel to lift force direction. Both these force components

depend on the inflow angle of attack ∝. The true wind flow over the wind turbine rotor is rather complex. For a typical blade cross-section, the dominant wind velocity conditions at are shown in Figure 7.2.

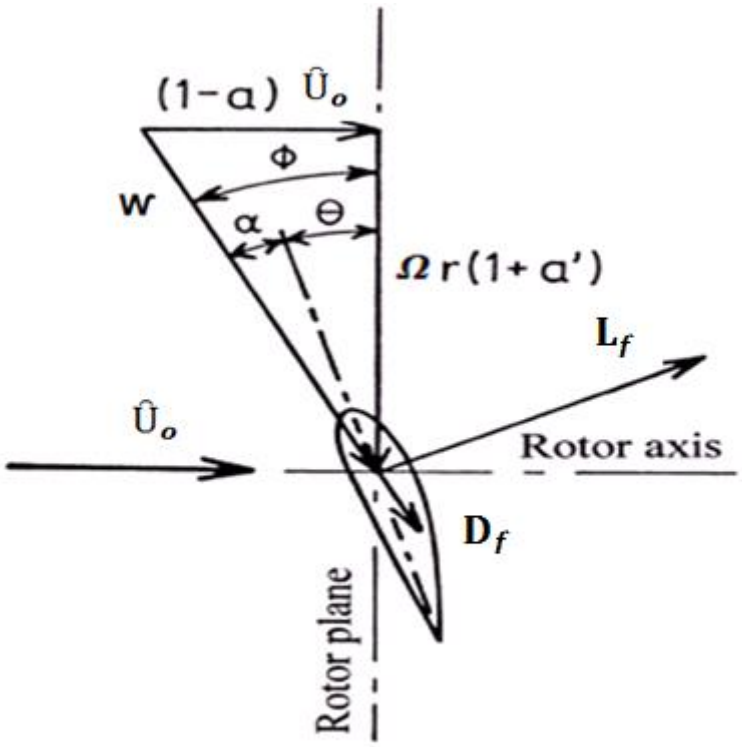

Figure 7.2: Velocity component of wind crossing an aerofoil (Risø, 2002)

The wind velocity $\hat{U}_o$ is assumed to be perpendicular to the rotor plane. This is referred to the inflow wind velocity. Due to the axial interference, the airflow velocity passes through the rotor plane will be reduced by $(a\,\hat{U}_o)$, where a was defined in Chapter 6 as the axial induction factor. For a blade element located at distance r from the rotor axis it will be moving in the rotor plane at a speed of $(\Omega\, r)$, where Ω is the rotor angular velocity. After the passing of the wind through rotor plane, a tangential slipstream wind velocity $(a'\Omega\, r)$ is introduced, where a' is the

tangential factor. The aerodynamic lift and drag forces couldn't have a rise without the resultant relative inflow wind velocity. The wind flow velocity components crossing an aerofoil are also given in the Figure 7.2 in more details, φ is the flow angle which lies between the direction of relative wind velocity on the rotating blade and the rotor plane. θ is the pitch angle and so the angle of attack is $\propto = \varphi - \theta$.

The lift and drag coefficients are functions of the angle of attack (AOA),$\propto$, the aerofoil shape and the Reynolds number Re which is defined as the ratio of internal forces to the viscous forces (Falkovich, 2011) . It is worth noting that C_L increases linearly with $\propto$ up to $\propto_{stall}$, where the aerofoil stalls. C_L reaches a maximum value when $\propto$ increases and then decreases for further increase in $\propto$. For small values of $\propto$, C_D is almost constant, but increases rapidly after stall.

The separation of the boundary layer from the upper side of the aerofoil is closely related to the stall phenomenon. Furthermore, the geometry of the profile is very important for the aerofoil stall initiation which is faster and sharper for aerofoils with thin profiles having a sharp nose as compared to thicker aerofoils. This is mainly related the way the boundary layer separates from the upper surface of the aerofoil. (Risø, 2002). By reaching the stall angle $\propto_{stall}$, a dramatic loss in the flow attachment and aerofoil lift.

7.2 Numerical Setup of the CFD Model

CFD simulations require a fluid domain surrounding the object of interest, which is the aerofoil in this study. This fluid domain may be created as a solid body in 3D-

CAD and then get the required external volume, leaving a cavity of the geometry of the aerofoil to be analyzed. The size of the domain depends on the size of the aerofoil to be analysed. Proper dimensions of the domain compared to the analysed geometry should be considered (Xing and Stern, 2007). The outside rectangle domain must be made large enough so that the flow around the aerofoil is steady and is not being affected by the walls of the domain (Chen, 2011). The inlet boundary may be taken as 20 times as the chord (Kishore et al., 2013). An aerofoil located in the middle of the icing zones (DU21) as discussed in Chapter 4 is chosen to perform the CFD power investigations. The chord of the 5-MW (DU21) aerofoil is 3.26 m so the inlet of the CFD domain is 20×3.26 = 65.2 m. The top and bottom boundaries have the dimension of (8×3.26+3.26+10×3.26 = 61.9 m). Constructing the 3D-CAD model for aerofoil CFD analysis took place using Rhinoceros according to the schematic diagram shown in Figure 7.3.

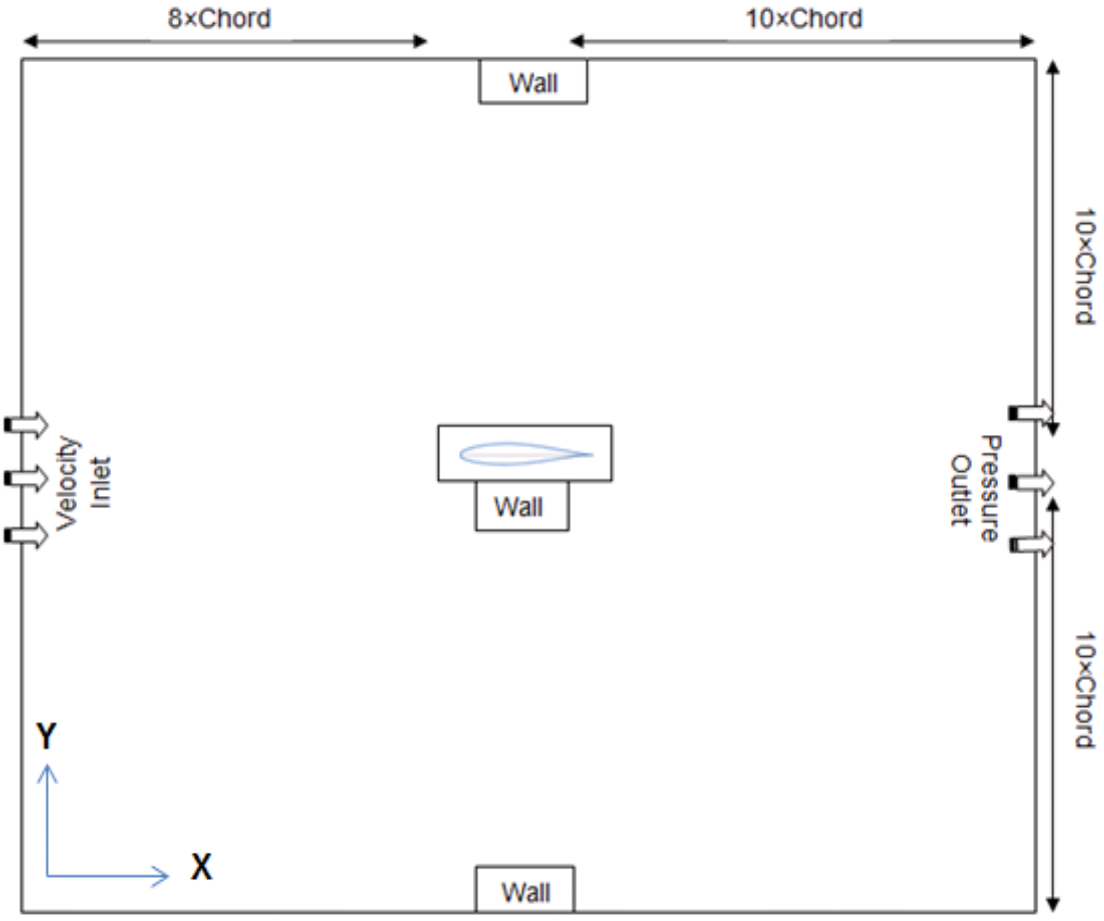

Figure 7.3: Schematic diagram of applied boundary conditions in the domain

The simulation domain is then meshed, and for which physics is solved and defined using regions and boundaries. For subsonic, incompressible flow cases like the case in this research, walls, inlet and at least one outlet boundaries conditions must be fulfilled (Versteeg and Malalasekera, 2007).

To prepare the CAD model, a solid parallelogram is established with the dimensions illustrated in the CFD domain as shown in Figure 7.3. The solid CAD model is then imported by STAR-CCM+. The rendered solid geometry in Rhinoceros is shown in Figure 7.4.

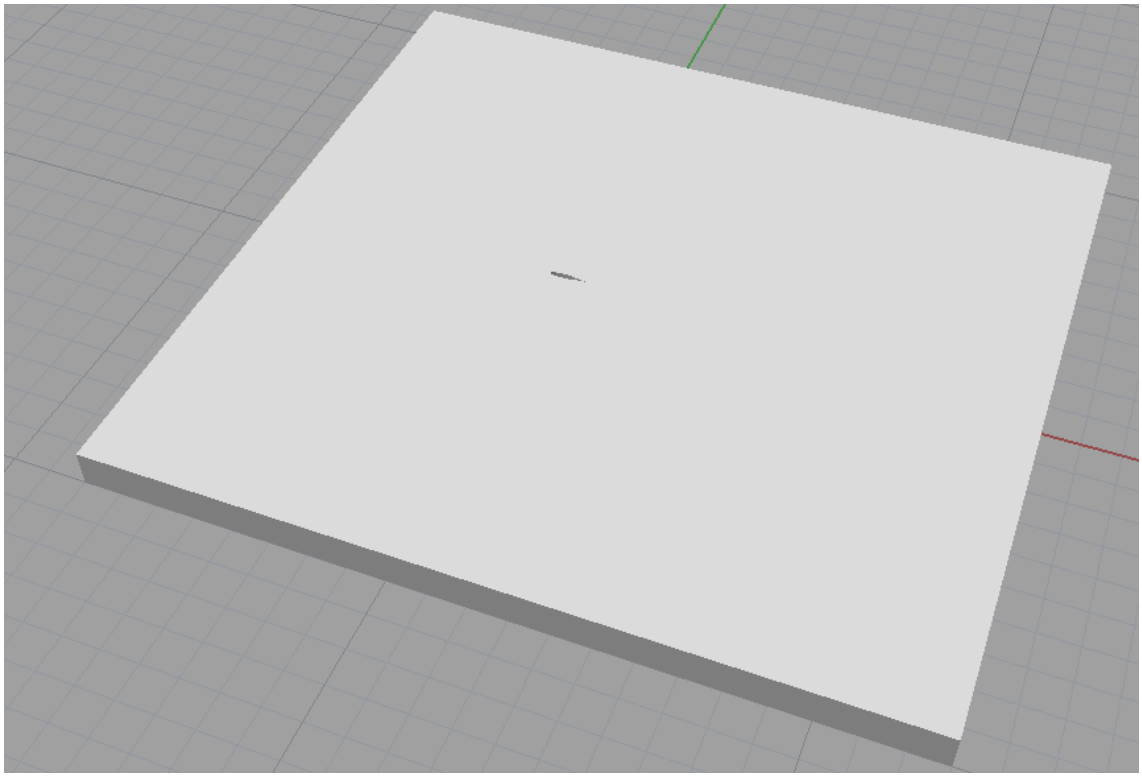

Figure 7.4: The rendered solid parallelogram with the aerofoil profile in the middle.

In this research, the flow was considered incompressible and the (k-ϵ) turbulence model was used. A y+ value less than 10 was used near the wall for all cases.

7.2.1 Boundary Conditions:

1) Inlet: Velocity Inlet condition is specified at the left boundary of the domain. Inlet velocity is assumed to be constant and with a magnitude of 10 m/s.

2) Outlet: Pressure outlet condition is specified at the right boundary of the domain. This is interpreted as the static pressure of the environment into which the flow exhausts.

3) Wall condition is specified for all other boundaries including aerofoil, top, bottom, facing and reverse sides of the solid parallelogram. A solid wall parallel to the x-direction was considered and no-slip condition at the solid

wall of the aerofoil was enforced. The main assigned boundaries in STAR-CCM+ are shown in Figure 7.5.

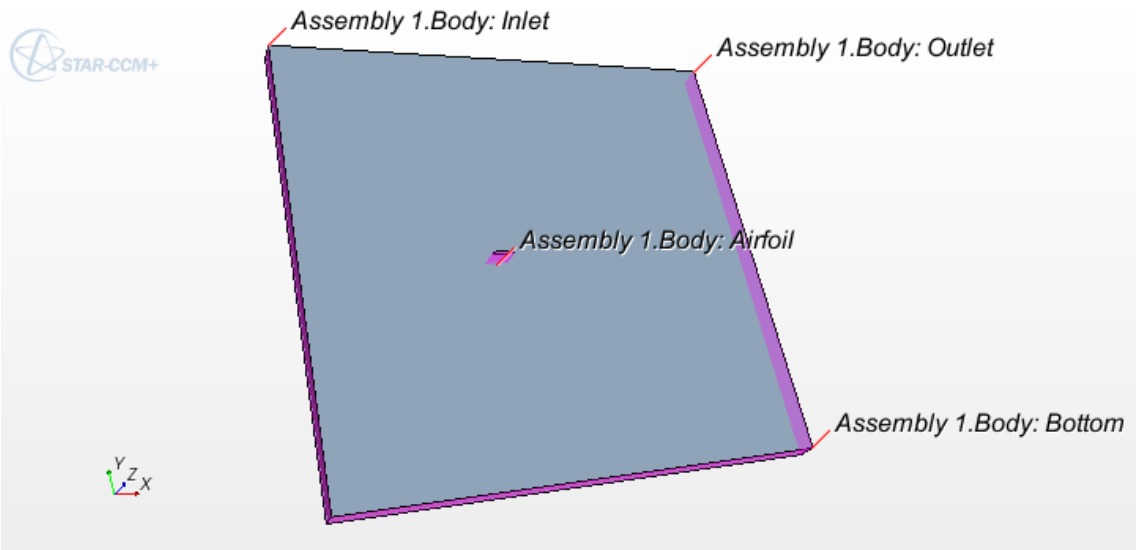

Figure 7.5: The main assigned boundary parts for the CFD domain in STAR-CCM+

7.2.2 Initial Conditions:

1) Pressure: zero gauge pressure.

2) Velocity: initialized to the value of 0.0 m/s for the whole model domain.

3) Constant turbulence model with value of 0.01 and turbulence velocity scale of 1 m/s and turbulence viscosity ratio of 10.

Turbulence intensity measures how much the wind varies typically within 10 minutes and is given by:

$$L_w = \frac{\delta_u}{u} \tag{7.1}$$

where L_w is the turbulence intensity, δ_u is the standard mean deviation of velocity

averaged over 10 min and u is the air velocity averaged over the same time period (Marjaniemi et al., 2001)

Other physical specifications are given in Table 7.1. The physical options represent the overall environmental situation. For simplicity, the analysis was chosen to be two dimensional under steady state condition. The moving medium is the airflow which is gas. The segregated flow reflects the pressure equilibrium at the inlet and outlet boundaries which encourages the airflow to be under the influence of gravity. The viscous regime is turbulent with (k-ϵ) Reynolds-Averaged Turbulence. The (k-ϵ) represents a flow with low Reynolds numbers (1×10^6 - 9×10^6) (Fuerle et al., 2010) and according to (Virk and Holdo, 2008) the use of (k-ϵ) is common for the wind engineering application. The Reynolds number may be calculated using:

$$R_e = \frac{\rho_{air}\, u\, \underline{\mathrm{d}}}{\mu} \tag{7.2}$$

where u is the inlet air velocity and assumed to have the magnitude of 10 m/s and μ is dynamic viscosity of air. Density of air ρ_{air} was given in Chapter 6 as 1.21 kg/m^3 at 20 ºC and 1.26 kg/m^3 at -10 ºC (Bertin and Smith, 1998) , $\underline{\mathrm{d}}$ is usually taken to be the aerofoil chord which is 3.26 m for the 5-MW (DU21) aerofoil section (Jonkman et al., 2009). Dynamic viscosity of the air at -10 ºC is 1.67×10^{-5} N-s/m^2 (Elger et al., 2014). So under these conditions, Reynolds numbers R_e = 2.62×10^6 which can fit in Reynolds-Averaged Turbulence (k-ϵ) range.

Table 7.1: Physical properties used in STAR-CCM simulation

Physical parameters	Description
space	2-Dimensional
Time	Steady
Material	Gas
Flow	Segregated
Equation of State	Constant Density
Viscous Regime	Turbulent
Reynolds-Averaged Turbulence	k-ϵ Turbulence

7.2.3 Meshing of the CFD Model

Surface remesher, polyhedral mesher and prism layer mesher were chosen from mesh model selection. In order to improve the overall quality of the surface and optimize it for the volume mesh models, the Surface Remesher model is often used. The remeshing is basically based on a target edge length. Based on the boundaries, localized refinement can also be included.

The use of Polyhedral cells has an important advantage such that they have about ten neighbours, while Tetrahedral control volumes have only four neighbours. And so, much better approximated for gradients and more storage computing operations per cell can be expected with the use of Tetrahedral cells. This will lead to higher accuracy (Peric, 2004).

Prismatic cell layers will be added next to wall boundaries by the use of Prism layer mesher which is also a region-based.

Main meshing reference values are:

- The base size is a characteristic dimension of the model and can be set as the diameter of the inlet. As the aerofoil is the main geometry to be analysed, the base size may represent the dimension perpendicular to the chord and assumed to be from 0.7 to 1.0 m.
- Number of prism layers next to walls is assumed 2 to 4.
- Prism layer thickness relative size is a percentage of the prism layer thickness to core mesh size. By referring to Figure 7.4, core mesh size is the length from analyzed object (aerofoil) to the top boundary, which is 32 m. Assuming three prism layers (3×0.8=2.4 m) are used, the Prism layer thickness relative size is (2.4/32= 7.5%).
- Surface relative target size is the average domain mesh cell surface size compared to the base size. Default value of 100% will be adopted.
- Surface relative minimum size is the smallest allowable dimension of a cell in the mesh domain and will be taken as the default value of 25% of the base size.

Table 7.2 is a summary of the meshing reference used in this study.

Table 7.2: Meshing reference values

Meshing property	Meshing reference values
Base size	1m
Number of prism layers	2
Relative size	5%
Surface relative minimum size (Domain)	25%
Surface relative target size (Domain)	100%

The relative velocity for the 5-MW aerofoil section (DU21) is taken to be 50.7 m/s (Homola et al., 2012). The volume mesh is illustrated in Figure 7.6.

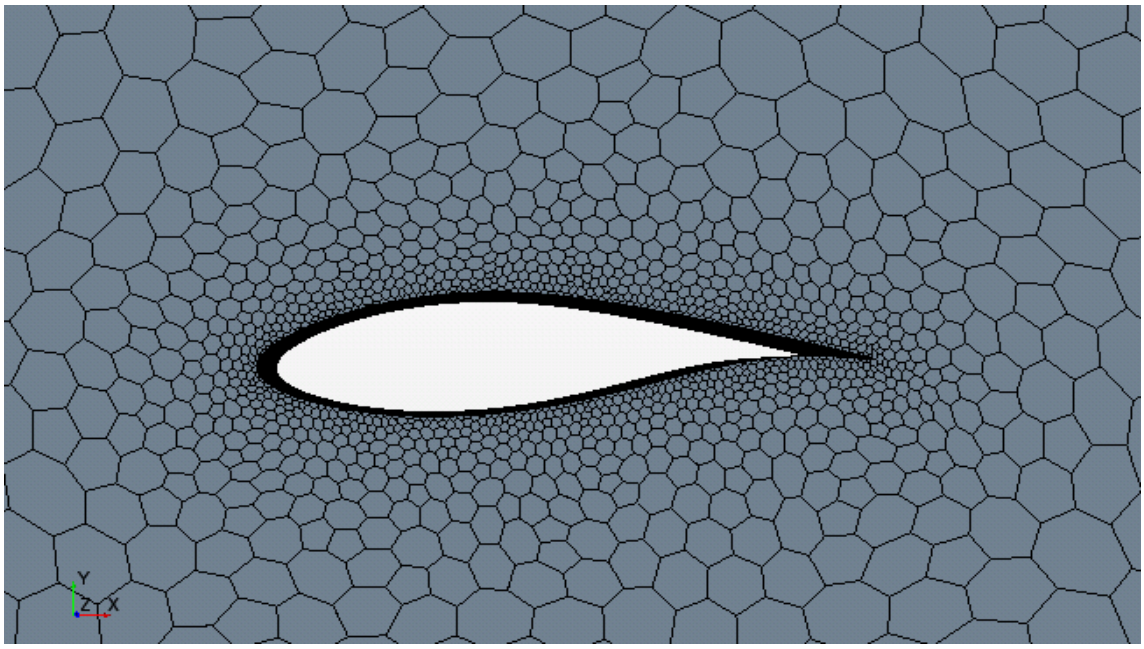

Figure 7.6: 3D volume meshing for clean 5-MW (DU21) aerofoil profile

After the volume mesh was performed, the meshing has converted to the 2D mesh. Figure 7.7 shows the 2D mesh. According to the mesh diagnostics report provided by the software, 100% of the meshing faces are valid and have the value of unity.

The overall volume change validity is 100%. The STAR-CCM+ user guide states that a face validity of 1.0 means that all face normals are correctly pointing away from the cell centroid and in a good quality cell (Zhang et al., 2014). Statistical data about volume and surface 2D mesh is given in Table 7.3.

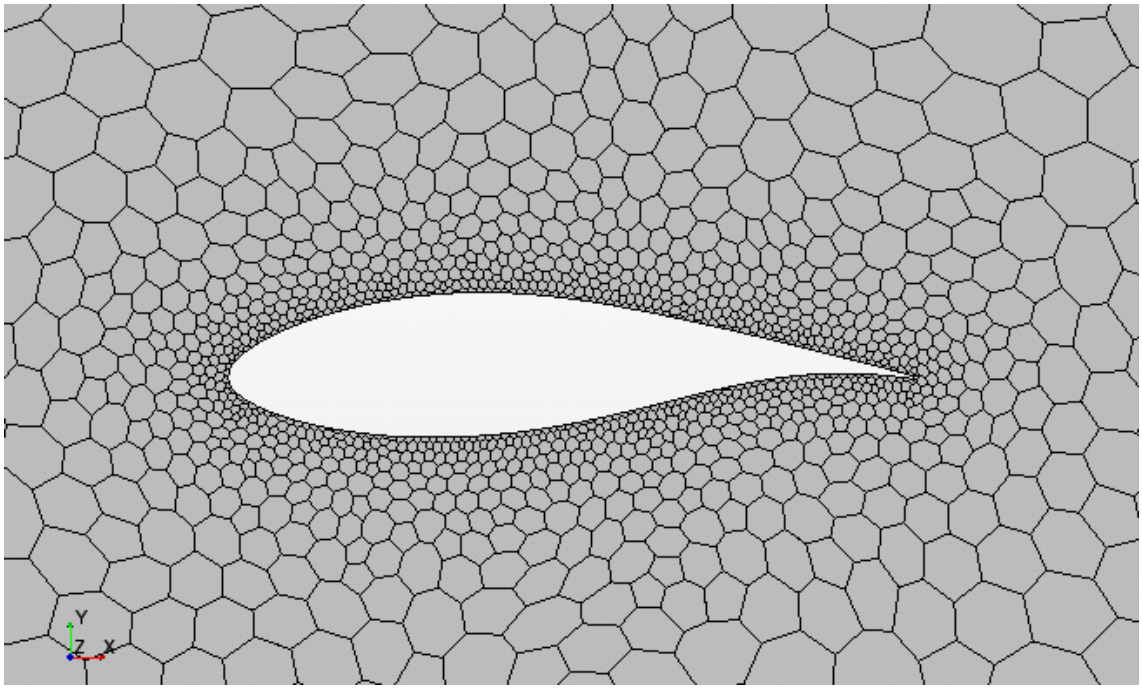

Figure 7.7: 2D meshing for clean 5-MW (DU21) aerofoil profile

Table 7.3: Statistical data about volume and surface meshing

Mesh type	No of cells	No of Faces	No of Vertices
Volume mesh (3D)	813627	3656059	247914
Surface mesh (2D)	89875	268404	179750

Mesh density study has been taken to ensure the reliability of the results for drag and lift coefficients. The common CFD technique starts with a relatively coarse mesh with refinements being gradually applied until changes in the results are small enough (Chen, 2011).

Table 7.4 includes different meshing schemes for the same case. The average number of cells for the 2D analysis was about 90,000. Running time for each case was about one hour with 500 steps for each run.

Table 7.4: Different meshing schemes for clean 5-MW (DU21) aerofoil

Meshing Scheme Number	**Meshing Property**					**Drag coefficient C_D**	**deviation from 1st reading**
	Base size (m)	Number of prism layers	Relative size	Surface relative minimum size	Surface relative target size		
1	1.00	2	5	25	100	0.0082	0%
2	0.95	2	5	5	25	0.0081	1.2%
3	0.90	3	5	5	25	0.0081	1.2%
4	0.80	3	5	5	25	0.0084	2.4%
5	0.70	3	5	5	25	0.0085	3.6%
6	2.00	3	5	25	100	0.0125	52.4%

By comparing results to (Homola et al., 2012), second scheme was the nearest to authors results as they have for the same 5-MW (DU21) aerofoil a value of 0.007 for drag coefficient. It is clear from Table 8.4 that reducing values of base size in schemes 3 and 4 increases deviation from the first scheme. Result of coarser meshing scheme number 5 wasn't very encouraging with high deviation rates for both coefficients being obtained. The second scheme will be adopted for all other assumed icing scenarios. A detailed volume mesh view near the aerofoil middle edge and at the leading edge is illustrated in Figure 7.8.

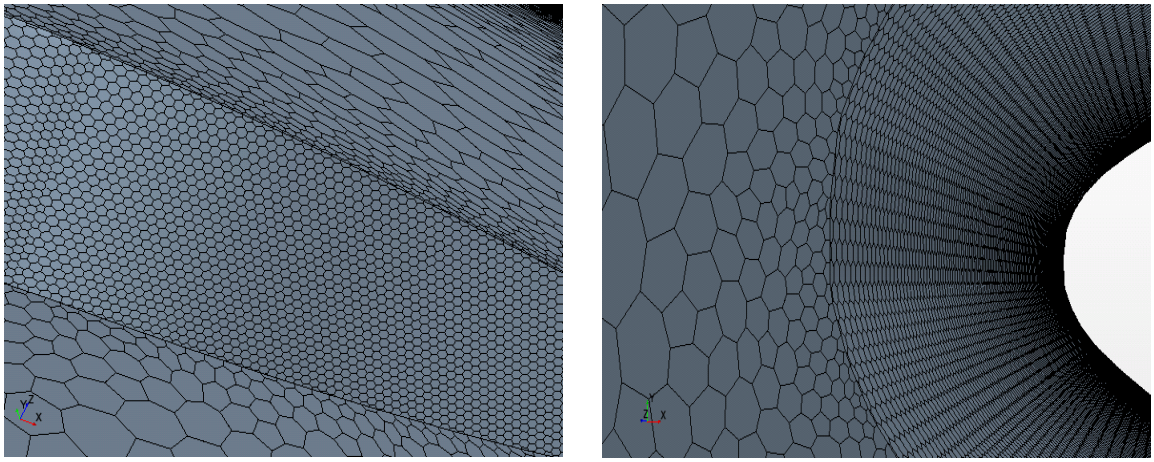

Figure 7.8: A detailed 3D mesh view for (DU21) aerofoil section near aerofoil edge (left) and at the leading edge (right)

According to STAR-CCM+ user guide (Zhang et al., 2014), if the residuals lines are going down, this means that the flow residuals are converging well. Figure 7.9 illustrates the convergence of the residuals during the running of the program.

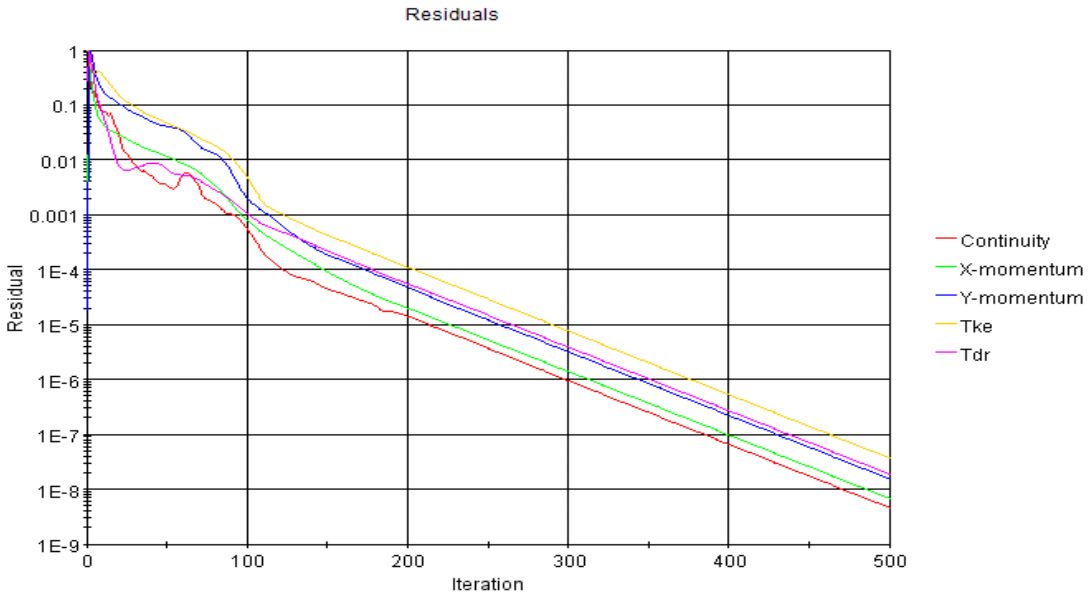

Figure 7.9: Residuals plot appeared after running of (DU21) aerofoil analysis

7.3 Aerodynamic Effect Due To the Different Icing Scenarios of the 5-MW Aerofoil Profile (DU21)

In order to study aerodynamic effects of the three assumed icing cases given in Chapter 5, one section of the 5-MW wind turbine blade, (DU21), was selected to carry out the CFD analysis. The aerofoil is selected in the middle of the assumed five icing zones illustrated in Chapter 4. The location of the aerofoil is illustrated in Figure 7.10.

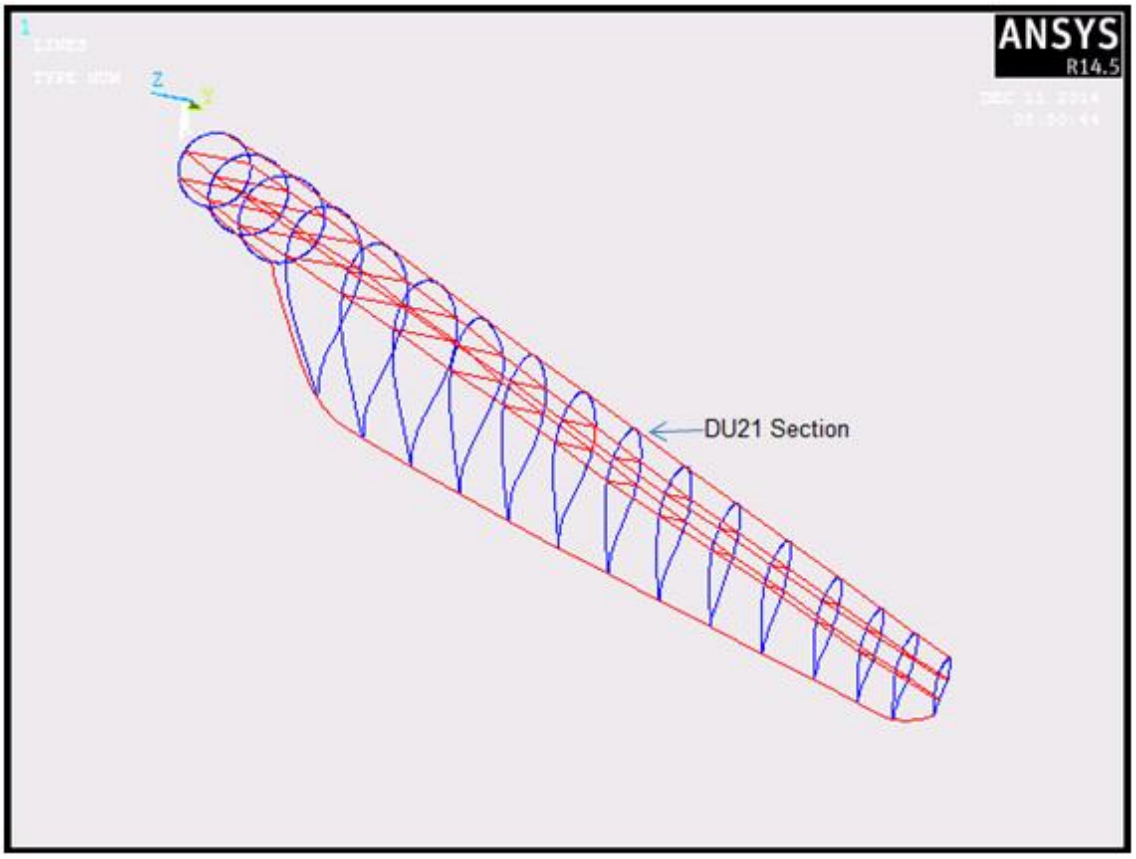

Figure 7.10: 5-MW wind turbine blade with section DU21 in the middle

In order to investigate the effect of icing on the aerodynamically behaviour of the wind turbine blade, the thickness of accreted ice on the leading edge is determined by referring to ISO 94242 International Standard (ISO, 2001b).

Based on the new approach for estimating the largest aerofoil section width $\hat{W}$ given in Section 4.4, the maximum ice thickness may be calculated using the following relation (ISO, 2001b):

$$Ł = \frac{\hat{m} \times 4 \times 10^6}{\pi \times \rho_{ice} \times \hat{W}} \quad (7.3)$$

where $\hat{m}$ is preliminary value for accreted ice mass given for different icing cases shown in Table 4.8, ρ_{ice} is the density of ice which will be considered as hard rime with density of 900 kg/m^3 (Makkonen, 2000). Values of maximum ice thickness for the different icing scenarios are calculated according to equation (7.3) and presented in Table 7.5.

Table 7.5: Maximum ice thickness for the three assumed icing scenarios

Icing Scenario	Preliminary value for ice mass $\hat{m}$ (kg/m)	Maximum accreted ice thickness (mm)
Moderate R5	5	10.5
Heavy icing R8	28	59.0
Heavy icing R9	50	105.4

According to a typical ice accretion on wind turbine blade, the maximum thickness of the accreted ice is located at tip of the leading edge at any section of the blade due to the continuous rotation of the blades, the ice thickness gradually decreases away from the leading edge towards the middle of the blade section, the thickness actually vanishes when it reaches the middle of the section, at this point, the profile of the accreted ice touches the outer skin of the blade (ISO, 2001b). It is worthwhile

to mention that ice accretion is usually minimum or no icing occurs at the middle of the blade section where maximum width of the blade is located.

As numerical setup was prepared for both clean and iced blade, the accreted ice thickness associated to each icing scenario given in Table 7.5 will be added to the clean profile of the blade to generate the 3D-CAD models representing the different assumed icing cases in the Rhinoceros environment. It is important to notice that by equation (7.3) the maximum thickness of the accreted ice on the leading edge of the blade can be estimated, this maximum thickness starts to decrease as moving from the nose of the leading edge towards the middle of the blade section at where maximum width of the bade section, this means that ice accretion thickness vanishes at the middle of the blade section whereas it reaches maximum at the nose of the leading edge.

Figure 7.11 shows how the new thickness profile of accreted ice has been added to the clean profile, the Figure shows a small amount of ice accumulated on the leading edge in yellow colour.

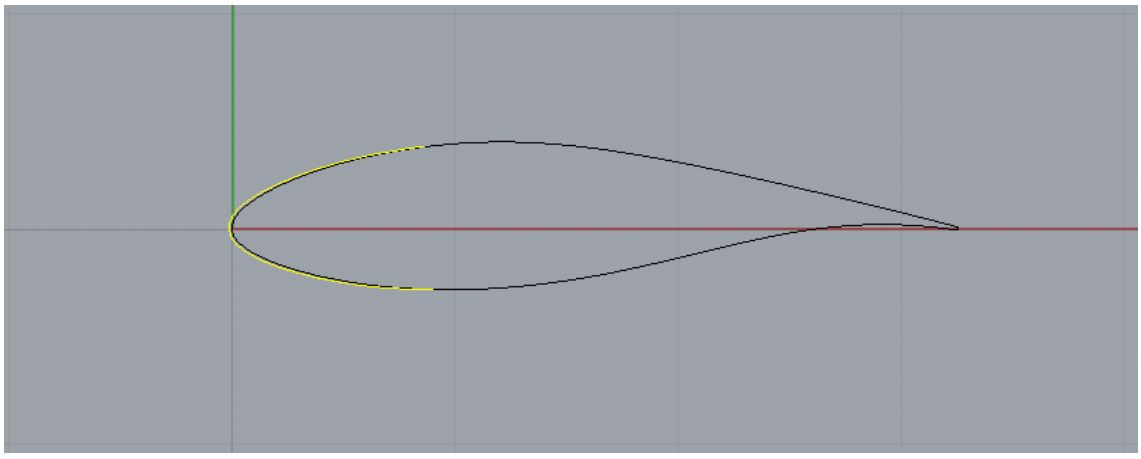

Figure 7.11: Icing profile added to the aerofoil for the moderate scenario

For heavy icing scenario R8, maximum ice thickness is 59 mm. Figure 7.12 shows the accreted ice on the aerofoil profile.

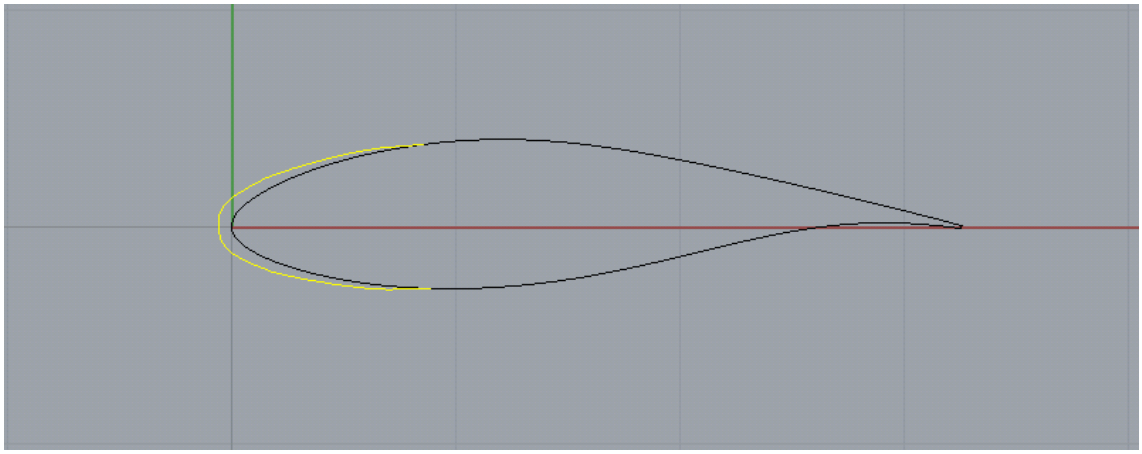

Figure 7.12: Icing profile added to the aerofoil for the heavy icing R8 scenario

The icing profile for the third assumed icing scenario R9 is illustrated in Figure 7.13. A considerable increasing in the accreted ice thickness is clear from the Figure 7.13.

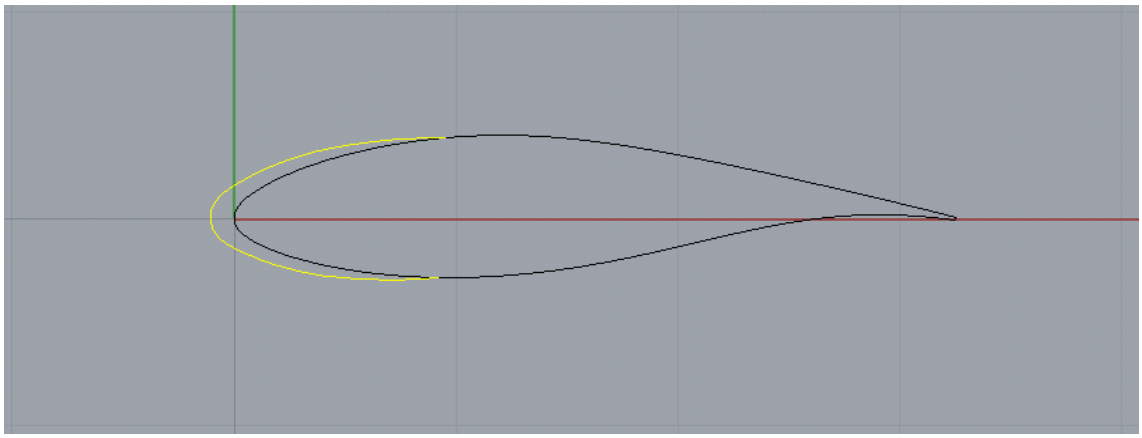

Figure 7.13: Icing profile added to the aerofoil for the heavy icing R9 scenario

According to (Manwell et al., 2009), surface roughness height for the ice may generally reaches 1×10^{-4}. The cell height (layer thickness near the wall) in the current numerical setting was in the range of 1×10^{-3} m. In their study about

wind turbine performance under icing conditions, (Jasinski et al., 1998) used roughness heights of $9 \times 10^{-4} - 19 \times 10^{-4}$ m for 450 kW iced wind turbine. For icing study of NACA 63418, (Mortensen, 2008) used value of 5×10^{-6} m for ice roughness height and the author concluded that flow discrepancies due to the surface roughness were not captured. By assuming surface roughness in the order of 1×10^{-5} m, the effects on aerodynamic behaviour on the aerofoil can be neglected.

Drag coefficient represent the ratio of drag force to the total dynamic force which is the total force generated by air and lift coefficient is the ratio of lift force to the total dynamic force. Both coefficients play crucial role in the process of power generation of the wind turbine, this can be explained as for a given air velocity, constant chord length and constant air density for a certain temperature, different values for lift or drag coefficient make a lot of difference for the lift and drag forces values and power is simply force by velocity. The aerodynamic load response is basically the result of both the lift force which is perpendicular to the airflow and drag forces which is in the direction of the airflow.

The design of an aerofoil shape is aimed to create differential pressure between the upper and lower surfaces in order to create a net force perpendicular to the direction to the incoming wind. As a result of this, rotors must be carefully oriented. In this study, drag and lift coefficients are numerically calculated for angles of attack (AOA) of 0º, 5º, 10º, 15º, and 20º using STAR-CCM+. As mentioned in Chapter 6, the optimum angle (AOA) is 15º as maximum lift can be captured. Results of drag and lift coefficients for 5-MW (DU21) aerofoil section are given in Table 7.6.

Table 7.6: 5-MW (DU21) drag and lift coefficients for different assumed icing scenarios

AOA	Clean Blade		Moderate Icing		Heavy Icing R8		Heavy Icing R9	
	C_D	C_L	C_D	C_L	C_D	C_L	C_D	C_L
0 º	0.008	0.401	0.009	0.393	0.010	0.382	0.011	0.382
5 º	0.012	0.902	0.012	0.881	0.014	0.930	0.022	0.863
10 º	0.021	1.471	0.034	1.691	0.029	1.711	0.032	1.352
15 º	0.038	1.880	0.036	1.810	0.035	1.732	0.035	1.701
20 º	0.072	1.532	0.078	1.513	0.079	1.390	0.078	1.472

Table 7.6 shows results for drag and lift coefficients of clean and iced aerofoil under the three assumed icing scenarios. General trend for drag coefficient is that it increases with the increase of the angle of attack (AOA) starting from 0º to 20º.It also increases with the increase of the icing load from moderate to heavy icing. Lift coefficient increases in the same trend but by smaller values as compared to the drag coefficient. As expected, after (AOA) of 15º, lift coefficient starts to decrease when approaching stalling of aerofoil profile due to the separation of the boundary layer from the upper side of the aerofoil.

Drag coefficient kept increasing by the increase of the severity of the icing scenarios while on the other hand lift coefficient decreases with the increase of icing from moderate to heavy scenarios. Figures 7.14 illustrates the changes for Lift coefficients and Figure 7.15 shows changes in drag with respect to the different assumed icing cases. For the cases of moderately iced aerofoil and clean aerofoil, both coefficients were compared with the work of (Homola et al., 2012) with good agreement achieved especially up to (AOA) of 15º. Also (Turkia et al., 2010) have

conducted a study for similar aerofoil with (AOA) from -6º to 10º for moderate icing case having near values for drag and lift coefficients.

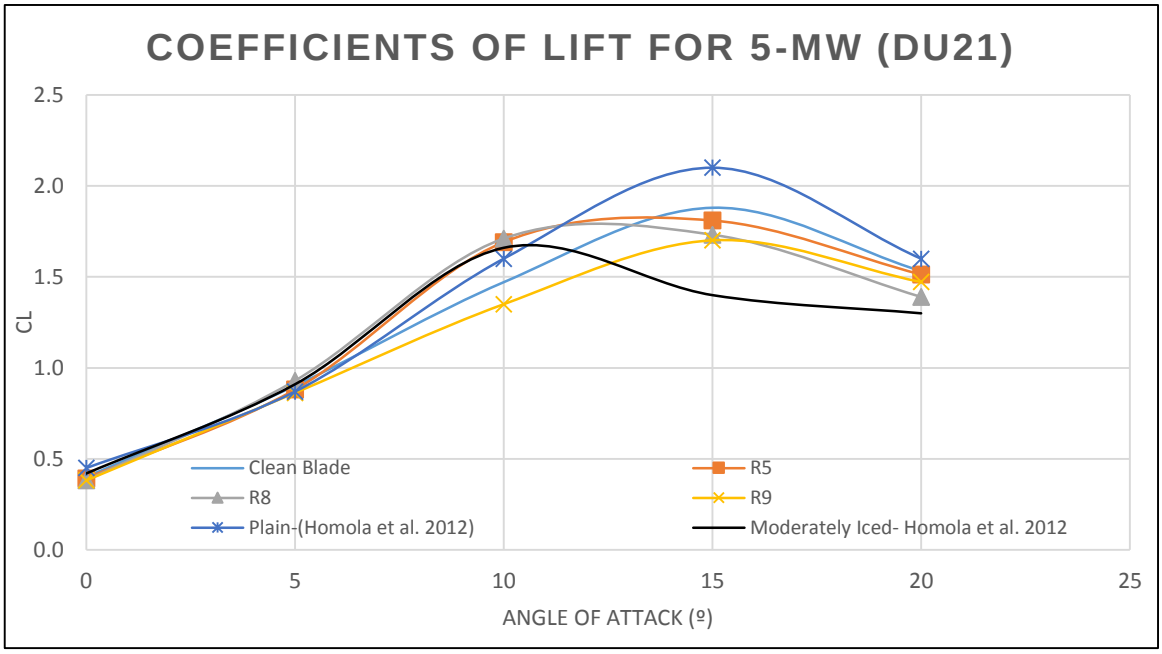

Figure 7.14: Lift coefficeints for clean and iced 5-MW (DU21) aerofoil profile

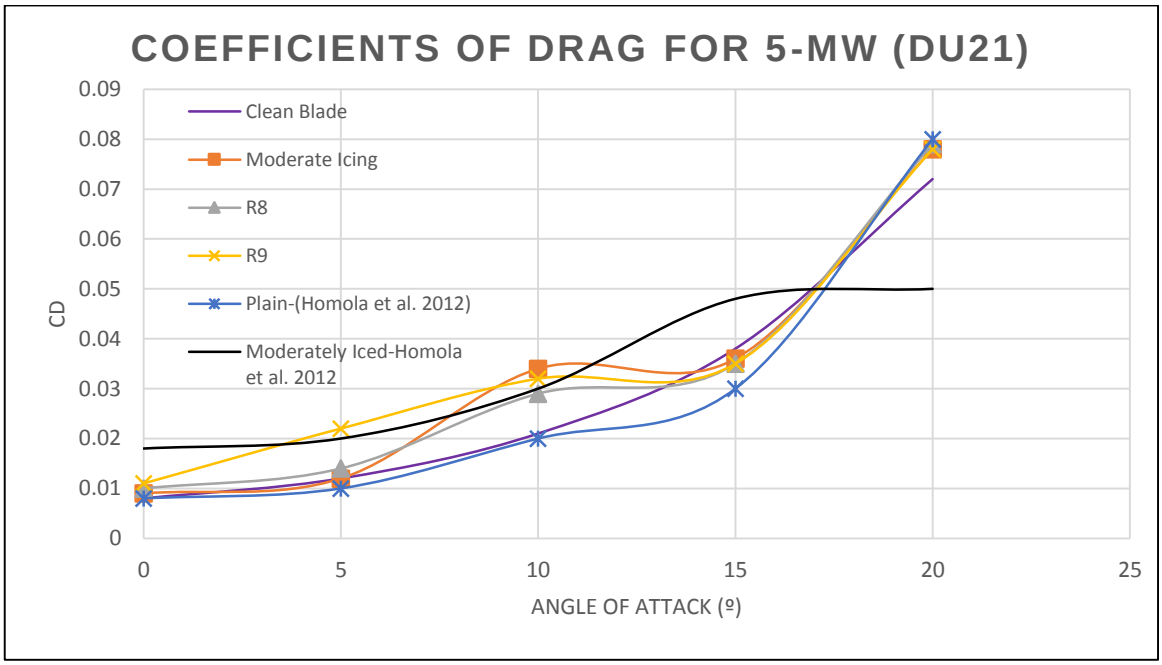

Figure 7.15: Drag coefficeints for clean and iced 5-MW (DU21) aerofoil

Turbulence intensity is not the same for clean and iced wind turbine aerofoil. The value of turbulence intensity increases with the existence of accreted ice on the blade (Manwell et al., 2009). In his CFD numerical analysis , (Mortensen, 2008), assumed a value of 0.1 for turbulence intensity for several cases of an iced NACA 63418.

The ratio of lift to drag coefficients is illustrated in Figure 7.16 for all assumed icing cases along with the case of clean blade, it's clear that the ratio of the clean blade case is on the top of all iced cases followed by the moderate ice case, the maximum ratio is noticed between AOA of 5º-10º this mainly because the increase of lift wasn't accompanied with an decrease in drag at the same rate. All cases are almost share the same trend from AOA of 15º-20º as the increase of drag coefficient happened after reaching stall angle of 15º along with decrease of lift.

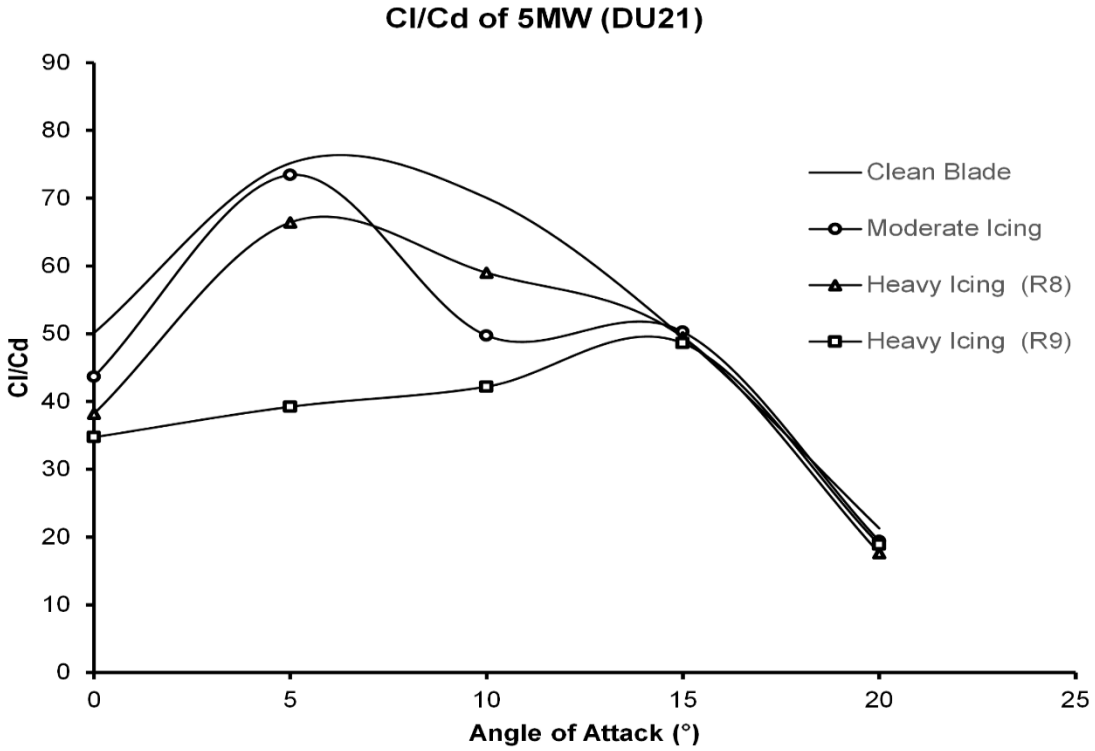

Figure 7.16: Ratio of lift / drag coefficients for clean and iced 5-MW (DU21) aerofoil

(Mortensen, 2008), assumed a value of 0.1 for turbulence intensity for all iced cases of 2-MW wind turbine blade, the author concluded that the changes in the values of drag and lift coefficients were very small. In this research the value of turbulence intensity was given in in section 7.2.2 as 0.01, by considering a value of 0.1 for turbulence intensity as an example for the case of heavy icing R8 at AOA of 15º, the value of the drag coefficient increased from 0.035 to 0.036 and that for the lift coefficient decreased from 1.73 to 1.71, which is a very small change.

7.4 Aerodynamic Effect Due To the Irregular Icing Profile of the 5-MW (DU21) Section

The icing profile of a wind turbine blade has usually different shapes according to several factors explained in section 2.3.4, main factors are the wind velocity and air temperature. In this section, the aerodynamic effect of an irregular iced profile for DU21 section will be addressed. The assumed air velocity and temperature were 10 m/s and -10 ºC respectively, the simulation was for 1 hour (Virk et al., 2012). The CAD model for the iced aerofoil profile was prepared in Rhinoceros for 5 different angles of attack, the model then exported to STAR-CCM+ in order to perform the aerodynamic analysis. The rendered CAD model of the aerofoil as appeared in Rhinoceros is shown in Figure 7.17

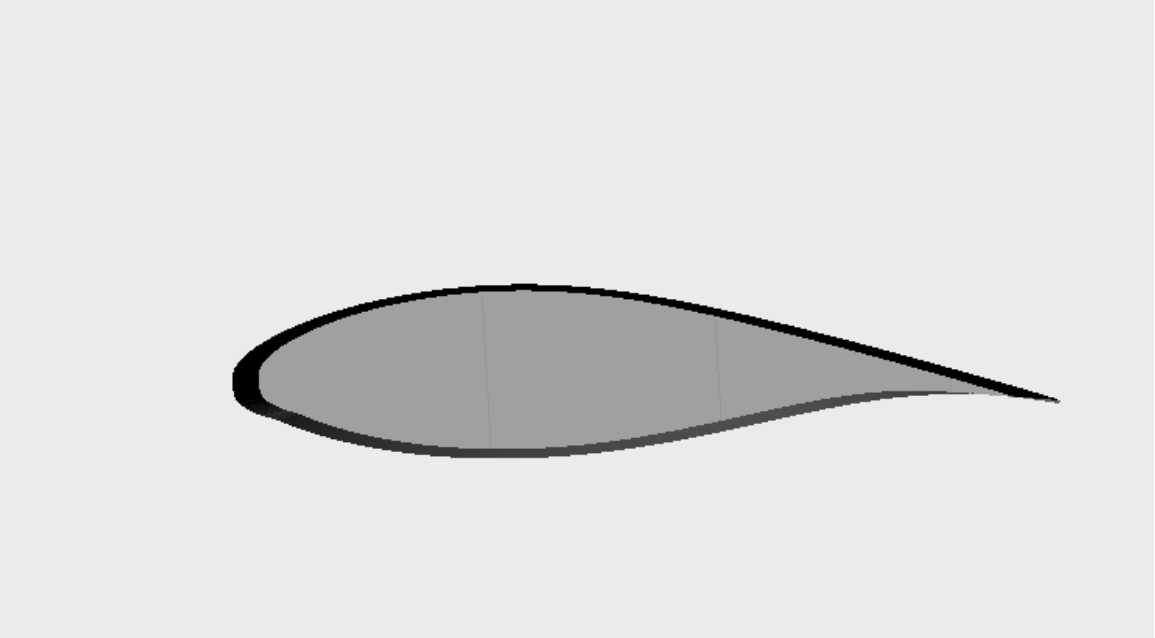

Figure 7.17: CAD model for the irregular iced DU21 section as appeared in Rhinoceros

The results for lift and drag coefficients for the irregular iced profile along with other icing scenarios are given in Table 7.7

Table 7.7: 5-MW (DU21) drag and lift coefficients all icing cases

AOA	**Clean Blade**		**Irregular Icing Profile**		**Moderate Icing**		**Heavy Icing R8**		**Heavy Icing R9**	
	C_D	C_L	C_D	C_L	C_D	C_L	C_D	C_L	C_D	C_L
0 °	0.008	0.401	0.008	0.395	0.009	0.393	0.010	0.382	0.011	0.382
5 °	0.012	0.902	0.011	0.872	0.012	0.881	0.014	0.930	0.022	0.863
10 °	0.021	1.601	0.028	1.77	0.034	1.691	0.029	1.711	0.032	1.352
15 °	0.038	1.880	0.036	1.84	0.036	1.810	0.035	1.732	0.035	1.701
20 °	0.072	1.532	0.076	1.52	0.078	1.513	0.079	1.390	0.078	1.472

The results show a small reduction in left coefficients as compared to the clean blade for all AOA except the value for 10º, the irregular icing profile has in general

higher values for lift coefficients as compared to heavy icing and moderate icing cases.

The drag coefficients for all icing cases given in Table 7.7 are illustrated in Figure 7.18 and lift coefficients are shown in Figure 7.19

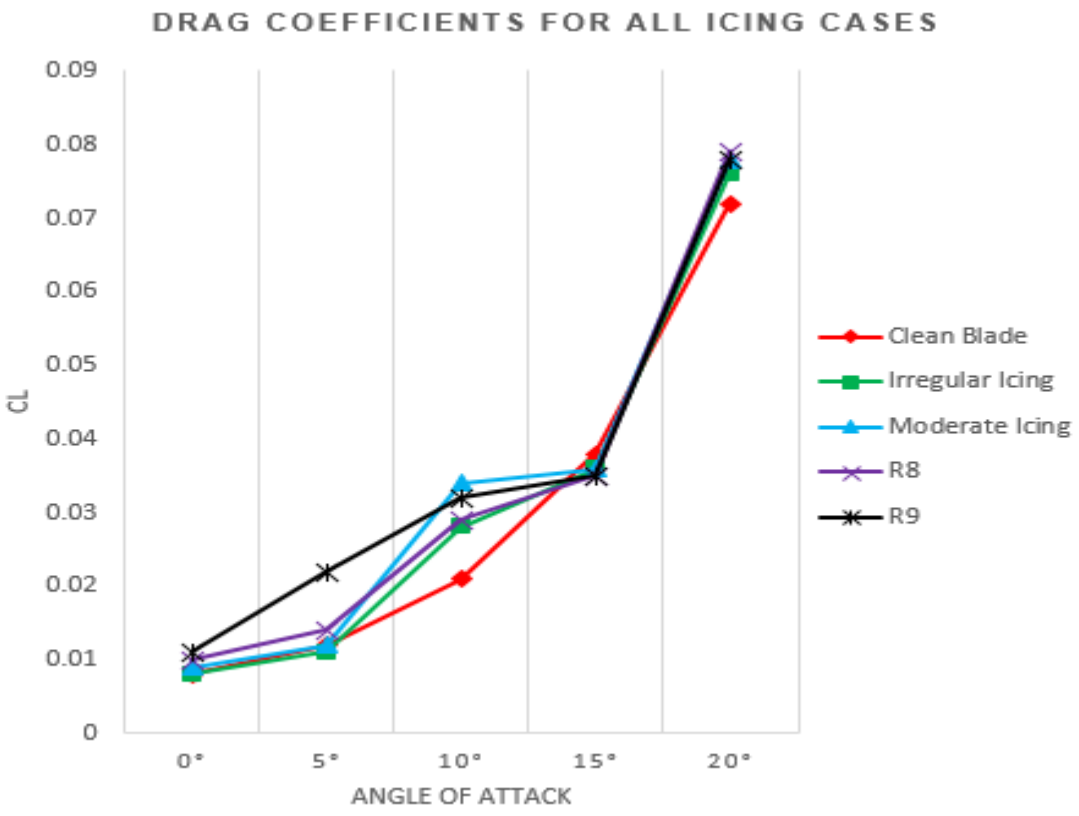

Figure 7.18: Drag cefficients for clean blade and all icing cases

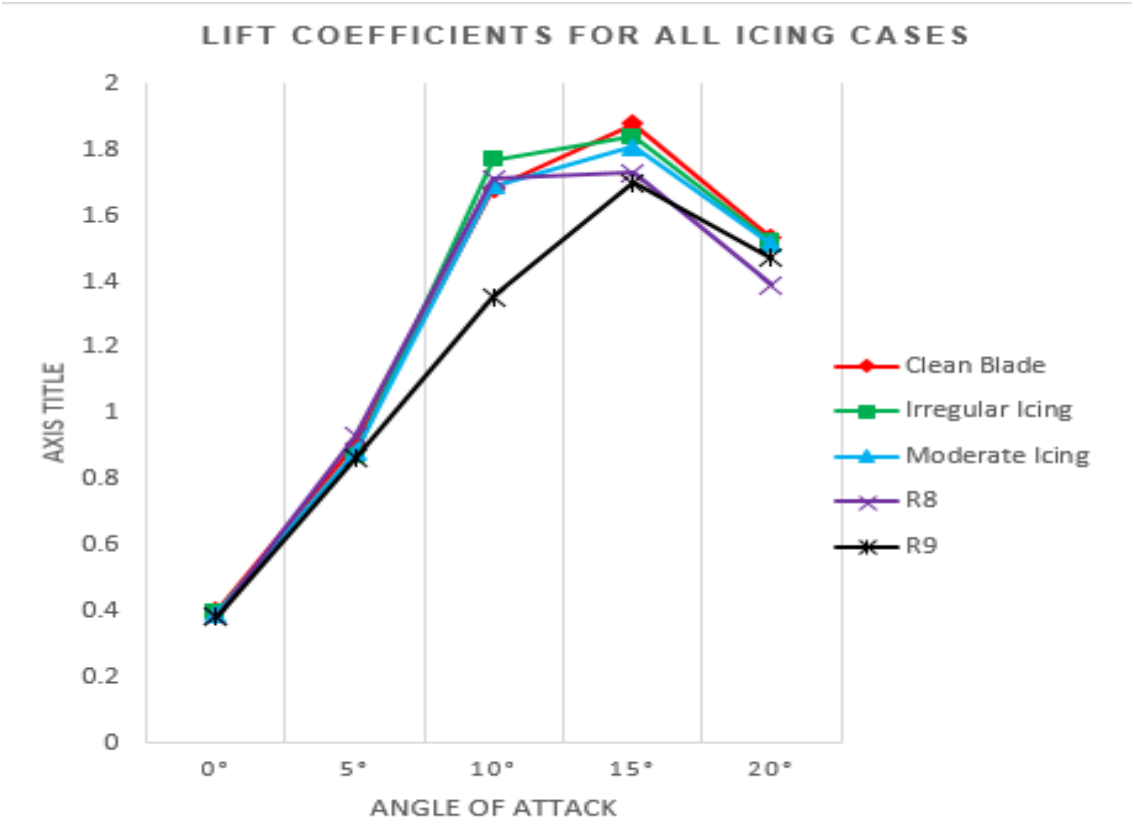

Figure 7.19: Lift cefficients for clean blade and all icing cases

Figure 7.18 shows the drage coefficients for all cases of icing and clean blade case, the clean blade curve lies, as expected, lower than other curves, while the curve of the icing case R9 almost on the top of the curves. The lift coefficients for all icing cases, are illustrated in Figure 7.18, R9 case is lower than all other cases. It is observrd that maximum lift occurs at angle of stall at 15º.

7.5 Effect of Icing on Power Generated By the Wind Turbine

The main goal when designing a wind turbine, is to get the highest possible power output under certain weather conditions. The blade profile, the wind velocity and other weather conditions are curtail aspect to determine the amount of power that a wind turbine can generate.

(Manwell et al., 2009) introduced a model to estimate power generated by ideal wind turbine rotor. The authors proposed a model which is based on a linear momentum theory assuming steady state fluid flow homogenous and incompressible, and uniform thrust over the rotor area.

By applying the conservation of linear momentum to the control volume enclosing the whole system as shown in Figure 7.20, the net force, which is equal and opposite to the thrust, $\underline{T}$, can be determined.

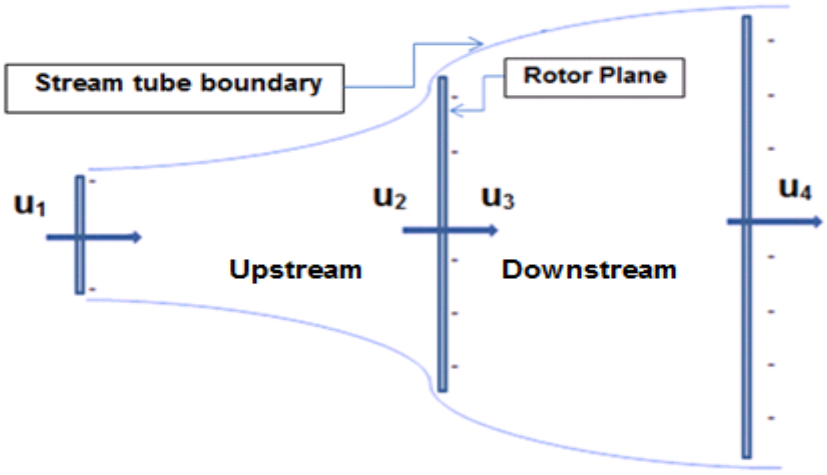

Figure 7.20: Simple model to estimate power generated by ideal wind turbine rotor (Manwell et al., 2009)

For a one-dimensional, incompressible and time-invariant flow and according to the conservation of linear momentum, one may find the thrust which is simply equal and opposite to the rate of change of momentum of the air stream as:

$$\underline{T} = u_1(\rho\, A\, u)_1 - u_4(\rho\, A\, u)_4 \tag{7.4}$$

where ρ is the air density, A is the cross-sectional area, u is the air velocity, and subscripts indicate values for sections illustrated in Figure 7.18. For steady state flow, $(\rho A u)_1 = (\rho A u)_4 = \dot{m},$ where $\dot{m}$ is the air mass flow rate. Therefore the thrust is:

$$\underline{T} = \dot{m}\,(u_1 - u_4) \tag{7.5}$$

The thrust is positive so $u_4 < u_1$. In other words, the air velocity behind the rotor u_4 is less than the free stream velocity u_1. There is no work done on either side of the turbine rotor. So for the two control volumes in both sides of the rotor plane, Bernoulli equation may be applied. To the left of the rotor plane, Bernoulli equation for upstream of the rotor plane is:

$$P_1 + \frac{1}{2}\,\rho\,{u_1}^2 = P_2 + \frac{1}{2}\,\rho\,{u_2}^2 \tag{7.6}$$

where P is the air pressure, and to the right side of the rotor plane, Bernoulli equation for downstream of the rotor plane is:

$$P_3 + \frac{1}{2}\,\rho{u_3}^2 = P_4 + \frac{1}{2}\,\rho{u_4}^2 \tag{7.7}$$

It is important to note that far upstream pressure and far downstream pressure are assumed to be equal and the velocity across rotor plane remains the same which means that ($P_1 = P_4$) and ($u_2 = u_3$).

The thrust is the net sum of the forces on each side of the rotor plane and is given by:

$$\underline{T} = A_2\,(P_2 - P_3) \tag{7.8}$$

Solving for $(P_2 - P_3)$ using equations (7.6) and (7.7) and substituting in equation (7.8) yields:

$$\underline{T} = \frac{1}{2}\,\rho A_2\,({u_1}^2 - {u_4}^2) \tag{7.9}$$

By equating values of thrust for equations (7.8) and (7.9) and knowing that the air mass flow rate remains ($\rho A_2 u_2$), one obtains:

$$u_2 = (u_1 + u_4)/2 \tag{7.10}$$

The wind velocity at the rotor plane is simply the average of the upstream and downstream wind speeds. The power output, $\mathbb{P}$, is equal the thrust multiplied by the velocity at the rotor plane:

$$\mathbb{P} = \frac{1}{2}\,\rho A_2 ({u_1}^2 - {u_4}^2) \times u_2 \tag{7.11}$$

7.5.1 Power Reduction Due To Moderate Icing Scenario

Figure 7.21 illustrates a 5-MW (DU21) aerofoil in CFD domain at 0º (AOA) for both the clean and the assumed moderate icing scenario. The inlet wind stream velocity was assumed to be u_1= 10 m/s for all cases.

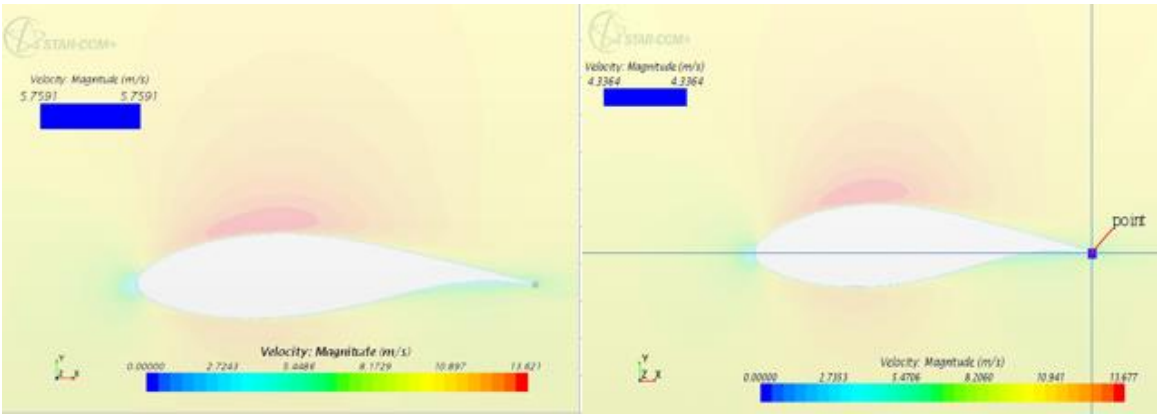

Figure 7.21: Velocity at trailing edge for (DU21) airfoil for 0º (AOA), clean profile to the right and moderately iced to the left

The outlet stream velocity was measured at the trailing edge of the aerofoil, which for this case is u_4= 4.3 m/s. The velocity at different locations of the aerofoil can be measure by the use of STAR-CCM+. According to equation (7.10) the intermediate velocity u_2 is the average of the inlet and outlet velocities, i.e., u_1 and u_4 respectively. The velocity at the trailing edge for the moderate iced profile has increased to 5.8 m/s which mean less power being generated.

By assuming air temperature -10 ºC the air density was given in Chapter 6 as 1.26 kg/m^3. The reference velocity and the area for 5-MW (DU21) aerofoil were estimated by (Homola et al., 2012) to be 50.7 m/s and 1.35 m^2, respectively.

Moreover, according to the Betz limit, the maximum amount of power that can be extracted from a wind turbine is approximately 59% (Light and Robinson, 2003). This means that no wind turbine is capable to convert more than 59% of the kinetic energy of the wind into mechanical energy, thus equation (7.11) will be modified as:

$$\mathbb{P} = 0.6 \times \frac{1}{2}\, \rho A_2 ({u_1}^2 - {u_4}^2) \times u_2 \qquad (7.12)$$

The generated power for clean and moderately iced aerofoil may be calculated as follows:

$$\mathbb{P}_{Clean} = 0.6 \times \frac{1}{2} \times 1.26 \times\ 1.35\ \left(10^2 - 4.3^2\right) \times 7.2 = 279.8\ \text{W} \qquad (7.13)$$

$$\mathbb{P}_{Iced} = 0.6 \times \frac{1}{2} \times 1.26 \times\ 1.35\ \left(10^2 - 5.8^2\right) \times 7.64 = 265.1\ \text{W} \qquad (7.14)$$

Hence, for the case of moderately iced airfoil, a reduction of the generated power by 9.7% was observed.

The same procedure is repeated to calculate the results under all other angles of attack (AOA). Velocities for different (AOA) for clean and moderately iced profile are shown in Figure 7.22.

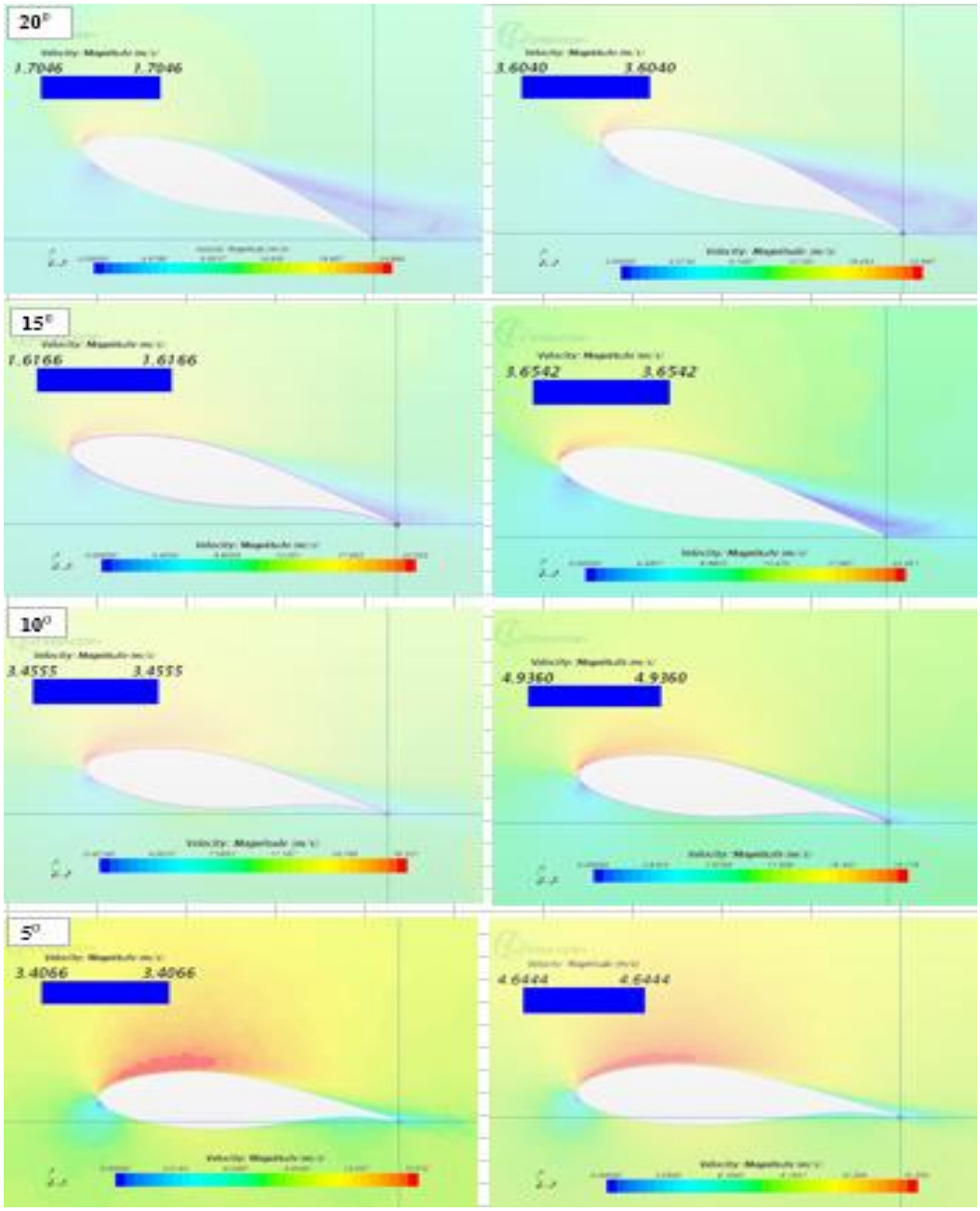

Figure 7.22: Velocities at trailing edge for (DU21) airfoil at different (AOA), clean profile to the left and moderately iced to the right

Table 7.8 summarizes the power generation results of the 5-MW (DU21) under a moderate icing scenario and the comparison to a clean blade case.

Table 7.8: Power generated for moderate icing scenario and clean 5-MW (DU21) aerofoil

AOA	Moderate icing scenario			Clean airfoil			Power reduction Percent
	u_4 m/s	u_2 m/s	Power ($\mathbb{P}$) $\bar{w}$ (Watt)	u_4 m/s	u_2 m/s	Power ($\mathbb{P}$) $\bar{w}$ (Watt)	
0º	5.8	7.9	268.5	4.3	7.2	297.2	9.7%
5º	6.7	7.9	235.9	3.4	6.7	302.2	21.2%
10º	7.0	8.5	221.7	3.5	6.7	302.1	26.6%
15º	7.6	8.8	189.6	6.0	8.0	260.1	27.1%
20º	8.1	9.0	160.0	6.3	8.1	251.0	36.0%

The velocity at the trailing edge of the aerofoil is found to be less for clean airfoil profile and more for the same iced aerofoil profile. This is due to the change in the aerodynamic behaviour of incoming airstream around the airfoil because of the change in the geometry of airfoil profile. Instead of smooth moving of airstream around the clean aerofoil profile, the accreted ice is presenting geometrical obstacle and leads to local distortions within the incoming airstream. Figure 7.23 gathered different arrangements for airstream velocity at trailing edge of clean aerofoil, moderately and heavy iced aerofoils profile under various (AOA). The Figure shows that ice accretion has changed the profile of the aerofoil leads to dislocation of the separation point for the flow over the top of the aerofoil, hence earlier flow separation.

Results show reductions in the generated power due to moderate icing on the aerofoil profile. The power reduction has increased with the increase of the (AOA). This is primarily due to the fact that the incoming airflow separation point is moving opposite to the direction of the airflow as the (AOA) increases as shown in Figure 7.23. This will reduce lift and increase drag, leading to more power reduction. With

the existence of accreted ice on the leading edge, the incoming airflow separation point will move left further to facilitate earlier flow separation and introduce more drag and less lift, as severity of icing and (AOA) are increasing and consequently cause more reduction in the generated power of the wind turbine.

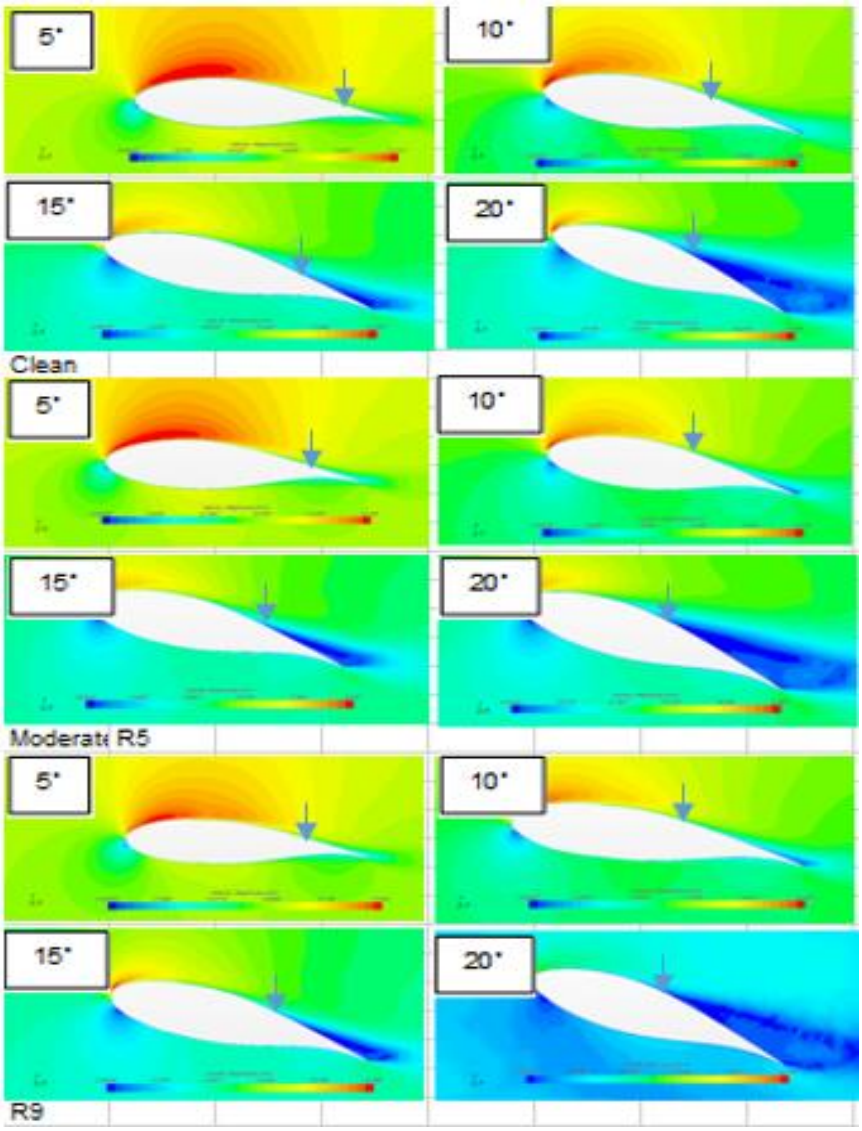

Figure 7.23: Airflow separation point moving left for moderate iced and R9 aerofoils as compared to clean aerofoil for different (AOA).

7.5.2 Power Reduction Due To the Heavy Icing Scenario R8

In this icing scenario, the thickness of ice at the leading edge of airfoil profile has increased to 59 mm. Due to the increase of thickness the shape of the aerofoil profile experiences more change. This will encourage earlier separation in the boundary layer resulting in lift force loss. Hence, less power will be generated in the presence of more accreted ice.

Same method for power calculation was followed up to get the generated power for both iced and clean aerofoil profiles under different (AOA) values. Table 7.9 summarizes the results for heavy icing case R8.

Table 7.9: Power generated for heavy icing scenario R8 and clean (DU21) airfoil

AOA	R8 icing scenario			Clean aerofoil			Power reduction Percent.
	u_4 m/s	u_2 m/s	Power ($\mathbb{P}$) $\bar{w}$ (Watt)	u_4 m/s	u_2 m/s	Power ($\mathbb{P}$) $\bar{w}$ (Watt)	
0º	6.2	8.1	254.3	4.3	7.2	297.2	14.4%
5º	6.8	8.4	230.3	3.4	6.7	302.2	23.8%
10º	7.5	8.7	198.0	3.5	6.7	302.1	34.5%
15º	8.1	9.0	160.0	6.0	8.0	260.1	38.5%
20º	8.8	9.4	108.2	6.3	8.1	251.0	56.9%

It can be seen from the results in Table 7.9 that the power reduction is greater under R8 icing condition as compared to the previous moderate icing case. This is expected as the ice thickness has increased creating more change to the original aerofoil profile shape. It will affect lift force generation by displacing the path of airflow which supposed to be aligned to airfoil original profile. As the aerofoil increases its angle of attack, airflow can no longer flow smoothly over the aerofoil,

causing the aerofoil to stall. Icing problem will added to this, causing more losses to the lift and encouraging more drag and hence, more power reduction.

7.5.3 Power Reduction Due To the Heavy Icing Scenario R9

The third case deals with heavy icing scenario R9. The ice thickness on the leading edge of the aerofoil has increased to a value 105.4 mm as given in Table 7.5. As the aerofoil profile is subjected to more change to its original shape, more power loss is expected due to further changing in the airflow stream lines. Results of power loss under icing scenario R9 are given in Table 7.10.

Table 7.10: Power generated for heavy icing scenario R9 and clean (DU21) aerofoil

AOA	R9 icing scenario			Clean airfoil			Power reduction Percent.
	u_4 m/s	u_2 m/s	Power ($\mathbb{P}$) $\bar{w}$ (Watt)	u_4 m/s	u_2 m/s	Power ($\mathbb{P}$) $\bar{w}$ (Watt)	
0º	6.5	8.3	243.0	4.3	7.2	297.2	18.2%
5º	7.3	8.7	206.1	3.4	6.7	302.2	31.8%
10º	7.9	9.0	221.7	3.5	6.7	302.1	43.2%
15º	8.5	9.3	131.6	6.0	8.0	260.1	49.4%
20º	10.1	10.0	-1.0	6.3	8.1	251.0	250%

The R9 assumed icing scenario represents a heavy icing case. Results show greater power loss as compared to the previous two cases. The aerofoil lost about half of its generated power at the (AOA) of 15º. The aerofoil stalls at the angle of attack of 20º and loses its capacity of power generation as it's no longer able to produce lift due to the excessive ice accretion.

7.5.4 Power Reduction Due To the Irregular Icing Profile of the 5-MW (DU21) Section

The last case of the 5-MW (DU21) section is the irregular icing profile, results are given in Table7.11

Table 7.11: Power generated for irregular icing profile and clean (DU21) aerofoil

AOA	Irregular Icing Profile			Clean airfoil			Power reduction Percent
	u_4 m/s	u_2 m/s	Power ($\mathbb{P}$) $\bar{w}$ (Watt)	u_4 m/s	u_2 m/s	Power ($\mathbb{P}$) $\bar{w}$ (Watt)	
0º	5.6	7.8	273.2	4.3	7.2	297.2	8.1%
5º	6.1	7.9	253.1	3.4	6.7	302.2	16.2%
10º	6.8	9.0	246.9	3.5	6.7	302.1	18.2%
15º	7.5	9.3	207.6	6.0	8.0	260.1	201.%
20º	8.1	9.3	163.2	6.3	8.1	251.0	34.9%

The generated power for all cases is illustrated in Figure 7.24

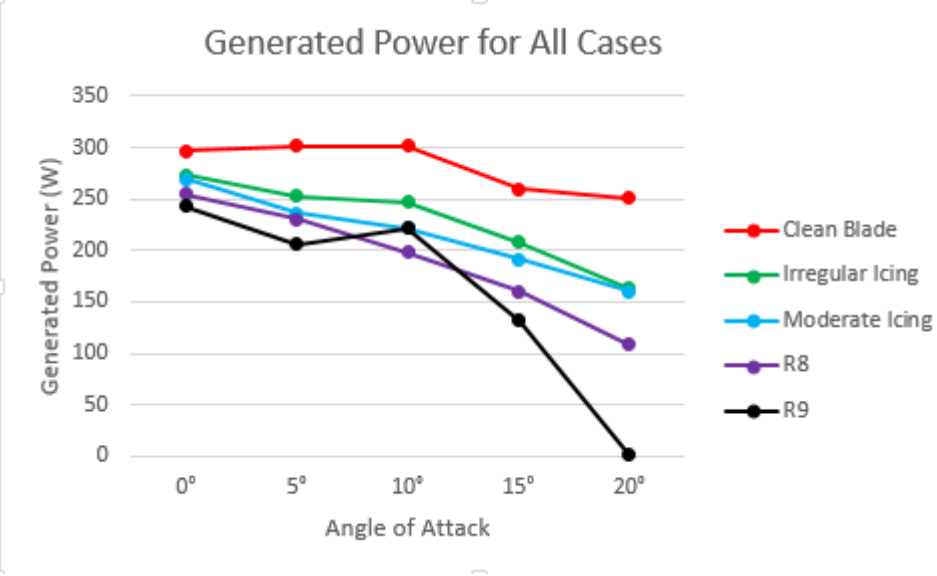

Figure 7.24: Generated power in the 5-MW (DU21) aerofoil due to applying all icing cases compared to clean aerofoil

As illustrated in Figure 7.24, the clean blade has gained the maximum generated power, and then the case of irregular icing then moderate icing. Heavy icing cases R8 and R9 have obtained lower generated power. Power for all cases dropped after stall (AOA). It is linked to the increase of the distortion vortices over the top of the airfoil leading to an increase in the drag force. It's worthwhile to mention that it was expected that the case of irregular icing profile has less generated power as compared to the moderate case but because the simulation for the irregular icing profile was just for one hour it gained more power than the case of the moderate icing as all assumed icing scenarios including the moderate case are based on longer icing events. Figure 7.25 shows the percentage of power reduction for the all icing cases with the heavy icing R9 having the highest power reduction.

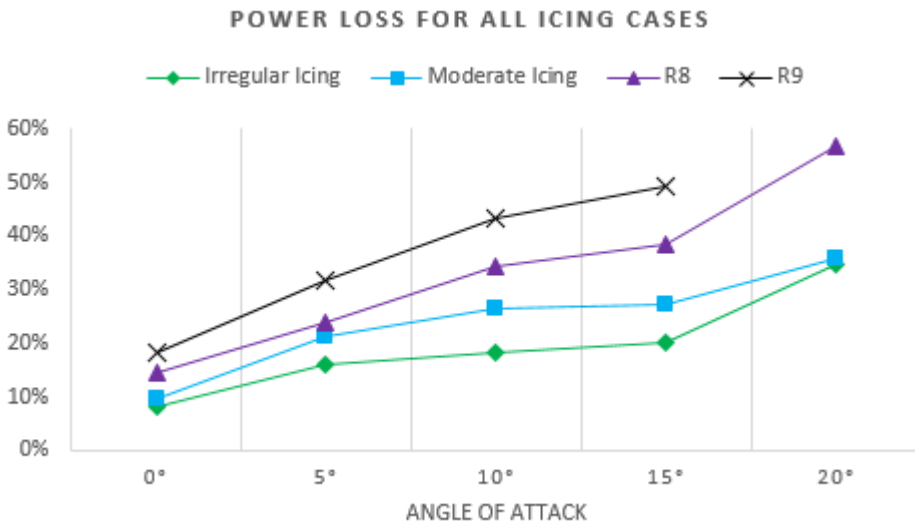

Figure 7.25: Power reduction percentage in the 5-MW (DU21) airfoil due to applying different icing cases

This may shed a light that, besides the danger of vibrations to the structural integrity of the wind turbine, it is useless to allow the wind turbine working under severe atmospheric icing conditions, especially with high angles of attack which

cannot be avoided with the continuous change of airflow direction (Busch et al., 2008).

7.6 Effects of Icing on the Aerodynamic Behaviour and Power Generation of 1-MW Aerofoil Profile

In this section, the effect of atmospheric icing on the aerodynamic performance of a typical 1-MW aerofoil will be investigated.

7.6.1 The Drag and Lift Force Coefficients for 1-MW (NACA 63417) Aerofoil

The profiles of clean and typically moderately R5 iced 1-MW aerofoil are illustrated in Figure 7.26. The aerofoil (NACA 63417) cross-sectional area and relative velocity are 0.270 m^2 and 57.75 m/s, respectively (Homola et al., 2009).

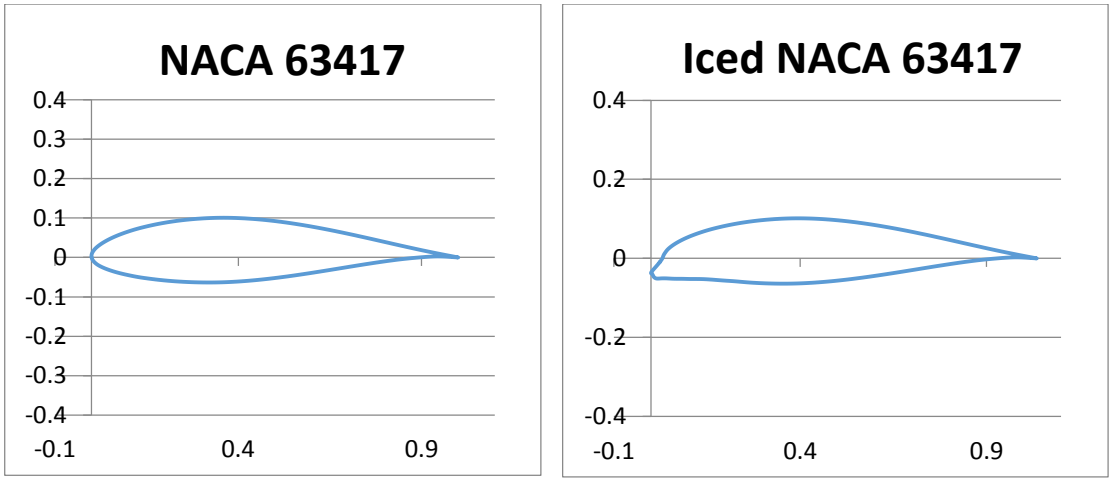

Figure 7.26: Clean and iced 1-MW (NACA 63417) aerofoil profiles, clean to the left and typically iced (R5) to the right

Numerical setup for 1-MW aerofoil profile is almost the same as what was explained earlier for the 5-MW aerofoil profile in previous sections except that the CFD boundary domain is smaller due to smaller chord length. The physical properties and mesh scheme remain the same.

The 1-MW (NACA 63417) aerofoil profile has an cross sectional area of 0.20 m^2 ,relative velocity of 53.9 m/s, and chord length of 1 m (Homola et al., 2009). Drag and lift coefficients are numerically calculated for (AOA) 0º, 5º, 10º, 15º, and 20º using STAR-CCM+. Results are summarised in Table 7.12.

Table 7.12: Drag and lift coefficients for iced and clean 1-MW (NACA 63417) aerofoil

AOA	Case	C_D	C_L
0º	Clean	0.012	0.24
	Iced	0.014	0.22
5 º	Clean	0.017	0.67
	Iced	0.015	0.54
10 º	Clean	0.030	1.06
	Iced	0.032	1.02
15 º	Clean	0.073	1.05
	Iced	0.075	1.05
20 º	Clean	0.161	0.90
	Iced	0.133	1.04

It can be seen from Table 7.12 that drag coefficients are increased due to icing and the increase of (AOA). For each (AOA), the drag coefficient increases due to atmospheric icing on the leading edge of the aerofoil profile causing unfavourable change in the stream lines of the incoming flow. Lift coefficients are decreasing due to icing till stall happens at about 15 degrees, as illustrated in Figure 7.27. Drag coefficients for the same aerofoil are shown in Figure 7.28, the iced aerofoil has more drag values as compared to the clean one until the stalling (AOA) then has less values after that.

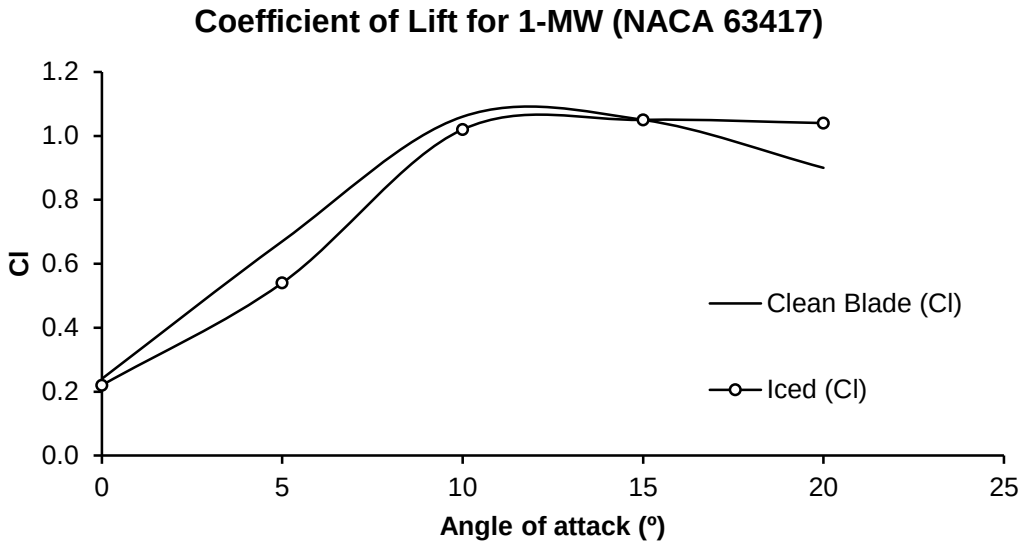

Figure 7.27: Lift coefficeints for clean and iced 1-MW (NACA 63417) aerofoil profile

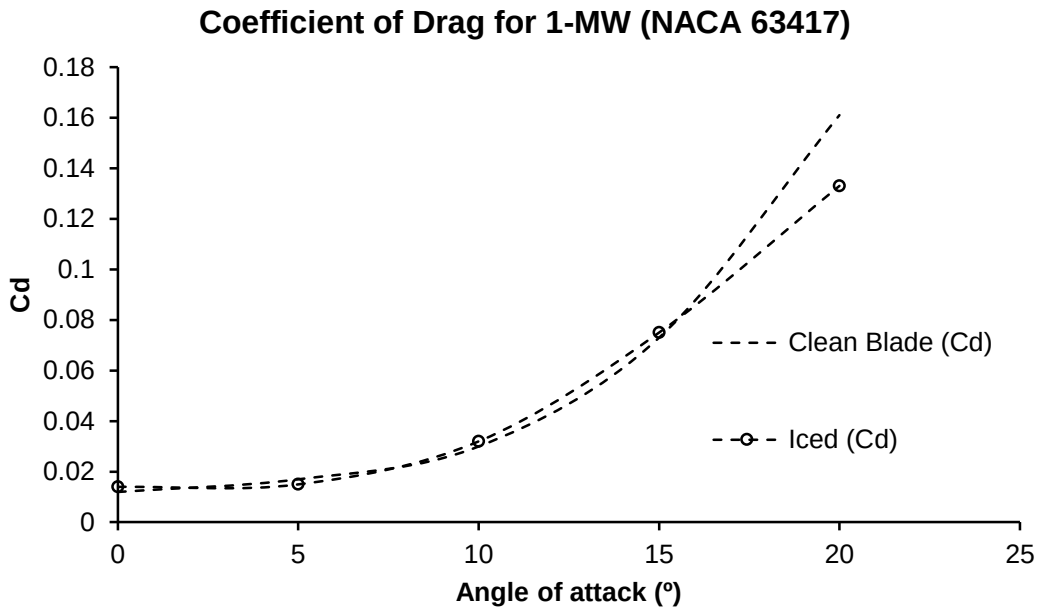

Figure 7.28: Drag coefficeints for clean and typically iced 1-MW (NACA 63417) aerofoil profile

7.6.2 Generated Power Losses Due To Typical Icing of 1-MW Aerofoil Profile

The generated power for 1-MW wind turbine aerofoil is calculated using the same method explained in previous sections. With the existence of ice on the leading

edge, there will be a reduction in the velocity drop due to change of stream lines of the incoming airflow causing earlier and larger flow separation over the top of the aerofoil and power reduction. Results of generated power for clean and iced aerofoils are given in Table 7.13.

Table 7.13: Power loss due to icing for the 1-MW (NACA 63417) aerofoil

AOA	**Iced aerofoil**			**Clean aerofoil**			**Power reduction Percent.**
	u_4 m/s	u_2 m/s	Power ($\mathbb{P}$) $\bar{w}$ (Watt)	u_4 m/s	u_2 m/s	Power ($\mathbb{P}$) $\bar{w}$ (Watt)	
0º	6.4	8.2	49.4	5.9	8.0	53.2	7.1%
5º	6.9	8.5	45.5	6.2	8.1	50.9	11.9%
10º	8.6	9.3	24.7	7.6	8.8	38.0	35.0%
15º	9.0	9.5	18.4	8.1	9.1	32.0	42.4%
20º	9.6	9.8	7.8	7.6	8.8	38.0	79.5%

Figure 7.29 shows the power reduction of the of the iced 1-MW (NACA 63417) aerofoil as function of the angle of attack of the incoming air stream, the power reduction has increased as the angle of attack increases due to the increase of distortion vortices near the boundary layer of the upper side of the aerofoil leading to more decrease in the lift and increase in the drag and hence more power

reduction.

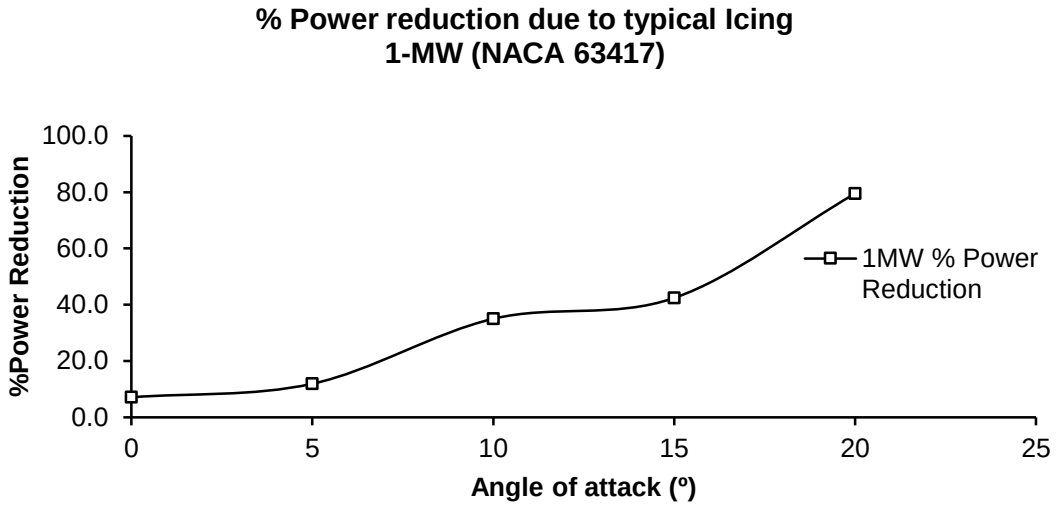

Figure 7.29: Power reduction percentage due to typical icing on 1-MW (NACA 63416) aerofoil profile

7.7 Summary

This Chapter deals with the effect of atmospheric ice accretion on the aerodynamic performance of typical 5-MW and 1-MW aerofoils. STAR-CCM+ was chosen to perform the CFD analysis. Aerofoil geometries, boundary conditions, and mesh specifications were presented. Mesh diagnostics report provided by the Software record stated that both volume and 2D mesh were in excellent conditions. Coefficients for drag and lift were obtained for both the clean and the iced aerofoil profiles. Power losses of the 5-MW blade due to the three assumed icing scenarios along with a case of irregular icing were investigated, showing greater power loss for heavy icing cases. It is found that the 1-MW blade aerofoil profile has experienced relatively greater power loss compared with those of the 5-MW case as the smaller size of the 1-MW aerofoil tends to collect more ice on its leading edge in terms of percentage.

CHAPTER EIGHT

CONCLUSIONS AND FUTURE WORK

8.1 Conclusions

Atmospheric icing presents serious challenges to the wind energy industry in cold regions in terms of its potential detrimental impact on the safe operation and the energy harvest of the wind turbine. A further understanding of the effect of atmospheric ice accretion on the structural integrity and aerodynamic performance of wind turbine blades is required to address the challenges facing the industry. This thesis presents a systematic numerical study on icing profiles under different weather conditions and their impact on natural frequency, fatigue life, and lift/drag and power generation of wind turbines. Following conclusions can be drawn based on the research in this project:

While many researchers have investigated the vibrational behaviour of wind turbines due to the aerodynamic effect, little attention has been paid to the research of the effect of atmospheric ice accretion on the dynamic performance of wind turbines. The potential detrimental impact of atmospheric icing on the safe operation of wind turbines and the energy harvest hasn't been fully understood and requires further investigation.

A method to estimate icing mass and profile under different weather conditions has been developed. Three icing scenarios have been identified according to the ISO Standard and the corresponding icing profiles have been established for the 5-MW wind turbine blade and its rotor to investigate their influence on vibrational behaviours of the wind turbine blade and the rotor.

Atmospheric ice accretion will drive natural frequencies of the wind turbine down to the near resonance limit, which could lead to significant issues on structural

integrity of the wind turbine. The moderate icing scenario showed a small reduction of about 4% - 5% in the first three natural frequencies of the non-rotating system. No change was observed for the first and the third modes in the rotating system, which was attributed to the centrifugal stiffness of the blade during rotation. For icing scenario R8, the reduction for the first vibration mode was 17% and 19% for the second and third mode and for the non-rotating case and from 12% to 15% for the rotating case. As for the severe icing scenario R9, natural frequencies were dropped even further. The reduction was 24% for the first and second modes and 25% for the third vibration mode for the non-rotating case and 19% to 22% for the rotating case.

The effect of atmospheric ice accretion on the fatigue life of the wind turbine blade has been investigated for heavy icing scenario R8 and for two different wind velocities. Significant reduction of fatigue life was found due to the increase in the von Mises stresses and the dynamic magnification factor under the three assumed icing loads.

CFD simulation has been carried out to investigate the effect of atmospheric ice accretion on the aerodynamic performance of typical 1-MW and 5-MW wind turbine blades. Results of the drag and lift coefficients and power production under different icing scenarios and an irregular icing profile were obtained for five angles of attack. Compared with the results of the clean aerofoil profile, remarkable reduction in the power generation due to the accreted ice was observed at various aerofoil sections in the spanwise direction of the blade. It is found that ice accretion leads to a dislocation of the separation point and hence promotes earlier flow separation, leading to an increase in drag and a decrease in lift and consequently a reduction in the generated power. The detrimental

impact of atmospheric icing on energy harvest has been demonstrated for the wind energy industry.

8.2 Future Work

Based on the research of this project, following work are recommended for further study of the effect of excessive icing on the dynamic performance of wind turbines:

- Carry out the research for the complete wind turbine system. The inclusion of the mast and the nacelle will add a more elaborated understanding on the impact of ice accretion on the dynamics performance of the wind turbine.

- Conduct an experimental study to compare and validate numerical results in this project. Vibration test and wind tunnel test should be carried out using suitable wind turbine blade prototype with and without the icing profile.

- Carry out a 3D CFD analysis for the whole blade to obtain more accurate data on the effect of atmospheric ice accretion on the aerodynamic performance of the wind turbine blade.

- Carry out an in-depth fluid-structural interaction analysis for the iced wind turbine and develop a further understanding of the effect of unbalanced ice accretion on the dynamic performance of the wind turbine.

References

AHLSTRöM, A. 2005. *Aeroelastic Simulation of Wind Turbine Dynamics.* PhD, Royal Institute of Technology.

AHTI, K. & MAKKONEN, L. 1982. Observations on rime formation in relation to routinely measured meteorological parameters. *Geophysica,* 19**,** 75-85.

ALBISSER, P. 2009. Adhesives for Bonding Wind Turbine Blades *Reinforced Plastics,* 9**,** 26-29.

ANDERSEN, E., BöRJESSON, E., VAINIONPää, P. & UNDEM, L., S. 2011. Wind Power in cold climate. *In:* ENVIRONMENTAL, W. (ed.) *Nordic Energy Research.* Oslo, Norway.

ANTIKAINEN P., P. S., T., L. & E., P. 2003. Modeling, verification and classification of ice loads in wind turbines. *In:* VI, B. (ed.). Pyhätunturi, Finland.

ARRIGAN, J., PAKRASHI, V., BASU, B. & NAGARAJAIAH, S. 2011a. Control of flapwise vibrations in wind turbine blades using semi-active tuned mass dampers. *Structural Control and Health Monitoring,* 18**,** 840–851.

ARRIGAN, J., PAKRASHI, V., BASU, B. & NAGARAJAIAH, S. 2011b. Control of flapwise vibrations in wind turbine blades using semiactive tuned mass dampers. *Structural Control and Health Monitoring,* 18**,** 1-38.

ATTAF, B. Vibrational analyses of fibre-reinforced composite wind turbine blades. *In:* EFEEA, ed. International Symposium on Environment Friendly Energies in Electrical Applications, 2010 Ghardaïa, Algeria. 1-8.

ATTARNEJAD, R., MANAVI, N. & FARSAD, A. 2006. Exact Solution for The Free Vibration of A Tapered Beam With Elastic End Rotational Restraints. *Computational Methods***,** 1993–2003.

BARANOWSKI, S. & LIEBERSBACH, J. 1978. The intensity of different kinds of rime on the upper tree line in the Sudety Mountains. *Journal of Glaciology,* 19**,** 489-497.

BARCLAY, C. 2012. Wind Farms - Distance from housing. *In:* SN/SC/5221, S. N. (ed.). England.

BAZILEVS, Y., HSU, M.-C., AKKERMAN, I., WRIGHT, S., TAKIZAWA, K., HENICKE, B., SPIELMAN, T. & TEZDUYAR, T., E. 2010. 3D Simulation of Wind Turbine Rotors at Full Scale. Part I: Geometry Modelling and Aerodynamics. *INTERNATIONAL JOURNAL FOR NUMERICAL METHODS IN FLUIDS,* 2010**,** 1-29.

BAZOUNE, A. 2007. Effect of Tapering on Natural Frequencies of Rotating Beams. *Shock and Vibration,* 14**,** 169-179.

BAZOUNE, A. & KHULIEF, Y., A. 1992. A FINITE BEAM ELEMENT FOR VIBRATION ANALYSIS OF ROTATING TAPERED TIMOSHENKO BEAMS. *Journal of Sound and Vibration,* 156**,** 141-164.

BECHLY, M., E. & CLAUSEN, P., D. 1997. Structural Design of a Composite Wind Turbine Blade Using Finite Element Analysis. *J. of Computers and Structures,* 63**,** 639-646.

BERTIN, J. J. & SMITH, M. L. 1998. Aerodynamics for engineers.

BERZERI, M. & SHABANA, A. A. 1999. A finite element study of the geometric centrifugal stiffening effect. DTIC Document.

BIGGS, J., M. 1964. *Structural Dynamics,* USA.

BIR, G. & MIGLIORE, P. 2004. Preliminary Structural Design of Composite Blades for Two- and Three-Blade Rotors. *In:* NREL (ed.) *WER4.3303.* Golden, Colorado, USA.

BONNET, P., A. , AND DUTTON, G. Parametric Modelling Of Large Wind Turbine Blades. Abaqus UK Regional User Meeting, 2007 UK. 211-225.

BORTOLOTTI, P. 2012. *Carbon Glass Hybrid Materials for Wind Turbine Rotor Blades.* MSc, Delft University of Technology.

BOSE, N. 1992. Icing on a small horizontal-axis wind turbine-Part 1: Glazing profiles. *Journal of Wing Engineering and Industrial Aerodynamics,* 45**,** 75-85.

BOTTA, G., CAVALIERE, M. & HOLTTINEN, H. Ice Accretion at Acqua Spruzza and its Effects on Wind Turbine Operation and Loss of Energy Production BOREAS IV, 1998 FMI, Hetta, Finland. 77-86.

BRØNDSTED, P., LILHOLT, H. & LYSTRUP, A. 2005. Composite materials for wind power turbine blades. *Annu. Rev. Mater. Res.,* 35**,** 505-538.

BUDYNAS, R. G. & NISBETT, J. K. 2006. *Shigley's Mechanical Engineering Design*.

BURTON, T., JENKINS, N., SHARPE, D. & BOSSANYI, E. 2011. *Wind Energy Handbook*.

BUSCH, G. T., BROEREN, A. P. & BRAGG, M. B. 2008. Aerodynamic simulation of a horn-ice accretion on a subscale model. *Journal of Aircraft,* 45**,** 604-613.

CARLSSON, V. 2011. *Measuring routines of ice accretion for Wind Turbine applications-The correlation of production losses and detection of ice.* MSc, Skellefteå Kraft AB.

CHEN, C.-L. & L-W., C. 2001. Random Response of a Rotating Composite Blade with Flexure-Torsion Coupling Effect by the Finite Element Method *Composite Structures,* 54.

CHEN, L.-W. & PENG, W.-K. 1995. Dynamic Stability of Rotating Blades With Geometric Non-Linearity. *Journal of Sound and Vibration,* 187 421-433.

CHEN, L., -W. & KU, D.-., M. 1990. Dynamic Stability Analysis of a Rotating Shaft By the Finite Element Method. *Journal of Sound and Vibration,* 143**,** 143-151.

CHEN, Y.-P. 2011. *A STUDY OF THE AERODYNAMIC BEHAVIOUR OF A NREL PHASE VI WIND TURBINE USING THE CFD METHODOLOGY* MSc, Wright State University.

CHOUDHRY, A., MO, J., ARJOMANDI, M. & KELSO, R. Effects of Spacing between Wind Turbines on Blade Dynamic Stall. 18th Australasian Fluid Mechanics Conference, 3-7 December 2012 2012 Launceston, Australia.

COBBLE, M., H. & FANG, P., C. 1976. Finite Transformation Solution of the Damped Cantilever Beam Equation Having Distributed Load, Elastic Support, and the Wall Edge Elastically restrained Against Rotation. *Journal of Sound and Vibration,* 6**,** 187-198.

COLBY, D. 2008. The Health Impact of Wind Turbines: A Review of the Current White, Grey, and Published Literature. *In:* UNIT, C.-K. P. H. (ed.). Chatham Ontario, Canda.

CORUM, J. M., BATTISTE, R. L., LIU, K. C. & RUGGLES, M. B. 2000. Basic Properties of Reference Crossply Carbon-Fiber Composite. *In:* LABORATORY, O. R. N. (ed.) *LOCKHEED MARTIN ENERGY RESEARCH CORP.* Oak Ridge, Tennessee, USA U.S. DEPARTMENT OF ENERGY.

DALILI, N., EDRISY, A. & CARRIVEAU, R. 2009. A review of surface engineering issues critical to wind turbine performance. *Renewable and Sustainable Energy Reviews,* 13**,** 428–438.

DAS, S., K., RAYB, P., C. & POHIT, G. 2007. Free Vibration Analysis of a Rotating Beam With Non-linear Spring and Mass System. *Journal of Sound and Vibration,* 301**,** 165-188.

DE-JIN, H., HAO-JIANG, D. & WEI-QIU, C. 2007. Analytical solution for functionally graded anisotropic cantilever beam subjected to linearly distributed load. *Applied Mathematics and Mechanics,* 28**,** 855-860.

DOBESCH, H. & NIKOLOV, D. Icing measurements and model results from Oberstrahlbach, Austria. Proceedings of the 2005 BOREAS VII, 2005 Saariselkä, Finland.

DOBESCH, H. E. A. 2005. Physical processes, modelling, and measuring of icing effects in Europe. *In:* ENERGY, E. A. S. D. Ö. B. Z. M. U. G. Z. F. M. U. G. N. (ed.). Vienna, Austria: EU, contract NNE5/2001/259.

DUNNE, F., SCHLIPF, D. & PAO, L., Y. 2012. Comparison of Two Independent LIDAR-Based Pitch Control Designs. *In:* LABORATORY, N. R. E. (ed.). Golden, Colorado, USA.

DUTTA, P., K. & HUI, D. Effects of Cold Regions Environment on Structural Composites *In:* ENGINEERS, J. S. O. M., ed. Proceedings of the International Conference on Advanced Technology in Experimental Mechanics, 1997.

ELGER, D. F., WILLIAMS, B. C., CROWE, C. T. & ROBERSON, J. A. 2014. *Engineering fluid mechanics*, Wiley.

ESWARARAO, A., VSJ 2012. Comparison of Experimental Results With CFD For NREL Phase VI Rotor With Tip Plate PRESS. *INTERNATIONAL JOURNAL of RENEWABLE ENERGY RESEARCH,* 2**,** 1-8.

EWINS, D. 2003. Modal testing: theory, practice and application (mechanical engineering research studies: engineering dynamics series).

FALKOVICH, G. 2011. *Fluid mechanics: A short course for physicists*, Cambridge University Press.

FARINHOLT, K., M., TAYLOR, S., G., PARK, G. & AMMERMAN, C., M. Full-scale fatigue tests of CX-100 wind turbine blades. Part I: testing. *In:* GRIFFIN, K. F. A. S. F., ed. Industrial and Commercial Applications of Smart Structures Technologies 2012 San Diego, California, March 11, 2012.

FAY, G. 2001. Derivation of the aerodynamic forces for the mesicopter simulation. *Standord University. Stanford, CA*.

FORTIN, G., PERRON, J. & ILINCA, A. A Study of Icing Events at Murdochville: Conclusions for the Wind Power Industry, International Symposium Wind Energy in Remote Regions, October 2005 2005 Magdalen's Island, Canada.

FROHBOESE, P. & ANDERS, A. 2007a. Effects of Icing on Wind Turbine Fatigue Loads. *Journal of Physics: Conference Series,* 75, 012061.

FROHBOESE, P. & ANDERS, A. 2007b. Effects of Icing on Wind Turbine Fatigue Loads. *Conference Series 75.2007, Journal of Physics.,* 75.

FU, P. & FARZANEH, M. 2010. A CFD Approach for Modeling the Rime-Ice Accretion Process on a Horizontal-Axis Wind Turbine. *J. Wind Eng. Ind. Aerodyn.,* 98**,** 181–188.

FU, P., FARZANEH, M. & BOUCHARD, G. 2006. Two-dimensional modelling of the ice accretion process on transmission line wire sand cables. *Cold Regions Science and Technology,* 46**,** 132–146.

FUERLE, F., SIENZ, J., MOWBRAY, K. & WALKLETT, M. Optimum Blade Design for a Novel Wind Turbine. 2nd International Conference on Engineering Optimization, 2010 Lisbon, Portugal

GADAWSKI, A. & LYNCH, G. 2011. The Real Truth About Wind Energy, A Literature Review on Wind Turbines in Ontario. *In:* INTERNS, S. C. C. (ed.). Ottawa, Canada.

GALLARDO, P., A., L. . 2011. *Static and Fatigue Analysis of Wind Turbine Blades Subject to Cold Weather Conditions Using Finite Element Analysis.* MSc, University of Victoria.

GHAYOURA, R., GHAYOURA, M. & ZIAEI-RADA, S. 2010. Vibration Analysis of Tapered Rotating Composite Beams Using The Hierarchical Finite Element. *Applied and Computational Mechanics,* 4 157-170.

GL, T. R. 2000. Technical Note: IEC 1400-1 GL Test Regulation.

GOODWIN, T. J., II, MOZER, J. D. & DI GIONIA, A. M. Predicting ice and snow loads for transmission lines. *In:* JR., P., B.A, ed. Celerino Grandiosa, In the proceedings of the first IWAIS, 1983. 267-273.

GRIFFIN, D., A. 2004. Blade System Design Studies Volume II: Preliminary Blade Designs and Recommended Test Matrix. *In:* EDITOR 2004, S.-. (ed.) *WindPACT.* Washington, USA.

GRIFFIN, D., A. & ASHWILL, T., D. 2003. Alternative Composite Materials for Megawatt-Scale Wind Turbine Blades: Design considerations and Recommended Testing. *J. Sol. Energy Eng.,* 125**,** 515-521.

GURSEL, K., T., ÇOBAN, T. & ÖZDAMAR, A. 2012. VIBRATION ANALYSIS OF ROTOR BLADES OF A FARM WIND-POWER PLANT. *Mathematical and Computational Applications,* 17**,** 164-175.

GUTIERREZ, E., S. 2003. *Modal Analysis of Rotating Machinery Structures.* PhD, Imperial College London.

HAALAND, S., S. . 2011. *Estimating Production Loss due to Icing on Wind Turbines.* MSc, University of Troms

HAMEEDA, Z., HONGA, Y., S., CHOA, Y., M., AHNB, S., H. & SONG, C., K. 2009. Condition monitoring and fault detection of wind turbines and related algorithms: A review. *Renewable and Sustainable Energy Reviews,* 13**,** 1-39.

HANSEN, M., H. 2003. Improved Modal Dynamics of Wind Turbines to Avoid Stall-induced Vibrations. *Wind Energy,* 6**,** 179–195.

HANSEN, M., H. , FUGLSANG, P., THOMSEN, K. & KNUDSEN, T. 2006. Two methods for estimating aeroelastic damping of operational wind turbine modes from experiments. *Wind & Solar Energy,* 9.

HANSEN, M. O. 2015. *Aerodynamics of wind turbines*, Routledge.

HARTWANGER, D. & HORVAT, A. 3D modelling of a wind turbine using CFD. NAFEMS Conference, United Kingdom, 2008.

HAU, E. 2010a. *Wind Turbines Fundamentals, Technologies, Application, Economics,* Berlin, Germany.

HAU, E. 2010b. *Wind Turbines Fundamentals,Technologies, Application, Economics,* Berlin, Germany, Springer.

HILLERMEIER, R. W. 2009. New composite hybrid reinforcements for the wind turbine industry. *JEC composites***,** 36-38.

HOGG, P. 2010. Wind Turbine Blade Materials. *In:* ASSEMBLY, S. W. P. F. (ed.). Loughborough, UK: University of Loughborough.

HOLOOPTICS 2012. Estimating Energy Production Losses, Comparison with Ice Detection. *In:* 2012, W. (ed.) *Cold climate wind energy solutions.* Skellefteå, Sweden.

HOMOLA, M., C. 2005. Impacts and Causes of Icing on Wind Turbines. *In:* PROJECT, I. I. B. (ed.).

HOMOLA, M. C., VIRK, M., NICKLASSON, P. & SUNDSBø, P. 2011. Modelling of ice induced power losses and comparison with observations. *Proceedings of the Winterwind*.

HOMOLA, M. C., VIRK, M. S., NICKLASSON, P. J. & SUNDSBø, P. A. 2012. Performance losses due to ice accretion for a 5 MW wind turbine. *Wind Energy,* 15**,** 379-389.

HOMOLA, M. C., WALLENIUSB, T., MAKKONENB, L., NICKLASSONA, P. J. & SUNDSBøA, P. A. The dependence of icing severity on chord length. *In:* EWEC, ed. European Wind Energy Conference and Exhibition March 16-19, 2009 2009 Marseille, France. .

HOUGHTON, E. L. & CARPENTER, P. W. 2003. *Aerodynamics for engineering students*, Butterworth-Heinemann.

HU, G., Y., SUN, W., L., WU, A. & XU, Y. 2012. Modal Analysis of Three Rotating Blades of Large Wind Turbine. *Applied Mechanics and Materials,* 157 - 158**,** 1-6.

IEC, I. S. 1999. Wind turbine generator system. *Part I: safety requirements.* Geneva, Switzerland.

ISO 2001a. Atmospheric Icing of Structures. *In:* INTERNATIONAL STANDARDISATION ORGANISATION, I. (ed.).

ISO, E. 2001b. Atmospheric icing of structures, INTERNATIONAL STANDARD. *ISO 12494.* Switzerland.

JASINSKI, W., J., NOE, S., C., SELIG, M., S. & BRAGG, M., B. . Wind turbine performance under icing conditions. *In:* AIAA, ed. AIAA Meeting Papers on Disc, 1997 Reno, NV, USA.

JASINSKI, W. J., NOE, S. C., SELIG, M. S. & BRAGG, M. B. 1998. Wind turbine performance under icing conditions. *Journal of Solar Energy Engineering,* 120**,** 60-65.

JOHN, F. Wind Power Development in Sub-Arctic Conditions with Severe Rime Icing. Circumpolar Climate Change Summi tand Exposition, 2001 Whitehorse, Yukon, Canada.

JONKMAN, J. 2006a. NREL 5MW Offshore Baseline. *In:* NREL/NWTC (ed.). Golden, CO, USA: National Wind Technology Center.

JONKMAN, J. 2006b. NRELOffshrBsline5MW. *In:* NREL/NWTC (ed.). Golden, CO, USA: National Wind Technology Center.

JONKMAN, J., BUTTERFIELD, S., MUSIAL, W. & SCOTT, G. 2009. Definition of a 5-MW Reference Wind Turbine for Offshore System Development. *In:* LABORATORY, N. R. E. (ed.).

KHULIEF, Y., A. 1989. Vibration Frequencies of a Rotating Tapered Beam With End Mass. *Journal of Sound and Vibration,* 134**,** 87-97.

KIM, D., H. & KIM, Y., H. 2011. Performance Prediction of a 5MW Wind Turbine Blade Considering Aeroelastic Effect. *World Academy of Science, Engineering and Technology,* 81**,** 771-775.

KIM, K.-T. & LEE, C.-W. Structural Vibration Analysis of Large-scale Wind Turbines Considering Periodically Time-Varying Parameters. 13th World Congress in Mechanism and Machine Science, 2011 Guanajuato, México.

KISHORE, R. A., COUDRON, T. & PRIYA, S. 2013. Small-scale wind energy portable turbine (SWEPT). *Journal of Wind Engineering and Industrial Aerodynamics,* 116**,** 21-31.

KOLLáR, L., E. & FARZANEH, M. 2010. Wind-tunnel investigation of icing of an inclined cylinder. *International Journal of Heat and Mass Transfer,* 53**,** 849-861.

KRAJ, A., G. & BIBEAU, E., L. 2010. Phases of icing on wind turbine blades characterized by ice accumulation. *Renewable Energy,* 35**,** 966–972.

LAAKSO, T., BARING-GOULD, I., DURSTEWITZ, M., HORBATY, R., LACROIX, A., PELTOLA, E., RONSTEN, G., TALLHAUG, L. & WALLENIUS, T. 2010. State-of-the-art of wind energy in cold climates. *In:* V.W.P. (ed.). Finland: Technical Research Centre of Finland.

LAAKSO, T. & PELTOLA, E. Review on Blade Heating Technology and Future Prospects, 2005 Saariselkä, Finland. BOREAS VII. FMI, 12.

LAAKSO, T. E. A. 2010. State-of-the-art of wind energy in cold climates. vtt.fi /reports/State Of The Art Of Cold Climate 2009. pdf. Accessed May 2010., VTT, Editor 2009.

LACROIX, A. & MANWELL, J. F. 2000. Wind Energy: Cold Weather Issues. *In:* LABORATORY, R. E. R. (ed.).

LANZAFAM, R. & MESSINA, M. 2007. Fluid Dynamics Wind Turbine Design: Critical Analysis, Optimization and Application of BEM Theory. *Renewable Energy,* 32 2291-2305.

LARSEN, G., C., HANSEN, M., H., BAUMGART, A. & CARL´EN, I. 2002. Modal Analysis of Wind Turbine Blades. *In:* RISø NATIONAL LABORATORY (ed.) *Risø.* Roskilde, Denmark.

LARSEN, T., J. & HANSON, T., D. A Method to Avoid Negative Damped Low Frequent Tower Vibrations for a Floating, Pitch Controlled Wind Turbine. *In:* DENMARK, T. T. U. O., ed. The 2th EWEA/EAWE Special Topic Conference, The Science of making Torque from Wind, 28-31 August 2007 2007a Bergen, Norway.

LARSEN, T. J. & HANSON, T. D. A method to avoid negative damped low frequent tower vibrations for a floating, pitch controlled wind turbine. Journal of Physics: Conference Series, 2007b. IOP Publishing, 012073.

LEE, J.-W., LEE, J.-S., HAN, J.-H. & SHIN, H.-K. 2012. Aeroelastic analysis of wind turbine blades based on modified strip theory. *J. Wind Eng. Ind. Aerodyn.,* 110**,** 62-69.

LEHTOMäKI, V., HETMANCZYK, S., DURSTEWITZ, M., BAIER, A., FREUDENREICH, K. & ARGYRIADIS, K. Iced Blades - Modelling of ice accretion on rotor blades in a coupled wind turbine tool. *In:* 2012, W., ed. Winterwind 2012, 7-8 Feb. 2012 2012 Skellefteå, Sweden.

LIGHT, T. & ROBINSON, J. 2003. Aerodynamic Design of a Large Horizontal-Axis Wind Turbine. *In:* SULLIVAN, P. J. P. (ed.).

LIN, S.-M., LEE, S.-Y. & LIN, Y.-S. 2008. Modeling and Bending Vibration of the Blade of a Horizontal-AxisWind Power Turbine. *CMES,* 23**,,** 175-186.

LIU, T., R. & REN, Y., S. 2011. Vibration and flutter of wind turbine blade modeled as anisotropic thin-walled closed-section beam. *Sci China Tech Sci,* 54**,** 715−722.

LLOYD, G. 1999. Regulations for the certification of wind energy conversion system. Germany.

LLOYD, G. 2004. Guideline for the Certification of Wind Turbines, edition 2003, with supplement. Hamburg, Germany.

LOTH, E., STEELE, A., ICHTER, B., SELIG, M. & MORIARTY, P. 2012. Segmented Ultralight Pre-Aligned Rotor for Extreme-Scale Wind Turbines. *In:* AIAA (ed.) *50th AIAA Aerospace Sciences Meeting including the New Horizons Forum and Aerospace Exposition.* Nashville, Tennessee.

MAALAWI, K. & BADR, M. 2010. Frequency optimization of a wind turbine blade in pitching motion. Proceedings of the Institution of Mechanical Engineers, Part A. *Journal of Power and Energy,* 224 (A4)**,** 545-554.

MADSEN, P. H., FRANDSEN, S. T., HOLLEY, W. E. & HANSEN, J. C. 1984. Dynamics and fatigue damage of wind turbine rotors during steady operation. Danmarks Tekniske Universitet, Risø Nationallaboratoriet for Bæredygtig Energi.

MAISSAN, T. M. 2001. The Effects of the Black Blades on Surface Temperatures for Wind Turbines. *In:* J., W. A. T. (ed.) *Applied Mechanics and Materials.* Canada: Université du Québec à Rimouski.

MAKKONEN, L. 1988. Estimation of Wet Snow Accretion on Structures. *Cold Regions Science and Technology,* 17**,** 83-88.

MAKKONEN, L. 1994. Ice and Construction, Rilem report 13. *In:* CHAPMAN & HALL; LONDON, E. (ed.) First edition ed.

MAKKONEN, L. 2000. Models for the growth of rime, glaze, icicles and wet snow on structures. *Philosophical Transactions of the Royal Society,* 358**,** 2913-2939.

MANUEL, L., VEERS, P., S. & WINTERSTEI, S., R. 2001. Parametric Models For Estimating Wind Turbine Fatigue Loads For Design. *In:* MEETING, A. A. S. (ed.) *Proceedings of the 20th ASME Wind Energy Symposium.* Journal of Solar Energy Engineering.

MANWELL, J., F., MCGOWAN, J., G. & ROGERS, A., L. 2009. *Wind Energy Explained, Theory, Design and Application,* Great Britain by CPI Antony Rowe, Chippenham, Wiltshire., John Wiley & Sons Ltd.

MARJANIEMI, M., LAAKSO, T., MAKKONEN, L. & WRIGHT, J. 2001. Results of Pori wind farm measurements. *VTT Energy, Espoo*.

MATHEW, S. & PHILIP, G. S. 2011. *Advances in wind energy and conversion technology*, Springer.

MCCORMICK, B. W., MCCORMICK, B. W. & MCCORMICK, B. W. 1995. *Aerodynamics, aeronautics, and flight mechanics*, Wiley New York.

MEIROVITCH, L. 2001. *Fundamentals of Vibrations,* New York, USA.

MISHNAEVSKY JR, L. & FAVORSKY, O. 2011. Composite materials in wind energy technology. *Thermal to Mechanical Energy Conversion: Engines and Requirements, EOLSS Publishers: Oxford, UK*.

MONTEIRO, J., PáSCOA, J. & BROJO, F. Simulation of the Aerodynamic Behaviour of a Micro Wind Turbine. International Conference on Renewable Energies and Power Quality, 2009.

MORGAN, C., BOSSANYI, E. & SEIFERT, H. 1998. Assessment of Safety Risks Arising from Wind Turbine Icing. *BOREAS IV.* Hetta, Finland.

MORTENSEN, K. 2008. *CFD Simulations of an Airfoil With Leading Edge Ice Accretion.* MSc, Technical University of Denmark, DTU.

MURTAGH, P., BASU, B. & BRODERICK, B. 2004. Mode acceleration approach for rotating wind turbine blades. *Proceedings of the Institution of Mechanical Engineers, Part K: Journal of Multi-body Dynamics,* 218**,** 159-167.

MURTAGH, P., J., GHOSH, A., BASU, B. & BRODERICK, B., M. 2007. Passive Control of Wind Turbine Vibrations Including Blade/Tower Interaction and Rotationally Sampled Turbulence. *Wind Energy,* 11**,** 305-317.

MYERS, T., G. & CHARPIN, J., P., F. 2004. A mathematical model for atmospheric ice accretion and water flow on a cold surface. *International Journal of Heat and Mass Transfer,* 47**,** 5483-5500.

OSGOOD, R., M. 1998. Modal Testing of Advanced Wind Turbine Systems. *In:* NREL, N. R. E. L. (ed.). Golden, Colorado, USA: NREL.

OZBEK, M., F., M., RIXEN, D., J. & TOOREN, M., J., L., VAN 2010. Identification of the Dynamics of Large Wind Turbines by Using Photogrammetry. *In:* INC, S. F. E. M. (ed.) *Conference Proceedings of the Society for Experimental Mechanics.* Jacksonville, Florida, USA.

PARENT, O. & ILINCA, A. 2011. Anti-icing and de-icing techniques for wind turbines: Critical review. *Cold Regions Science and Technology,* 65**,** 88-96.

PARK, J., H., PARK, H., Y., JEONG, S., Y., LEE, S., SHIN, Y., H. & PARK, J., P. 2010 Linear vibration analysis of rotating wind-turbine blade. *Current Applied Physics,* 10**,** S332–S334.

PERIC, M. 2004. Flow simulation using control volumes of arbitrary polyhedral shape. *In:* 62, E. B. N. (ed.).

PERKINS, F. W. & CROMACK, D. E. 1978. Wind Turbine Blade Stress Analysis And Natural Frequencies.

PEROVIC, S., OSBORNE, M., LLOYD, G. & BRIDGES, P. Intelligent Blade Ice Detection and Measurement. European Wind Energy Conference & Exhibition, 2010 Warsaw, Poland.

PERVEZ, N. & MOKHTAR, W. CFD Study of a Darreous Vertical Axis Wind Turbine Proceedings of the 2012 ASEE North Central Section Conference, 2012.

PIOVAN, M., T. & SAMPAIO, R. 2009. A Study on the Dynamics of Rotating Beams with Functionally Graded Properties. *Journal of Sound and Vibration,* 327**,** 134-143.

POLLINO, M., C. & HUCKELBRIDGE, A., A. JR 2007. In-situ Measurements of Fatigue Demands on a Wind Turbine Support Structure *In:* PROGRAM, T. O. T. F. (ed.). Cleveland, OH, USA: Western Reserve University.

RAO, S. S. 2004. Mechanical vibrations. Pearson Prentice Hall, Inc. NJ.

RATHORE, A. S. & AHMED, S. 2011. Design and Analysis of Horizontal Axis Wind Turbine Rotor. *International Journal of Engineering Science & Technology,* 3.

RINDESKäR, E. 2010. Modelling of icing for wind farms in cold climate. *In:* SCIENCES, D. O. E. (ed.) *Uppsala University.* Uppsala, Sweden.

RISø, N. L. 2002. Guidelines for Design of Wind Turbines. *In:* LABORATORY, R. N. (ed.). Copenhagen, Denmark: Wind Energy Department.

RONSTEN, G. 2008. Mapping of Icing for Wind Turbine Applications, A Feasibility Study. *In:* PRODUCTION, E. A. P. (ed.). Stockholm, Sweden.

RONSTEN, G., WALLENIUS, T., HULKKONEN, M., BARING-GOULD, I., CATTIN, R., DURSTEWITZ, M., KRENN, A., LAAKSO, T., LACROIX, A., TALLHAUG, L., BYRKJEDAL, Ø. & PELTOLA, E. 2012. State-of-the-Art of Wind Energy in Cold Climates *In:* WIND, I. (ed.). Stockholm, Sweden.

ROSENOW, S., E. & ANDERSEN, P. Operational Modal Analysis of a Wind Turbine Mainframe using Crystal Clear SSI. Proceedings of the IMAC-XXVIII, 2010 Jacksonville, Florida, USA.

SAILOR, D., J., SMITH, M. & HART, M. 2008. Climate Change Implications for Wind Power Resources in the Northwest United States. *Renewable Energy,* 33**,** 2393–2406.

SATARI, M., A. & HUSSAIN, S. Vibration Based Wind Turbine Tower Foundation Design Utilizing Soil-Foundation-Structure Interaction. The 14th World Conference on Earthquake Engineering, 2008 Beijing, China.

SCHUELLER, O., J., A. , BRITTAIN, S., T., MARZOLIN, C. & WHITESIDES, G., M. 1997a. Fabrication and Characterization of Glassy Carbon. *Chem. Mater.,* 9**,** 1399-1406.

SCHUELLER, O., J., A. , BRITTAIN, S., T., MARZOLIN, C. & WHITESIDES, G. M. 1997b. Fabrication and Characterization of Glassy Carbon. *Chem. Mater.,* 9**,** 1399-1406.

SEIFERT, H. Technical Requirements for Rotor Blades Operating in Cold Climate. BOREAS VI. FMI, 2003 Pyhätunturi, Finland. 13.

SEIFERT, H. & RICHERT, F. Aerodynamics of Iced Airfoils and Their influence on Loads and Power Production. The European Wind Energy Conference, 1997a Dublin Castle, Ireland.

SEIFERT, H. & RICHERT, F. 1997b. Aerodynamics of Iced Airfoils and Their influence on Loads and Power Production. *The European Wind Energy Conference.* Dublin Castle, Ireland.

SEIFERT, H. & TAMMELIN, B. 1996. Icing of wind turbines-Final Report. *In:* ENERGIES-INSTITUTE, D. W. (ed.). Wilhelmshaven, Finland: Finnish Meteorological Institute.

SEIFERT, H., WESTERHELLWEG, A. & KRöNING, J. Risk Analysis Of Ice Throw From Wind Turbines. BOREAS 6, 2003 Pyhä, Finland.

SHIN, J. & BERKOWITZ, B. 1994. Prediction of ice shapes and their effect on airfoil drag. *Journal of aircraft,* 31**,** 263-270.

SICOT, C., DEVINANT, P., LOYER, S. & HUREAU, J. 2008. Rotational and Turbulence Effects on A Wind Turbine Blade: Investigation of The Stall Mechanisms. *Journal of Wind Engineering and Industrial Aerodynamics,* 96**,** 1320- 1331.

SONG, Y.-H., LUI, T.-S., CHEN, L.-H. & SONG, J.-M. 2003. Effect of Nodular Graphite on the Deterioration of Vibration Fracture Resistance of Ferritic Cast Iron under an Aqueous Environment. *Materials Transactions,* 44**,** 1461 to 1468.

STAINO, A., BASU, B. & NIELSEN, S., R., K. 2012. Actuator control of edgewise vibrations in wind turbine blades. *Journal of Sound and Vibration,* 331**,** 1233-1256.

STANDARD DNV, D. N. V. 2010. Design and Manufacture of Wind Turbine Blades, Offshore and Onshore Wind Turbines. Bærum, Norway.

SUNDINA, E. & MAKKONEN, L. 1998. Ice Loads on a Lattice Tower Estimated by Weather Station Data. *Journal of Applied Meteorology,* 37**,** 523-529.

SWEENEY, D. 2015. http://www.cadfemukandireland.com/category/simulation-driven-development/.

TAMMELIN, B. 2005. *Wind Turbines in Icing Environment: Improvement of Tools for Siting, Certification and Operation*, NEW ICETOOLS.

TAMMELIN, B., CAVALIERE, M., HOLTTINEN, H., MORGAN, C., SEIFERT, H. & SäNTTI, K. 1998. Wind Energy Production In Cold Climate. *In:* COMMISSION, T. E. (ed.) *WECO.* Copenhagen, Denmark.

TAMMELIN, B., CAVALIERE, M., HOLTTINEN, H., MORGAN, C., SEIFERT, H. & SäNTTI, K. 2000. Energy Production in Cold Climate, Meteorological Publication No 41. *In:* INSTITUTE, F. M. (ed.). Helsinki. Finland.

TAMMELIN, B. & SEIFERT, H. 2001. LARGE WIND TURBINES GO INTO COLD CLIMATE REGIONS. *EWEC.* Copenhagen, Denmark.

TARFAOUI, M., KHADIMALLAH, H., IMAD, A. & PRADILLON, J., Y. 2011. Design and Finite Element Modal Analysis of 48m Composite Wind Turbine Blade. *Applied Mechanics and Materials,* 146**,** 170-184.

TARTIBU, L. K., KILFOIL, M. & VAN DER MERWE, A. J. 2012. Vibration Analysis of a Variable Length Blade Wind Turbine *International Journal of Advances in Engineering & Technology,* 4**,** 630-639.

TONGGUANG, W., LONG, W., WEI, Z., BOFENG, X. & LI, C. 2012 Large-Scale Wind Turbine Blade Design and Aerodynamic Analysis. *Chinese Science Bulletin,* 57**,** 466-472.

TURKIA, V., HUTTUNEN, S. & WALLENIUS, T. 2010. Method for Estimating Wind Turbine Production Losses Due To Icing. *In:* FINLAND, T. R. C. O. (ed.). Technical Research Centre of Finland.

VARGAS, M. 2010. Wind Energy Icing. *In:* CENTER, G. R. (ed.).

VERSTEEG, H. & MALALASEKERA, W. 2007. *An Introduction to Computational Fluid Dynamics: The Finite Volume Method*

VIRK, M., S., HOMOLA, M., C. & NICKLASSON, P., J. 2012. Atmospheric icing on large wind turbine blades. *International Journal of Energy and Environment (IJEE),* 3**,** 1-8.

VIRK, M. S. & HOLDO, A. E. 2008. Numerical study of wind loads on a low-rise pitched roof building with spirelet. *International Journal of Computational Fluid Dynamics,* 22**,** 687-694.

VOITKOVSKII, K., F. 1960. THE MECHANICAL PROPERTIES OF ICE. *In:* SOCIETY, T. A. M.-. (ed.). Massachusetts, USA: Air Force Cambridge Research Laboratories.

WADHAM-GAGNON, M., BOLDUC, D., BOUCHER, B., CAMION, A., PETERSEN, J. & FRIEDRICH, H. Ice Profile Classification Based on ISO 12494. WinterWind 2013, 12-13 Feb. 2013 2013 Östersund, Sweden.

WALSH, M. 2010. *Accretion and Removal of Wind Turbine Icing in Polar Conditions.* M. Sc., AALTO UNIVERSITY.

WANG, J., QIN, D. & LIM, T., C. 2010. Dynamic Analysis of Horizontal Axis Wind Turbine by Thin-Walled Beam Theory. *Journal of Sound and Vibration,* 329**,** 3565-3586.

WANG, X., BIBEAU, E., L. & NATERER, G., F. Experimental Investigation of Energy Losses due to Icing of a Wind Turbine. International Conference on Power Engineering, 2007 Hangzhou, China.

WILBURN, D. R. 2011. Wind Energy in the United States and Materials Required for the Land-Based Wind Turbine Industry From 2010 Through 2030. *In:* USGS (ed.). Reston, Virginia, USA: U.S. Department of the Interior.

XING, T. & STERN, F. 2007. Introduction to Computational Fluid Dynamics (CFD). The University of Iowa.

ZHANG, J., ZHANG, K., ZHOU, A., ZHOU, T., HU, D. & REN, J. 2014. Analysis of Nonlinear Dynamic Response of Wind Turbine Blade Under Fluid–Structure Interaction and Turbulence Effect. *Journal of Engineering for Gas Turbines and Power,* 136**,** 102604.

ZHANG, Z. 2009. *Wind turbine vibration study: a data driven methodology.* M. Sc., University of Iowa.

ZHIQUAN, Y., HAOMIN, M., NENGSHENG, B., YAN, C. & KANG, D. 2001. Structure Dynamic Analysis of a Horizontal Axis Wind Turbine System Using a Modal Analysis Method *Wind engineering,* 25**,** 237-248.

Publication List

[1] Abdel Salam Y. Alsabagh, et al. "A Review of the Effects of Ice Accretion on the Structural Behaviour of Wind Turbines." *Wind Engineering* 37.1 (2013): 59-70.

[2] Abdel Salam Y. Alsabagh, Yigeng Xu, Muhammad S. Virk, and Omar Badran, “Atmospheric Ice Loading and Its Impact on Natural Frequencies”, ‘Journal of Wind Engineering” *Wind Engineering* 39.1 (2015):

Conferences

[1] Abdel Salam Y. Alsabagh, Yigeng Xu, Muhammad S. Virk, and Omar Badran, “Serious Consequences Due To Excessive Ice Accumulation on a Typical Wind Turbine”, (2014) Winterwind 2014, (12-14 Feb. 2014), Färentuna, Sweden.

[2] Abdel Salam Y. Alsabagh, W. T. a. M. S. V. (2011). Effect of Atmospheric Ice Accretion on the Dynamic Behaviour of Wind Turbine. The Sixth International Conference in Multiphysics (MULTIPHYSICS 2011) Barcelona, Spain on 15-16 December 2011.

APPENDICES

Appendix A

Table A1: Details for ice estimated mass and load with respect to R8

Icing Zone	Longest Distance Across Sections W (mm)	Length of Selected Zone (m)	Estimated Accreted Ice Mass (kg/m)	Estimated Accreted Ice Load (kg/Zone)
1	380	2.7	36.8	99.4
2	420	2.9	41.0	118.9
3	680	4	69.2	276.8
4	1480	16	156.1	2497.6
5	1870	21	198.4	4166.4

Table A2: Details for ice estimated mass and load with respect to R9

Icing Zone	Longest Distance Across Sections W (mm)	Length of Selected Zone (m)	Estimated Accreted Ice Mass (kg/m)	Estimated Accreted Ice Load (kg/Zone)
1	380	2.7	63.8	172.3
2	420	2.9	70.6	204.7
3	680	4	116.4	465.6
4	1480	16	253.6	4057.6
5	1870	21	320.6	6732.6

Table A3: Reduction in natural frequencies due to assembly and ice loading effect

Mode No.	Reduction due to assembly	Reduction for moderate scenario		Reduction for R8 scenario		Reduction for R9 scenario	
		Non-Rotating	Rotating	Non-Rotating	Rotating	Non-Rotating	Rotating
1	7%	5%	0%	17%	12%	24%	20%
2	9%	4%	3%	19%	15%	24%	22%
3	8%	4%	0%	19%	12%	25%	19%